Versatile Circular Test Structure for Ohmic Contact Characterisation

A thesis submitted in fulfilment of the requirements for the degree of Doctor of Philosophy

Yue Pan

B.E., M. Eng.

School of Electrical and Computer Engineering

College of Science Engineering and Health

RMIT University

March 2015

"To my parents, my wife and my little boy"

Declaration

I certify that except where due acknowledgement has been made, the work is that of the author alone; the work has not been submitted previously, in whole or in part, to qualify for any other academic award; the content of the thesis is the result of work which has been carried out since the official commencement date of the approved research program; and, any editorial work, paid or unpaid, carried out by a third party is acknowledged.

Yue Pan
March 2015

Acknowledgements

I would like to express my deepest gratitude to my supervisor, Associate Professor Anthony S. Holland, for his excellent guidance, caring, patience, and providing me with an excellent atmosphere for doing research and careful proof-reading of manuscripts and this thesis. He has taught me a great deal of semiconductor research in both general and specific topics.

I would like to thank Adjunct Professor Geoffrey K. Reeves and Dr. Patrick W. Leech, for their encouragement, scientific and insightful comments throughout my Ph.D. program.

I would also like to thank the microelectronic and materials technology centre (MMTC) technical officers: Mr. Yuxun Cao and Ms. Chiping Wu for training me on the initial procedures in the clean room and helping me with metal evaporation systems and other equipment at the MMTC. I would like to acknowledge Dr. Philip Tanner for offering me SiC samples for my experimental work.

Many thanks to Mr. Aaron M. Collins, Mr. Ghazwan Haddad and Mr. Jorge Rigoberto Jimenez Uribe, who as my colleges and best friends, were always willing to help and give their best suggestions. My research would not have been possible without their helps.

I am indebted to my amazing parents X. Y. Pan and F. H. Zhan for supporting me financially and emotionally.

Abstract

Metal to semiconductor contacts can be divided into two groups: rectifying contacts and non-rectifying contacts [Braun, 1874]. For a non-rectifying contact, which is also known as an ohmic contact, there is an electrical junction between the metal and semiconductor that has a linear current–voltage (I-V) characteristic (as with Ohm's law). A low resistance ohmic contact allows the carriers to flow easily in both directions between the metal and semiconductor. Ohmic contacts are essential for most semiconductor devices e.g. p-n diodes, Schottky diodes, metal–oxide–semiconductor field-effect transistors (MOSFETs), metal–semiconductor field effect transistors (MESFETs) and so on. Lower and lower ohmic contact resistance is desired as the dimensions of devices decrease and nanotechnology demands better means of creating electrical access to devices.

Continued improvement in the performance of ohmic contacts requires better characterisation of such contacts. In order to study the properties of ohmic contacts, the parameter specific contact resistivity (SCR), ρ_c, was introduced by [Chang et al., 1971]. Accurate test structures and evaluation techniques needed to be developed to obtain the values of ρ_c and the transmission line model (TLM) [Shockley, 1964], the circular transmission line model (CTLM) [Reeves, 1980] and the cross-bridge Kelvin resistor test structure (CBKR) [Shih and Blum, 1972] are the most commonly used techniques. Although they have their advantages in either analytical expressions or fabrications, their disadvantages exist as well.

In this work, new ohmic contact test structure, the two-contact circular test structure [Pan et al., 2013], has been developed for determining ρ_c. There is no correction factor and a mesa etch is unnecessary, compared to the TLM and

the conventional CTLM. Furthermore, the new structure removes the middle ring contact, which can be difficult to probe and to maintain as an equipotential, compared to the conventional three-electrode CTLM test structure. The evaluation techniques are also presented and demonstrated by using finite element modeling (FEM). Experimental results are reported for different metal to semiconductor ohmic contacts to verify the two-contact circular test structure. As examples of contacts to two-dimensional (2-D) semiconductor layers (relatively to vertical voltage drop in the semiconductors), the values of ρ_c of Ni to heavily doped n-type epitaxial 3C-SiC and Ti to lightly doped n-type epitaxial 3C-SiC ohmic contacts were determined to be $(0.8 - 5.7) \times 10^{-6}\ \Omega \cdot cm^2$ and $(3.0 - 7.5) \times 10^{-4}\ \Omega \cdot cm^2$ respectively using the proposed test structure and its corresponding evaluation technique. For contacts to bulk semiconductors (3-D circumstances compared to 2-D circumstances, where semiconductor vertical voltage drop is significant), the values of ρ_c of Ni to p-type bulk Ge and Ti to n-type 4H-SiC substrate ohmic contacts were determined to be $(2.3 - 27) \times 10^{-6}\ \Omega \cdot cm^2$ and $(1.8 - 2.5) \times 10^{-3}\ \Omega \cdot cm^2$ respectively. Furthermore, an investigation of the effect of low energy implantation on the properties of Au/Ni/Ti contacts to heavily doped n-type epitaxial 3C-SiC has been undertaken using the proposed test structure and its corresponding evaluation technique applied for the contacts to these 2-D semiconductor layers.

Contents

List of Figures

List of Tables

Nomenclature

Roman Symbols

A Contact area (in square micrometers).

d The distance between each two contact in the transmission line model (in micrometers); The width of the contact window in the cross-bridge Kelvin resistor test structure (in micrometers); The gap between the two electrodes in combined TLM-CLTM test structure (in micrometers).

$d^{'}$ The width of the diffusion region in the cross-bridge Kelvin resistor test structure (in micrometers).

e Mathematical constant, $e \approx 2.71828$.

F Factor used to extract ρ_c in the two-contact circular test structure (no unit).

$F^{'}$ Factor used to extract ρ_c in the two-contact circular test structure (no unit).

$\hbar$ The modified Planck constant.

I Current through the contacts (in milliamperes).

J Current density (in milliamperes per square micrometers).

K Ratio of R_{T1} - R_{T3} and R_{T1} - R_{T2} in the two-contact circular test structure (no unit).

k The Boltzmann constant.

L Contact length in the transmission line model (in micrometers).

m^* Effective mass of tunneling electron (in kilogrammes).

N Doping concentration (in cm^{-3}).

q Electrical charge (in coulomb).

T Temperature (in Kelvin degrees).

t Thickness (in micrometers).

t' Threshold thickness (in micrometers).

V Measured voltage drop between two electrodes (in millivolts).

W Contact width in the transmission line model (in micrometers).

W' The width of the diffusion area in the transmission line model (in micrometers).

Z Characteristic line resistance (in ohms).

Greek Symbols

α Attenuation constant, the inverse of the transfer length (L_T) in linear transmission line model (in per micrometer), $\alpha^2 = R_{SH}/\rho_c$.

Δ Factor used to extract ρ_c when using the circular transmission line model (no unit).

δ Distance between the contact edge and the edge of the diffusion region in the cross-bridge Kelvin resistor test structure (in micrometers).

η The ratio of the contact interfacial resistance R_i to the vertical semiconductor resistance R_S, $\eta = R_i/R_S$. It can be also written as $\eta = \rho_c/(\rho_b \cdot t)$ (no unit).

ρ Electrical resistivity (in ohms centimeter).

ϕ Factor used to extract ρ_c when using the circular transmission line model (no unit).

σ Electrical conductivity, the inverse of the electrical resistivity (ρ) (in per ohms centimeter), $\sigma = 1/\rho$.

θ An experimental determined factor for extracting ρ_c in the combined TLM-CTLM test structure (in per ohms).

φ An experimental determined factor for extracting ρ_c in the combined TLM-CTLM test structure (no unit).

Other Symbols

E_{00} Reference energy related to the probability of tunneling (in keV).

ε_s Semiconductor permittivity (no unit).

I_0 Zeroth order modified Bessel function of the first kind.

I_1 First order modified Bessel function of the first kind.

J_s Saturation current density (in milliamperes per square micrometers).

K_0 Zeroth order modified Bessel function of the second kind.

K_1 First order modified Bessel function of the second kind.

L_T Transfer length (in micrometers).

ϕ_B Potential barrier (in eV).

ρ_b Bulk semiconductor resistivity (in ohms centimeter).

ρ_c Specific contact resistivity (in ohms square centimeter).

r_0 Radius of the central dot electrode in both the two-contact circular test structure and the circular transmission line model (in micrometers).

R_1 Measured resistance between the left two contacts in Fig. 2.2 (in ohms); Measured resistance between the inner two contacts in the circular transmission line model (in ohms).

r_1 Inner radius of the middle ring contact in the circular transmission line model (in micrometers); Inner radius of the outer contact in the two-contact circular test structure (in micrometers).

$r_1^{'}$ Outer radius of the middle ring contact in the circular transmission line model (in micrometers); Outer radius of the outer contact in the two-contact circular test structure (in micrometers).

R_2 Measured resistance between the right two contacts in Fig. 2.2 (in ohms); Measured resistance between the outer two contacts in the circular transmission line model (in ohms).

r_2 The inner radius of the outer ring contact in the circular transmission line model (in micrometers).

$r_2^{'}$ The outer radius of the outer ring contact in the circular transmission line model (in micrometers).

R_A The bulk semiconductor resistance between the inner two contacts in the circular transmission line model (in ohms); The total resistance due to the isolated circular transmission line model pattern in the combined TLM-CTLM test structure (in ohms).

R_B The bulk semiconductor resistance between the outer two contacts in the circular transmission line model (in ohms); The total resistance due to the isolated TLM pattern in the combined TLM-CTLM test structure (in ohms).

R_C Contact resistance (in ohms).

R_{C0} Central dot contact resistance in both the two-contact circular test structure and the circular transmission line model (in ohms).

R'_{C0} Reduced central dot contact resistance in the two-contact circular test structure by considering the first term in the asymptotic forms of the Bessel functions (in ohms).

R''_{C0} Reduced central dot contact resistance in the the two-contact circular test structure by considering the first two terms in the asymptotic forms of the Bessel functions (in ohms).

R'''_{C0} Reduced central dot contact resistance in the two-contact circular test structure by considering the first three terms in the asymptotic forms of the Bessel functions (in ohms).

R_{C1} Middle ring contact resistance when current is forced between the middle ring contact and the outer ring contact in the circular transmission line model (in ohms); Outer electrode contact resistance in the two-contact circular test structure (in ohms).

R'_{C1} Middle ring contact resistance when current is forced between the central dot contact and the middle ring contact in the circular transmission line model (in ohms); Reduced outer electrode contact resistance in the two-contact circular test structure by considering the first term in the asymptotic forms of the Bessel functions (in ohms).

R''_{C1} Reduced outer electrode contact resistance in the two-contact circular test structure by considering the first two terms in the asymptotic forms of the Bessel functions (in ohms).

R_{C2} Outer ring contact resistance in the circular transmission line model in (in ohms).

R_D Semiconductor resistance in contact region of the cross-bridge Kelvin resistor test structure (in ohms).

R_{DT} Semiconductor tap resistance in the cross-bridge Kelvin resistor test structure (in ohms).

R_E Contact end resistance (in ohms).

R_I Interfacial resistance in contact region of the cross-bridge Kelvin resistor test structure (in ohms).

R_i Contact interfacial resistance (in ohm).

R_M Metal resistance in contact region of the cross-bridge Kelvin resistor test structure (in ohms).

R_{MT} Metal tap resistance in the cross-bridge Kelvin resistor test structure (in ohms).

R_P The resistance due to semiconductor layer, which surrounding the central dot electrode in the two-contact circular test structure (in ohms).

R_S Vertical semiconductor resistance (in ohms).

R_{SD} Semiconductor resistance in contact region of the cross-bridge Kelvin resistor test structure (in ohms per square).

R_{SH} Sheet resistance (in ohms per square).

R_{SK} Sheet resistance beneath the contact (in ohms per square).

R_{SM} Metal sheet resistance in contact region of the cross-bridge Kelvin resistor test structure (in ohms per square).

R_T Measured total resistance between two electrodes (in ohms).

R_{TC} The total contact resistances in the combined TLM-CTLM test structure (in ohm).

V_{b0} Built-in potential (in millivolts).

Acronyms

$CBKR$ Cross-Bridge Kelvin Resistor

$CTLM$ Circular Transmission Line Model

EDA Electronic Design Automation

FE Field Emission

FEM Finite Element Modeling

$HMDS$ Hexamethyldisilazane

IPA Isopropal Alcohol

$LPCVD$ Low Pressure Chemical Vapor Deposition

$MEMS$ Micro-Electro-Mechanical Systems

$MESFET$ Metal-Semiconductor Field-Effect Transistor

$MOSFET$ Metal-Oxide-Semiconductor Field-Effect Transistor

TE Thermionic Emission

TFE Thermionic Field Emission

TLM Transmission Line Model

$TRIM$ Transport and Range of Ions in Matter

Chapter 1

Introduction

1.1 Ohmic Contact

The earliest investigation of metal to semiconductor systems is generally regarded as having started by [Braun, 1874]. [Wilson, 1931] formulated the transport theory of semiconductors based on the band theory of solid. This theory was then applied to metal to semiconductor contacts. They have been studied extensively because of their importance in solid-state physics [Rhoderick, 1978], [Rideout, 1978]. Specifically, metal to semiconductor contacts have been used as the source and drain contacts in metal–oxide–semiconductor field-effect transistors (MOSFETs), the gate electrodes of metal–semiconductor field effect transistors (MESFETs), the anode and cathode contacts in p-n diodes and so on.

Metal to semiconductor contacts can be divided into rectifying contacts and non-rectifying contacts depending on their conduction mechanisms [Sze, 1981]. For the metal to semiconductor contacts with low doping concentrations, thermionic emission (TE) current dominates the current transport and rectifying contacts are formed (well known as Schottky contacts). The most common application of such rectifying contacts is the Schottky diode. For contacts with heavy doping concentrations, the current transport is dominated by field emission (FE). These metal to semiconductor contacts are known as ohmic contacts.

A comparison of rectifying and ohmic contacts based on both conduction mechanisms and current-voltage (I-V) characteristics is given in Fig. 1.1 [Yu, 1970].

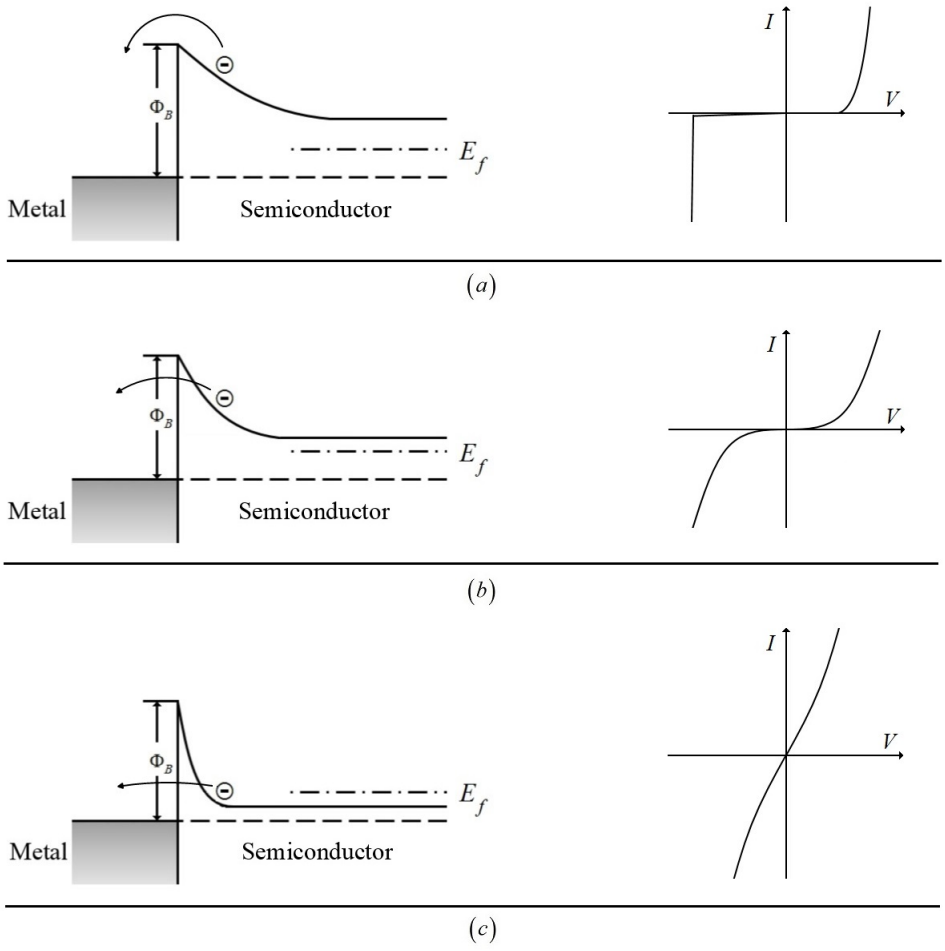

Figure 1.1: Band diagrams of metal to n-type semiconductor contacts under forward bias voltage and their I-V characteristics: (a) semiconductor lightly doped (TE), (b) semiconductor heavily doped (TFE), (c) semiconductor very heavily doped (FE).

It can be seen from Fig. 1.1 (a) that the semiconductor is lightly doped and TE occurs in the case of a depletion region so wide that the only way for electrons to cross the junction is to jump the potential barrier ϕ_B by emission over its maximum. In TE, the I-V curve shows a diode behavior. Fig. 1.1 (b) shows the energy band diagram and I-V curve for a heavily doped semiconductor. In this case, both

TE and FE occur and the mechanism of current flow is due to electrons with some thermal energy tunneling through the midsection of the potential barrier where it becomes suitably narrow. This process is called thermionic-field-emission (TFE). In Fig. 1.1 (c), the semiconductor is very heavily doped, FE occurs which effectively is carriers tunneling through the potential barrier. It takes place when the depletion region is sufficiently narrow. A linear or a near-linear I-V curve can be observed as in Fig. 1.1 (c).

In many cases, an ohmic metal to semiconductor contact with a linear I-V characteristic in both biasing directions is desired. For the contacts in some typical p and n regions in integrated circuits, it is very important that such contacts are ohmic with minimal contact resistance and no tendency to rectify signals.

An ideal ohmic contact is defined as a metal to semiconductor contact which has a negligible contact resistance relative to the resistance of the semiconductor [Sze, 1981]. A satisfactory ohmic contact will hardly affect the device performance but enables current to enter/exit the device with little voltage drop compared to the drop across the active regions of the device. A practical method to form ohmic contacts is by doping the semiconductor contact region heavily. Therefore, although a barrier exits at the interface between metal and semiconductor, the depletion width is narrow enough to allow the carriers to penetrate the barrier easily. This mechanism is also called tunneling [Streetman and Banerjee, 2000] as discussed in relation to Fig. 1.1 c.

Fig. 1.2 shows the examples of the ohmic contact applications in (a) p-n diodes and (b) MOSFETs. It can been seen that the anode and cathode contacts in p-n diodes and the source and drain contacts in MOSFETs are all ohmic contacts.

Fig. 1.3 shows the importance of an ohmic contact with a minimal contact resistance using a typical p-n diode as an example. Fig. 1.3 (a) illuminates the schematic of the cross-section of a p-n diode. It can be seen that ohmic contacts exist in both anode and cathode. Fig. 1.3 (b) shows the resistance representation of the model in (a). It can be found that the I-V curve of this diode shown in (d)

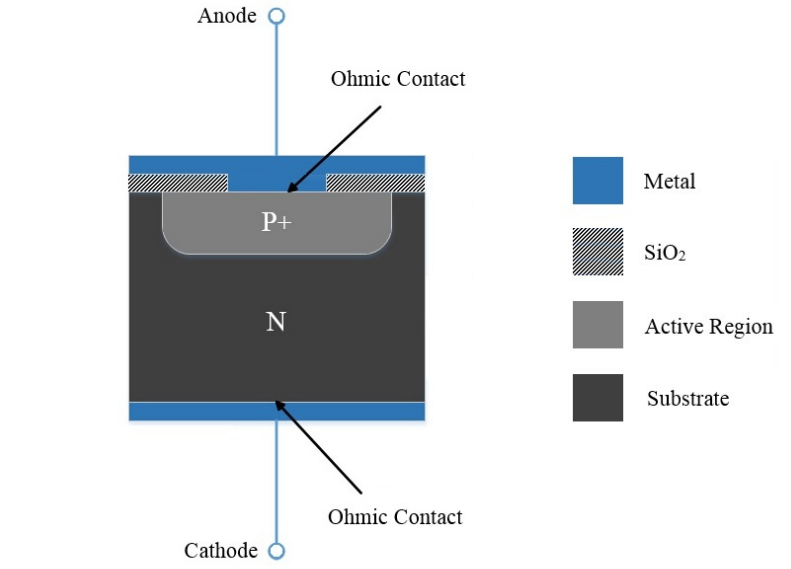

(a)

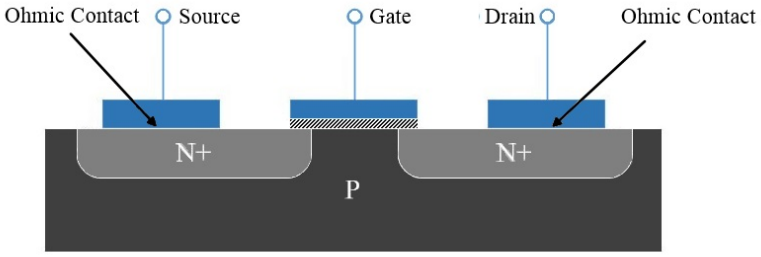

(b)

Figure 1.2: Schematics of the cross-sections of (*a*) a p-n diode and (*b*) a MOSFET. Ohmic contacts exit in the anode and cathode in the p-n diode and source and drain in the MOSFET.

is determined by both the p-n junction (R_B) and the anode and cathode contact resistances (R_{C1} and R_{C2}). However, for an ideal p-n diode, these metal contacts should have very low resistances so that the I-V curve is only determined by the p-n junction. It can let the current flowing through the diode leads to the smallest parasitic voltage drop so that the diode performance can be improved.

1.2 Specific Contact Resistivity

Specific contact resistivity (SCR), ρ_c $[\Omega \cdot cm^2]$, is an extremely important parameter for quantifying a metal to semiconductor ohmic contact. It is defined as the reciprocal of the derivative of current density with respect to voltage at $V = 0$ [Chang et al., 1971]. A good ohmic contact requires a negligible value of ρ_c to ensure the linear I-V characteristic (between such two contacts) is mainly due to resistance of the semiconductor

$$\rho_c = \left(\frac{\partial J}{\partial V} \right)^{-1}_{V=0} \tag{1.1}$$

Note that equation 1.1 is the definition of the specific contact resistivity which is a theoretical quantity referring to the metal-semiconductor interface only. In practical, a more meaningful definition of the specific contact resistivity for a real metal-semiconductor ohmic contact is an electrical parameter which is determined from measured contact resistance between metal and semiconductor. It is a very useful term for ohmic contacts because it is independent of contact area and is a convenient parameter when comparing contacts of various sizes [Schroder, 2006].

[Chang et al., 1971] derived the equations for ρ_c in both TE and FE regions. For the samples of low doping concentrations, the TE current dominates current transport

$$\rho_c = \frac{kT}{qJ_s} \tag{1.2}$$

For the samples of high doping concentrations, the tunneling process dominates

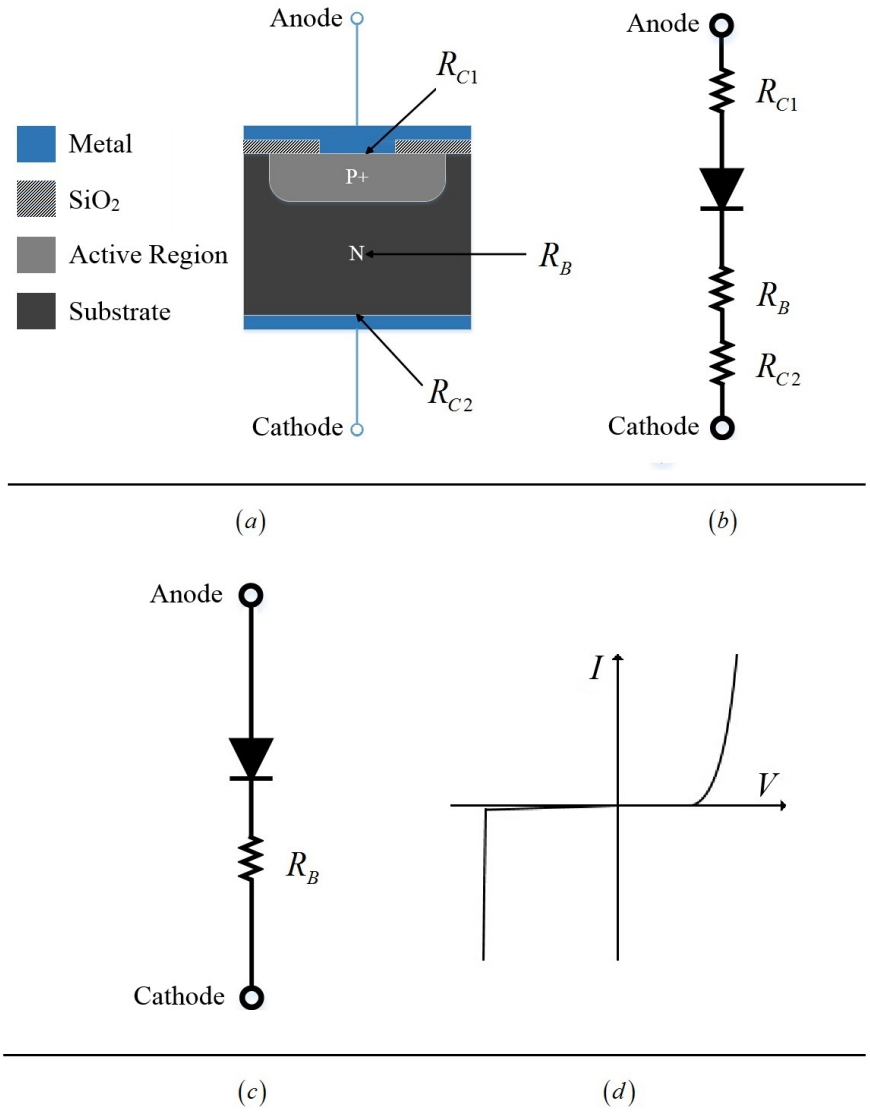

Figure 1.3: Example for showing the importance of an ohmic contact with a low contact resistance using a typical p-n diode. (a) schematic of the cross-section of a p-n diode. (b) resistance representation of the p-n diode in (a), R_{C1} and R_{C2} are the ohmic contact resistances in anode and cathode. (c) resistance representation of an ideal p-n diode, R_{C1} and R_{C2} are small enough to be neglected. (d) the I-V curve of a p-n diode.

current transport

$$\rho_c \sim \left(\frac{1}{E_{00}}\right) exp\left(\frac{qV_{b0}}{E_{00}}\right) \tag{1.3}$$

where E_{00} is a reference energy related to the probability of tunneling

$$E_{00} = \frac{\hbar}{2}\sqrt{\frac{N}{\varepsilon_s m^*}} \tag{1.4}$$

Note that in equations 1.2-1.4, k is the Boltzmann constant, T is the temperature, q is the electrical charge, J_s is the saturation current density, V_{b0} is the built-in potential, $\hbar$ is the modified Planck constant, N is the doping concentration, ε_s is the semiconductor permittivity and m^* is the effective mass of a tunneling electron.

From equation 1.2 it can be seen that ρ_c will increase with decreasing temperature for the cases where TE dominates (Schottky contacts). For FE cases, however, from equation 1.3, it can be found that ρ_c strongly depends on the doping concentration.

1.3 Thesis Outline

This thesis initially discusses the conventional test structures for ohmic contact characterisation, following which, the novel techniques for determining ρ_c of contacts to both two-dimensional (2-D) semiconductor layers and bulk semiconductors are presented. The fabrication of the novel test structures is given in detail and the electrical testing results obtained by using the novel techniques are reported.

Chapter 2 reviews the most commonly used test structures for ohmic contact characterisation. The advantages and disadvantages of these conventional test structures are discussed as well.

Chapter 3 presents a novel two-contact circular test structure for determining ρ_c of contacts to 2-D semiconductor layers. The analytical expressions are developed and presented, and finite element modeling (FEM) results are presented to demonstrate the accuracy of the technique.

Chapter 4 introduces a novel method to extract ρ_c of contacts to bulk semiconductors (three-dimensional (3-D) circumstance) using the novel two-contact test structure presented in Chapter 3. This method is developed using FEM of ohmic contacts between a metal layer and a semiconductor substrate to obtain a series of universal curves to determine ρ_c. It was not possible to determine analytical expressions via a mathematical process.

Chapter 5 details the experimental conditions and parameters used for fabricating the novel test structures which are presented in Chapter 3 and 4. A number of metals were used to form ohmic contacts to epitaxial 3C-SiC, bulk Ge and bulk 4H-SiC with and without heat treatment.

Chapter 6 reports and analyses the electrical testing results obtained by testing the samples fabricated in Chapter 5 and using the new techniques presented in Chapter 3 and 4. Confidence in these new techniques is increased by demonstrating excellent agreement between analytical, FEM and testing results.

Chapter 7 summarises the results of this thesis and recommends the relevant areas for further research.

Appendices A to E present equation definitions, additional results tables, two-layer metal fabrication schedule and an alternative method using reduced analytical expressions to evaluate ρ_c using the novel two-contact circular test structure. In addition, a new test structure with a combination of transmission line model (TLM) and circular transmission line model (CTLM) for determining ρ_c of contacts to 2-D semiconductor layers is presented. This new structure is demonstrated using FEM.

1.4 Original Scientific Contributions

A summary of the major original contributions is listed below:

1. Developed and demonstrated a novel two-contact circular test structures for ohmic contact characterisation in 2-D circumstances (e.g. thin epitaxial layers) using FEM and experimental results.

2. Developed and demonstrated a novel methodology using two-contact circular test structure for ohmic contact characterisation in 3-D circumstances (e.g. thick epitaxial layers, bulk substrates) using FEM and experimental results.

3. Investigate the effect of low energy implantation on the properties of Au/Ni/Ti contacts to n-type epitaxial 3C-SiC using the novel test structures.

4. Report the ρ_c for Ni to heavily doped n-type epitaxial 3C-SiC ohmic contacts, Ti to lightly doped n-type epitaxial 3C-SiC, Au/Ni/Ti to ion implanted n-type epitaxial 3C-SiC, Ni to p-type Ge substrate and Ti to n-type 4H-SiC substrate using the novel test structures.

5. Develop and demonstrated a novel combined TLM-CTLM test structure for ohmic contact characterisation in 2-D circumstances using FEM.

Chapter 2

Ohmic Contact Test Structures

It is highly unlikely that electrical probes could be placed across a typical metal to semiconductor contact to determine specific contact resistivity ρ_c. Either the contact area will be too small to probe or if large enough, the contribution of ρ_c will be too small to be determined. Many ohmic contact test structures have been reported throughout the history of semiconductor devices and several of these are discussed in this chapter.

The experimentally determined values of ρ_c can vary widely by using different test structures and different methods used for extracting this parameter. The variation is also due to the fabrication conditions, material properties and so on. In this chapter, a number of the most commonly used ohmic contact test structures are reviewed and the advantages and disadvantages of these structures are also discussed.

2.1 Transmission Line Model

The transmission line model (TLM), as a two-terminal contact resistance test structure, was developed by [Shockley, 1964]. [Murrmann and Widmann, 1969] reported a detailed theoretical investigation of the TLM considering both semiconductor sheet resistance and contact resistance and presented a structure to de-

termine the specific contact resistivity. [Berger, 1969] started with the differential equations for the TLM and took special solutions for the conditions of interest independently in the same year. The TLM was then modified by [Berger, 1972], where he accounted for the finite depth of the semiconductor. Later on, [Reeves and Harrison, 1982] pointed out that there is a difference in the semiconductor sheet resistance underneath and outside the contact area and modifications were also introduced.

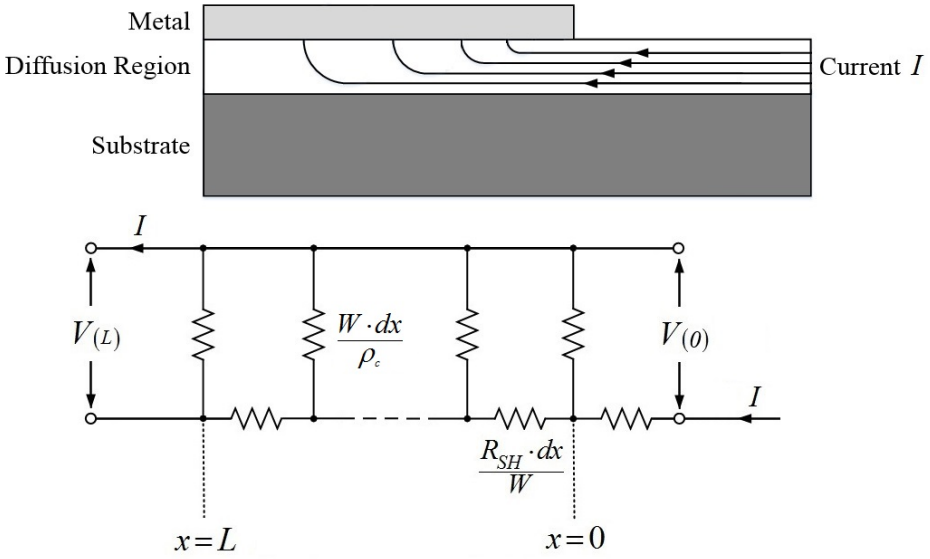

Figure 2.1: Comparison of a schematic of contact region with its transmission line resistor network model.

Fig. 2.1 shows a comparison of the cross section of a rectangular contact region with a transmission line resistor network model. The length of the contact is L and current I is injected into the edge of the diffusion region and flows out from the metal contact. The line equations for $V(x)$ and $I(x)$ in the TLM ohmic contact test structure were defined by [Berger, 1969] to describe the current and voltage distribution along the contact.

$$V(x) = V(0) \cosh \alpha x - I \cdot Z \sinh \alpha x \tag{2.1}$$

$$I(x) = I\cosh\alpha x - V(0)/Z\sinh\alpha x \tag{2.2}$$

where x is the distance from the leading contact edge, and Z is the characteristic line resistance

$$Z = \sqrt{\frac{R_{SH}}{W}\cdot\frac{\rho_c}{W}} = \frac{1}{W}\sqrt{R_{SH}\cdot\rho_c} \tag{2.3}$$

Here W is the width of the contact, R_{SH} and ρ_c are the semiconductor sheet resistance and the specific contact resistivity respectively.

α is the attenuation constant, the inverse of the transfer length L_T

$$\alpha = \frac{1}{L_T} = \sqrt{\frac{R_{SH}}{\rho_c}} \tag{2.4}$$

A TLM ohmic contact test structure with three identical contacts and different distances between them, is shown in Fig. 2.2. In the actual contacts, it is practically impossible to make the width of the contact W the same as the width of the diffusion area $W^{'}$. However the theory of the TLM ohmic contact test structure was developed assuming $W = W^{'}$ and error correction was later considered for $W < W^{'}$. Assuming $W = W^{'}$, then the total resistance R_1 is determined between the left two contacts to be

$$R_1 = \frac{R_{SH}\cdot d_1}{W'} + 2R_C \tag{2.5}$$

where

$$R_C = \frac{V(0)}{I} \tag{2.6}$$

With $I(L) = 0$, using equation 2.2, equation 2.6 can be written as

$$R_C = Z\coth\alpha L = \frac{\sqrt{R_{SH}\cdot\rho_c}}{W'}\coth\alpha L \tag{2.7}$$

Similarly

$$R_2 = \frac{R_{SH} \cdot d_2}{W'} + 2R_C \tag{2.8}$$

By subtracting R_1 from R_2, R_{SH} can be found

$$R_{SH} = \frac{W' \cdot (R_2 - R_1)}{d_2 - d_1} \tag{2.9}$$

Also, eliminate R_{SH} from equations 2.5 and 2.8, R_C can be found

$$R_C = \frac{R_1 \cdot d_2 - R_2 \cdot d_1}{2\,(d_2 - d_1)} \tag{2.10}$$

ρ_c can be found immediately using equations 2.4 and 2.7.

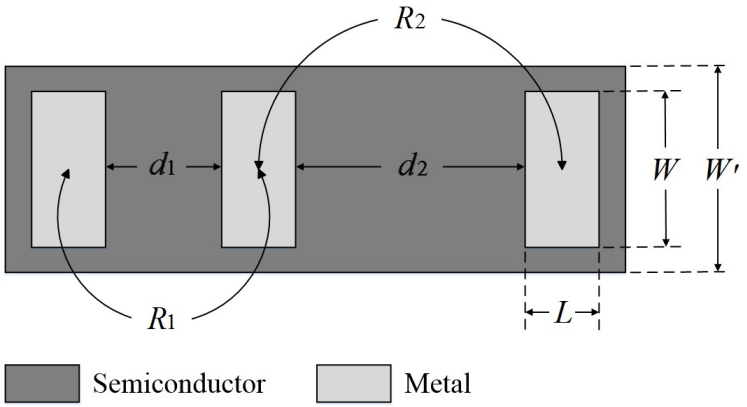

Figure 2.2: A test structure for determining ρ_c and R_{SH} using the TLM.

Because $W \neq W'$ in actual contacts, the equations discussed above only approximate the actual ρ_c and R_{SH}. The effect of this contact width approximation has been discussed by [Chang, 1970], [Ting and Chen, 1971] and [Berger, 1972].

Another inconvenience with using the TLM is the required mesa isolation (or selected (active) area diffusion). The diffusion region (or active region) has to be etched (or selectively formed) to ensure the required behavior of the current

flowing through the contacts. However, a number of compound semiconductors such as SiC and GaAs are very difficult to be etched. Therefore, other test structures that do not require a mesa etch are more desirable for characterising ohmic contacts to these materials. In any case, reducing the fabrication complexity is always an advantage.

2.2 Circular Transmission Line Model

The circular transmission line model (CTLM) is another well known two-terminal contact resistance test structure proposed by [Reeves, 1980]. The necessity of the mesa isolation of the contact patterns is eliminated using the CTLM and therefore, the pattern fabrication is simplified.

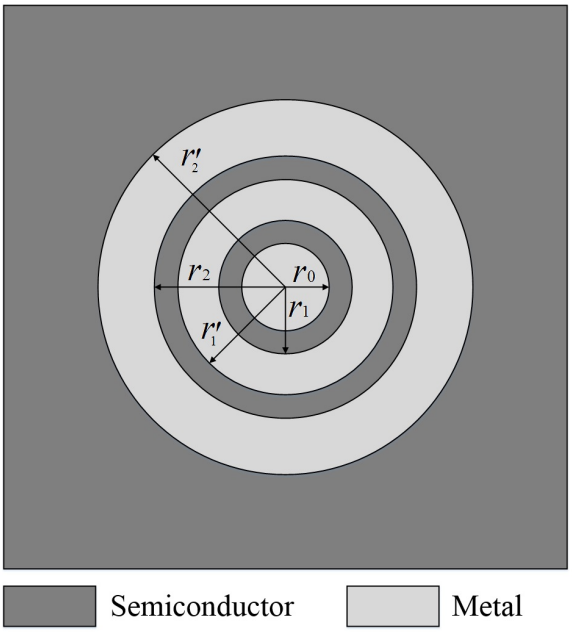

Figure 2.3: Plan view of the CTLM test structure.

Fig. 2.3 shows the CTLM test pattern which consists of a central dot contact and two concentric ring contacts. The radius of the central dot contact is r_0, the

inner and outer radii of the middle ring contact are r_1 and $r_1^{'}$ respectively, the inner and outer radii of the outer ring contact are r_2 and $r_2^{'}$ respectively.

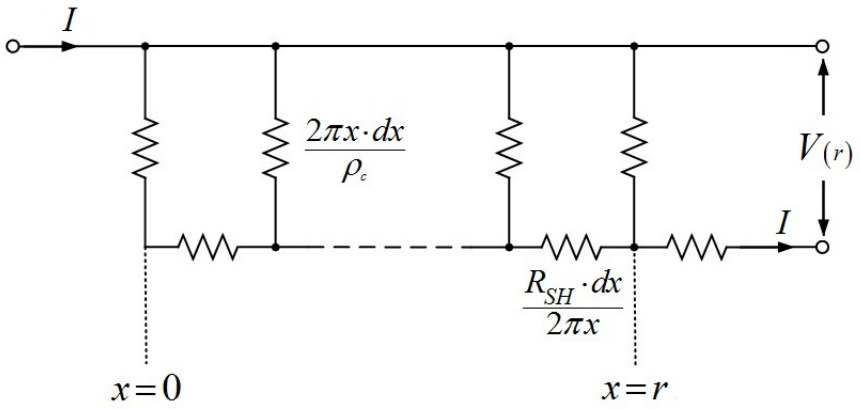

Figure 2.4: Resistor network model for the CTLM.

The sheet resistance beneath the contacts here is defined as R_{SK} [Kellner, 1975] to distinguish it from the normal sheet resistance R_{SH}. An alloyed ohmic contact to GaAs is an example of where $R_{SK} \neq R_{SH}$. Fig. 2.4 shows the resistor network model for the CTLM, as defined by [Reeves, 1980], the basic transmission line equations are

$$\frac{dV}{dx} = \frac{i\,(x) \cdot R_{SK}}{2\pi x} \tag{2.11}$$

$$\frac{di}{dx} = \frac{V\,(x) \cdot 2\pi x}{\rho_c} \tag{2.12}$$

where x is the distance from the central dot of the CTLM. $i(x)$ and $V(x)$ are the current flowing beneath the contact at x and the voltage drop across the contact interface at x respectively.

Eliminating $i(x)$ in equations 2.11 and 2.12, the differential equation for voltage

can be found

$$\frac{d^2V}{dx^2} + \frac{1}{x}\frac{dV}{dx} - \alpha^2 V = 0 \tag{2.13}$$

where α is the attenuation constant defined by equation 2.4.

The solution to equation 2.13 is [Commerce, 1972]

$$V(x) = aI_0(\alpha x) + bK_0(\alpha x) \tag{2.14}$$

Note that I_0 and K_0 are zeroth order modified Bessel functions of the first and second kind respectively and a and b are constants. By applying different boundary conditions, using equations 2.11, 2.12 and 2.14, the contact resistances for the central dot contact R_{C0} and the outer ring contact resistance R_{C2} can be written as

$$R_{C0} = \frac{R_{SK}}{2\pi\alpha r_0} \cdot E(r_0) \tag{2.15}$$

$$R_{C2} = \frac{R_{SK}}{2\pi\alpha r_2'} \cdot \frac{B(r_2', r_2)}{C(r_2, r_2')} \tag{2.16}$$

The functions such as $E(r_0)$ are defined in Appendix A.

The middle ring contact resistance depends on where the current flows into. When the current flows between the outer ring contact and the middle ring contact

$$R_{C1} = \frac{R_{SK}}{2\pi\alpha r_1} \cdot \frac{B(r_1, r_1')}{C(r_1, r_1')} \tag{2.17}$$

When the current flows between the middle ring contact and the central dot contact

$$R_{C1}' = \frac{R_{SK}}{2\pi\alpha r_1'} \cdot \frac{B(r_1', r_1)}{C(r_1, r_1')} \tag{2.18}$$

Hence, the total resistance between the central dot contact and the middle ring

contact R_1 and the total resistance between the middle ring contact and the outer ring contact R_2 can be written as

$$R_1 = R_A + R_{C0} + R_{C1}^{'} \tag{2.19}$$

$$R_2 = R_B + R_{C1} + R_{C2} \tag{2.20}$$

where R_A and R_B are the resistances due to the semiconductor rings between the central dot contact and the middle ring contact and the middle ring contact and the outer ring contact respectively

$$R_A = \frac{R_{SH}}{2\pi} \ln\left(\frac{r_1^{'}}{r_0}\right) \tag{2.21}$$

$$R_B = \frac{R_{SH}}{2\pi} \ln\left(\frac{r_2^{'}}{r_1}\right) \tag{2.22}$$

Taking the difference $R_1 - R_2$ (using equations 2.19 and 2.20), R_{SH} can be eliminated

$$\begin{aligned} \ln\left(\frac{r_2^{'}}{r_1}\right) \cdot R_1 - \ln\left(\frac{r_1^{'}}{r_0}\right) \cdot R_2 = \\ \ln\left(\frac{r_2^{'}}{r_1}\right) \cdot \left(R_{C0} + R_{C1}^{'}\right) - \ln\left(\frac{r_1^{'}}{r_0}\right) \cdot (R_{C1} + R_{C2}) \end{aligned} \tag{2.23}$$

The contact end resistance, R_E, is defined as the ratio of the contact output voltage V_{out} to the contact input current I_{in} when the contact output current is zero

$$R_E = \frac{V_{out}}{I_{in}} \tag{2.24}$$

Fig. 2.5 shows an example of the finite element modeling (FEM) of the CTLM (FEM will be discussed in detail later). An ohmic contact with a semiconductor sheet resistance (R_{SH}) and specific contact resistivity (ρ_c) values of 3000 $\Omega/\square$ and 1×10^{-4} $\Omega \cdot cm^2$ respectively, is used in this example. The equipotential of the middle ring electrode surface is set to zero, and the current is input at

the central dot electrode. Voltage is measured between the outer two electrodes. Using equation 2.24, R_E can be determined.

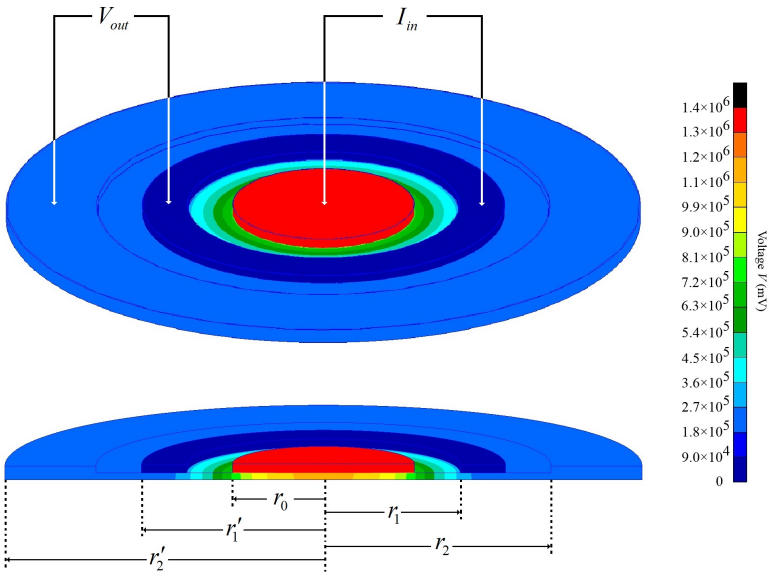

Figure 2.5: Measurement of R_E using equation 2.24. Equipotentials (in millivolts) in the semiconductor layer for the FEM example of the CTLM where $r_0 = 4\ \mu m$, $r_1 = 6\ \mu m$, $r_1^{'} = 8\ \mu m$, $r_2 = 10\ \mu m$ and $r_2^{'} = 14\ \mu m$ are presented. R_{SH} and ρ_c are 3000 $\Omega/\square$ and $1 \times 10^{-4}\ \Omega \cdot cm^2$ respectively.

The contact end resistance R_E for the central dot contact is given by [Reeves, 1980] as well

$$R_E = \frac{R_{SK}}{2\pi} \cdot \left[A\left(r_1, r_1^{'}\right) \cdot \frac{B\left(r_1, r_1^{'}\right)}{C\left(r_1, r_1^{'}\right)} + D\left(r_1, r_1^{'}\right) \right] \tag{2.25}$$

$R_{SK}/2\pi$ can then be canceled from equations 2.23 and 2.25

$$\left[\ln\left(\frac{r_2^{'}}{r_1}\right) \cdot R_1 - \ln\left(\frac{r_1^{'}}{r_0}\right) \cdot R_2 \right] \Big/ R_E = \phi \tag{2.26}$$

where ϕ is defined by the following equation according to equations 2.23 and 2.25

$$\phi = \left\{ \ln\left(\frac{r_2^{'}}{r_1}\right) \cdot \left[\frac{E\left(r_0\right)}{\alpha r_0} + \frac{1}{\alpha r_1^{'}} \cdot \frac{A\left(r_1, r_1^{'}\right)}{C\left(r_1, r_1^{'}\right)}\right] - \ln\left(\frac{r_1^{'}}{r_1}\right) \cdot \left[\frac{1}{\alpha r_1} \cdot \frac{B\left(r_1, r_1^{'}\right)}{C\left(r_1, r_1^{'}\right)} + \frac{1}{\alpha r_2} \cdot \frac{A\left(r_2, r_2^{'}\right)}{C\left(r_2, r_2^{'}\right)}\right] \right\} \Bigg/ \left[A\left(r_1, r_1^{'}\right) \cdot \frac{B\left(r_1, r_1^{'}\right)}{C\left(r_1, r_1^{'}\right)} + D\left(r_1, r_1^{'}\right)\right] \tag{2.27}$$

The value of ϕ can be experimentally determined with known geometries using equation 2.26 by plotting ϕ as a function of α using equation 2.27, α can then be found. With known α and ϕ, using equation 2.28, ρ_c can be determined.

$$\rho_c = \left[\ln\left(\frac{r_2^{'}}{r_1}\right) \cdot R_1 - \ln\left(\frac{r_1^{'}}{r_0}\right) \cdot R_2\right] \cdot r_0^2 \cdot \Delta \tag{2.28}$$

where Δ is

$$\Delta = \frac{2\pi}{\left(\alpha r_0\right)^2 \cdot \phi} \Bigg/ \left[A\left(r_1, r_1^{'}\right) \cdot \frac{B\left(r_1, r_1^{'}\right)}{C\left(r_1, r_1^{'}\right)} + D\left(r_1, r_1^{'}\right)\right] \tag{2.29}$$

Obviously, although the fabrication is simplified by using the CTLM, the analytical expressions for determining ρ_c are quite complicated. [Hewett et al., 1995] reduced the expressions by considering the asymptotic expressions for the modified Bessel functions and assuming $R_{SK} = R_{SH}$ (the sheet resistance beneath the contacts being the same as the sheet resistance between the contacts). However, these reduced expressions are not universal and depend on the contact geometries and the contact materials. Another problem is the difficulty of probing on and keeping the middle ring contact at an equipotential since it is very narrow compared to the central dot and the outer ring contacts. This effect will lead to an error in the derivation of the value of ρ_c.

2.3 Cross-Bridge Kelvin Resistor Test Structure

The most commonly used four-terminal contact resistance test structure is the cross-bridge Kelvin resistor (CBKR) test structure. This structure was initially proposed by [Shih and Blum, 1972] and then used extensively by [Cohen et al., 1982], [Proctor and Linholm, 1982] and [Mazer et al., 1985]. This technique allows ρ_c to be determined without being affected by a semiconductor region between two contacts. Fig. 2.6 illustrates the principle of this method. The structure consists of two L-shape regions (with width of d) which are the underlying semiconductor and the metal conductor on the surface respectively.

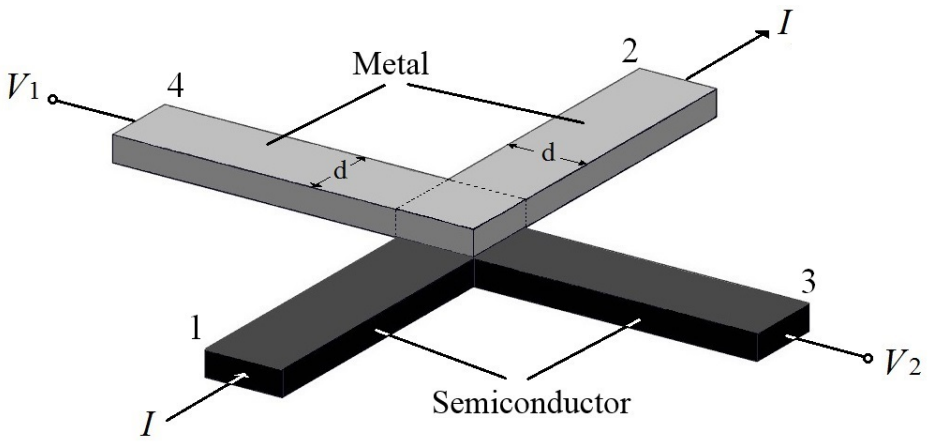

Figure 2.6: Isometric view of the ideal cross-bridge Kelvin test structure.

Current I is forced between terminals 1 and 2 and the voltage difference is measured between terminals 3 and 4. The contact resistance can be determined

$$R_C = \frac{V_{34}}{I_{12}} \tag{2.30}$$

The specific contact resistivity is then determined

$$\rho_c = R_C \cdot A \tag{2.31}$$

where A is the contact area that is shown as the area where the two L-shape

materials overlap in Fig. 2.6.

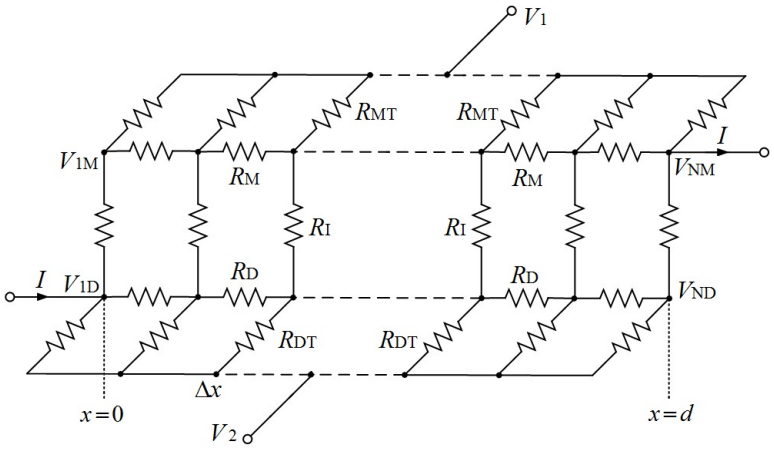

Figure 2.7: Resistor network model for the contact area shown in Fig. 2.6 [Proctor and Linholm, 1982].

Fig. 2.7 is the resistor network model of the ideal CBKR presented by [Proctor and Linholm, 1982]. The model consists of N stages of metal resistors R_M, interfacial resistors R_I and semiconductor resistors R_D which are defined as

$$R_M = \frac{R_{SM} \cdot \Delta x}{d} \tag{2.32}$$

$$R_I = \frac{\rho_c}{d \cdot \Delta x} \tag{2.33}$$

$$R_D = \frac{R_{SD} \cdot \Delta x}{d} \tag{2.34}$$

Note that d is the contact length, Δx is the incremental length of each of the N stages and R_{SM} and R_{SD} are the sheet resistances of the metal and semiconductor layers in the contact region respectively. Hence, N can be written as

$$N = \frac{d}{\Delta x} \tag{2.35}$$

The semiconductor voltage tap consists of N parallel resistors of value R_{DT}. Similarly, the metal voltage tap consists of N parallel resistors of value R_{MT}.

Since there is no net current flowing into the voltage taps, the sum of the current in the parallel resistors is zero

$$\sum_{j=1}^{N} \frac{V_{jM} - V_1}{R_{MT}} = 0 \tag{2.36}$$

$$\sum_{j=1}^{N} \frac{V_{jD} - V_2}{R_{DT}} = 0 \tag{2.37}$$

Note that $V_{jM} - V_1$ and $V_{jD} - V_2$ are the voltages across the j^{th} metal tap resistor and semiconductor tap resistor respectively. The voltage difference between the two taps is

$$V_2 - V_1 = \frac{1}{N} \sum_{j=1}^{N} (V_{jD} - V_{jM}) \tag{2.38}$$

Because all the current injected into the structure must pass through the contact

$$I = \sum_{j=1}^{N} \frac{V_{jD} - V_{jM}}{R_I} = \frac{N}{R_I} (V_2 - V_1) \tag{2.39}$$

Hence

$$R_C = \frac{V_2 - V_1}{I} = \frac{R_I}{N} \tag{2.40}$$

$$\rho_c = R_C \cdot A = \frac{V_2 - V_1}{I} \cdot A \tag{2.41}$$

Fig. 2.6 shows the ideal CBKR test structure where the size of the contact window between metal and semiconductor is exactly the same as the diffusion tap (the two L-shape materials overlap), that is, $\delta = 0$ in Fig. 2.8. In an actual contact, however, the contact window is usually smaller than the diffusion tap ($\delta > 0$). Therefore, the lateral current flow will lead to an additional voltage drop affecting the value of V_{34}. The higher value of V_{34} will result in a higher R_C. If we consider A as the actual area, according to equation 2.31, ρ_c is also higher. The extracted inaccurate ρ_c is also known as the effective specific contact resistivity. [Finetti

et al., 1984] pointed that this error due to the geometrical factor will be smaller for high L_T and greater for low L_T. Correction curves are used to correct the effective specific contact resistivity to obtain the true value of ρ_c [Loh et al., 1987].

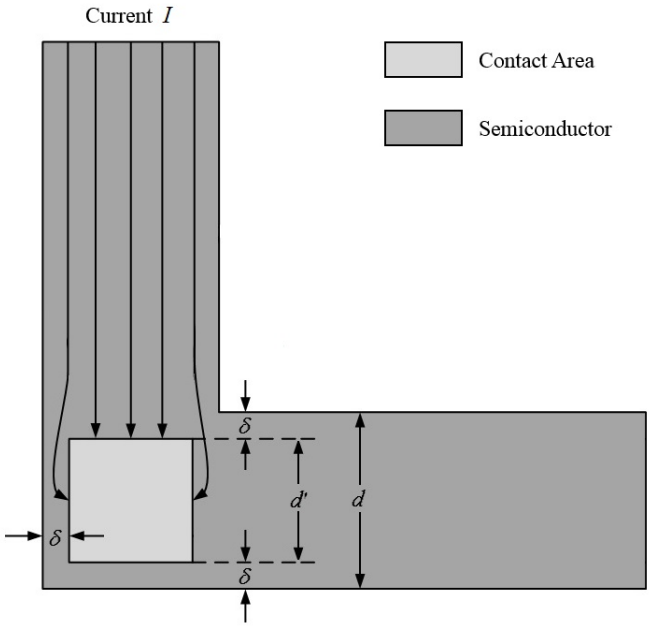

Figure 2.8: Current flows into and around the contact in an actual CBKR model.

The contact misalignment and the vertical voltage drop in the semiconductor are also issues to consider when using the CBKR. [Ono et al., 2002] and [Holland et al., 2004] have discussed these issues and give solutions.

2.4 Summary

The most commonly used ohmic contact test structures were reviewed. The methods used with these test structures for extracting ρ_c were also discussed. As a two-terminal contact resistance test structure, the TLM has relatively very simple analytical equations for extracting ρ_c. However, the necessity of mesa isolation (or other process for defining active layers) makes the fabrication difficult

practically for semiconductors that are difficult to etch (when investigating ohmic contacts to epitaxial layer for example). The CTLM is another two-terminal contact resistance test structure. Without mesa etch, the fabrication is simplified but the heavy analytical expressions make the derivation of ρ_c quite complicated. How to keep the middle ring contact at an equipotential is also a problem for the CTLM. The CBKR, a four-terminal contact resistance test structure was also discussed. The analytical equations for extracting ρ_c using the CBKR are relatively simple but a mesa etch (or selective area doping to define the test structure active area) is required. Furthermore, correction curves have to be used to obtain the true value of ρ_c because fabrication tolerances require the contact area to be overlapped by the active semiconductor area.

Chapter 3

Two-Contact Circular Test Structure for Determining Specific Contact Resistivity of Contacts to 2-D Semiconductor Layers

A new test structure, based on the conventional circular transmission line model (CTLM) and also using a series of contact pairs of different spacings to determine the specific contact resistivity, ρ_c, is presented. There is no correction factor process and a mesa etch is unnecessary. Furthermore, the measurements are simplified, compared to the standard CTLM pattern based on three electrodes. The new structure removes the middle ring contact, which can be difficult to probe and to maintain as an equipotential.

3.1 The Two-Contact Circular Model

The two-contact circular test pattern for determining ρ_c is shown in Fig. 3.1 where the radius of the central dot contact is r_0 and the inner and outer radii of the outer contact are r_1 and $r_1^{'}$ respectively. The radius of the outer circle $r_1^{'}$ can be taken to be infinite beyond a certain value (discussed later). The sheet

resistance of the metallic layer is assumed to be zero (as stated in Section Future Research, finite resistivity of the metal can be further investigated using suggested structures).

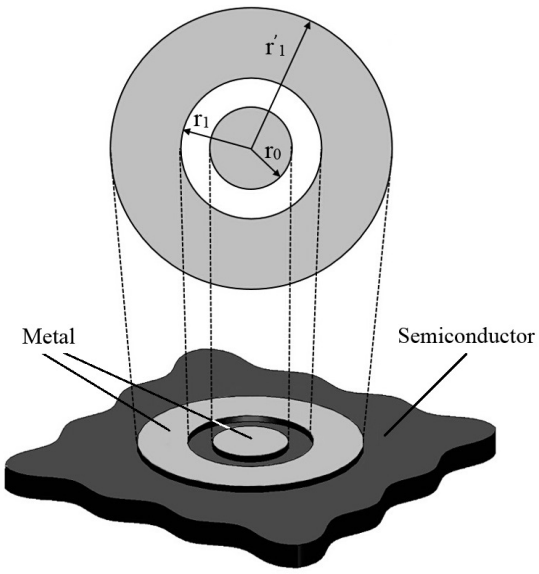

Figure 3.1: Isometric view of the two-contact circular test structure. Total resistance R_T is measured between the central dot and the outer electrode.

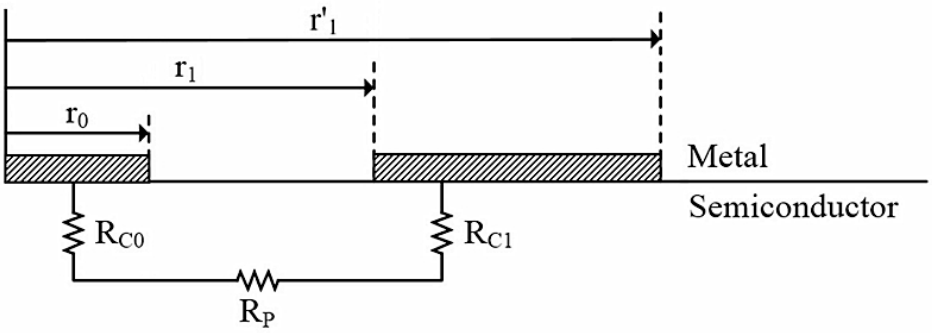

Figure 3.2: Schematic illustration of the two-contact circular test structure. Total resistance R_T consists of R_{C0}, R_P and R_{C1}.

Fig. 3.2 shows the resistance representation of the model in Fig. 3.1. When

current is injected into the central dot and flows out from the outer contact, the total resistance, R_T, between the central dot and the outer electrode can be determined by measuring the voltage between the two electrodes

$$R_T = \frac{V}{I} \tag{3.1}$$

As shown in equation 3.1, R_T consists of the central dot contact resistance, R_{C0}, R_P, which is due to the semiconductor layer and the outer electrode contact resistance R_{C1}.

$$R_T = R_{C0} + R_P + R_{C1} \tag{3.2}$$

The components of the analytical model for R_T are determined as follows:

A. Central Dot Contact Resistance R_{C0}

As defined by [Reeves, 1980], the contact resistance for a circular electrode with symmetric concentric current distribution is

$$R_{C0} = \frac{R_{SH}}{2\pi\alpha r_0} \frac{I_0(\alpha r_0)}{I_1(\alpha r_0)} \tag{3.3}$$

where α is defined as

$$\alpha^2 = \frac{R_{SH}}{\rho_c} \tag{3.4}$$

I_0 and I_1 are the zeroth and first order modified Bessel functions of the first kind respectively [Commerce, 1972]. Note that α is the inverse of transfer length, L_T, in the linear transmission line model (TLM) for ohmic contacts.

B. Resistance R_P Due to Semiconductor Layer

As reported in [Reeves, 1980], the semiconductor ring of sheet resistance, R_{SH}, as shown in Fig. 3.1 has a resistance of

$$R_P = \frac{R_{SH}}{2\pi} \ln\left(\frac{r_1}{r_0}\right) \tag{3.5}$$

C. Outer Area Contact Resistance R_{C1}

The outer electrode contact resistance is given by equation 3.6 in [Reeves, 1980]

$$R_{C1} = \frac{R_{SH}}{2\pi\alpha r_1} \frac{\left[I_1\left(\alpha r_1'\right) K_0\left(\alpha r_1\right) + I_0\left(\alpha r_1\right) K_1\left(\alpha r_1'\right)\right]}{\left[I_1\left(\alpha r_1'\right) K_1\left(\alpha r_1\right) - I_1\left(\alpha r_1\right) K_1\left(\alpha r_1'\right)\right]} \tag{3.6}$$

where K_0 and K_1 are the zeroth and first order modified Bessel functions of the second kind respectively. This equation (as well as equation 3.3 and equation 3.5) fully describes the resistances in a two-dimensional (2-D) ohmic contact structure, i.e., where R_{SH} only is required to describe the contribution of the semiconductor layer to the total resistance R_T.

3.2 Modeling of The Two-Contact Circular Test Structure

Finite element modeling (FEM) can be used to accurately model the electrical behavior of ohmic contacts between a metal and a semiconductor. Forming a model requires information on contact structure geometry, conductivity of each layer in the structure, and ρ_c of each interface in the structure [Holland et al., 2009]. MSC Nastran and Patran software are used to model the two-contact circular test structure. MSC Nastran is a finite element program developed by NASA for heat transfer analysis, mechanical analysis and so on while MSC Patran is used for creating models and meshing. However, voltage distribution in materials can also be obtained by using MSC Nastran because the equation for electrical current transfer (Ohms Law) is analogous to that of the heat transfer (Fourier's Law). Electrical properties and their thermal equivalents are shown as follows:

(i) Voltage $(V) \rightleftharpoons$ Temperature (T)

(ii) Current density $(J) \rightleftharpoons$ Heat density (H)

(iii) Electrical conductivity $(\sigma) \rightleftharpoons$ Thermal conductivity (K)

The equation for heat transfer and its electrical equivalent for current density are

$$H = K \cdot \nabla T \tag{3.7}$$

$$J = \sigma \cdot \nabla V \tag{3.8}$$

The parameter settings for a two-contact circular model in MSC Patran are given in Table 3.1. As shown in Table 3.1, the interface between the semiconductor and metal where the ρ_c of the ohmic contact is ascribed, is given a finite thickness of 0.02 μm, which is reasonable for a depletion region. An ohmic contact with a semiconductor sheet resistance (R_{SH}) and ρ_c values of 3000 $\Omega/\square$ and 1×10^{-4} $\Omega \cdot cm^2$ respectively, is used as an example to compare the analytical model and FEM results [Nasir et al., 2012]. These parameters are typical of SiC which is very difficult to etch, and hence, the CTLM techniques are more convenient to use for determining ρ_c.

Table 3.1: Parameter settings for the two-contact circular test structure in MSC Patran. $R_{SH} = 3000$ $\Omega/\square$ and $\rho_c = 1 \times 10^{-4}$ $\Omega \cdot cm^2$. r_0 is from 1 μm to 5 μm. r_1 is kept at 1.5 times the value of r_0. $r_1^{'}$ is kept at 10 times the value of r_0 (discussed later).

Symbol	Metal Layer	Interface	Semiconductor Layer
t[1]	0.285	0.02	0.285
σ[2]	100	2×10^{-6}	1.17×10^{-3}

[1] thickness [μm].
[2] electrical conductivity [$1/\Omega \cdot \mu m$].

Fig. 3.3 shows a section of the three-dimensional (3-D) finite element mesh used to model this two-contact circular test structure. In the model, each metal contact is assumed to be an equipotential, and this implies zero sheet resistance for the metal layer. Various FEM models (different dimensions and material properties) of this structure were modeled with the values of r_0 varying from 1 to 5 μm, and the corresponding values of r_1 from 1.5 to 7.5 μm. r_1 was kept at 1.5 times the value of r_0 (to keep the contribution of R_P to the total resistance R_T small). The values of $r_1^{'}$ are 10 times greater than r_1 in the model (when $r_1^{'}$ is beyond a certain value, it does not matter that the outer ring contact shown in

Fig. 3.1 as a ring, is not a ring). The factor of 10 times greater is suitably large. In order to reduce the time taken for analysis, only a 45° sector is modeled. The equipotential of the outer electrode surface is set to zero, and the current is input at the central dot electrode.

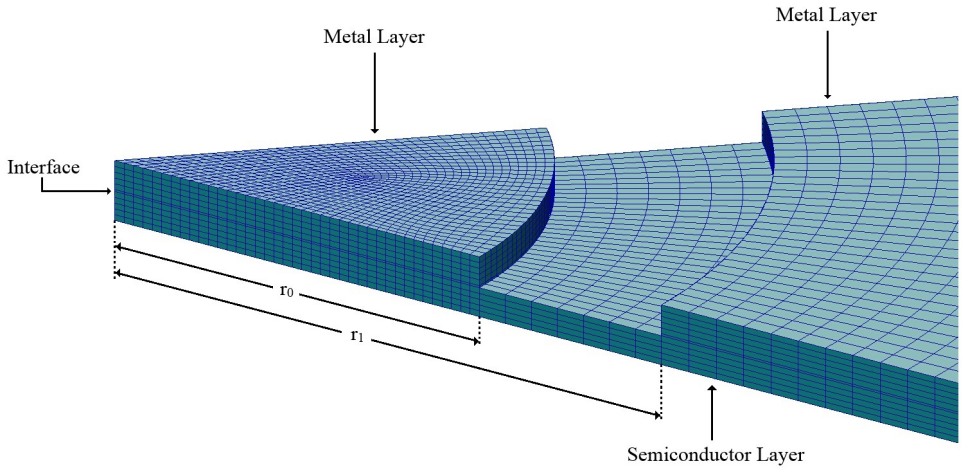

Figure 3.3: Finite element mesh used to model the two-contact circular test structure. $r_0 = 4\ \mu m$, $r_1 = 6\ \mu m$, and $r_1^{'} = 40\ \mu m$. R_{SH} and ρ_c are 3000 $\Omega/\square$ and $1 \times 10^{-4}\ \Omega \cdot cm^2$ respectively (a 45° sector of the test structure is presented and Fig. 3.1 is a schematic of the full test structure).

Fig. 3.4 shows the equipotentials and structure geometry for analysis where $r_0 = 4\ \mu m$, $r_1 = 6\ \mu m$, and $r_1^{'} = 40\ \mu m$ and Fig. 3.5 illuminates the current densities for analysis of the same model.

R_{C0} from the FEM is obtained by determining the difference between the equipotential below the leading edge of the central dot electrode and the equipotential of the dot electrode. R_{C0} from the model is then determined by dividing this potential difference by the input current.

Fig. 3.6 shows a comparison of calculations by FEM with analytical results obtained using equation 3.3 for R_{C0}. It is seen that the FEM results match equation 3.3 very well for the plotted range of $0 \leq \alpha r_0 \leq 10$ which covers all practical values of α.

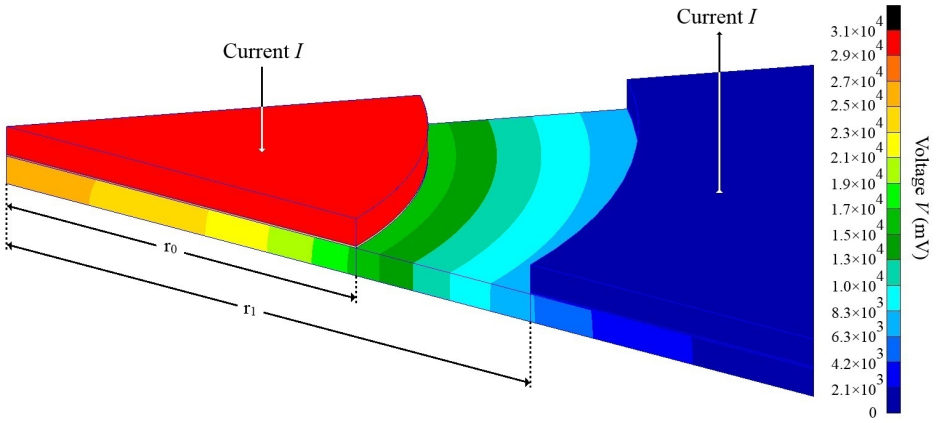

Figure 3.4: Equipotentials (in millivolts) in the semiconductor layer for the FEM example where $r_0 = 4\ \mu m$, $r_1 = 6\ \mu m$, and $r_1^{'} = 40\ \mu m$. R_{SH} and ρ_c are 3000 $\Omega/\square$ and $1 \times 10^{-4}\ \Omega \cdot cm^2$ respectively (a 45° sector of the test structure is presented and Fig. 3.1 is a schematic of the full test structure).

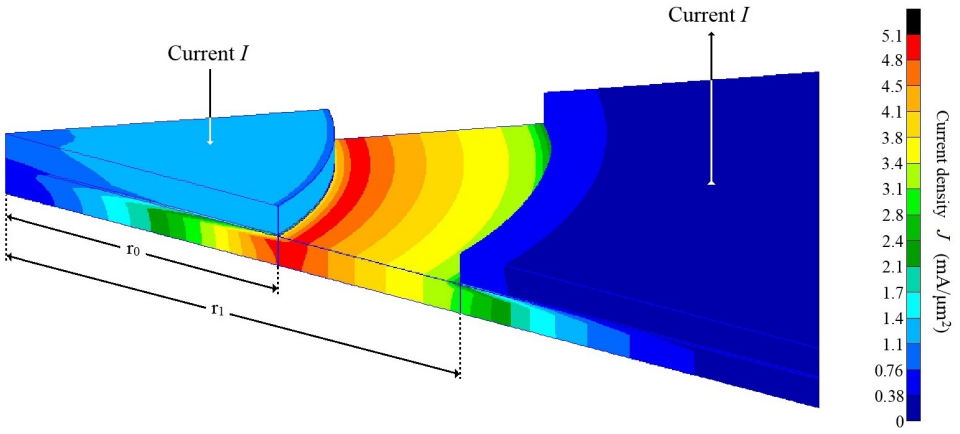

Figure 3.5: Current densities (in milliamperes per square micrometers) in the semiconductor layer for the FEM example where $r_0 = 4\ \mu m$, $r_1 = 6\ \mu m$, and $r_1^{'} = 40\ \mu m$. R_{SH} and ρ_c are 3000 $\Omega/\square$ and $1 \times 10^{-4}\ \Omega \cdot cm^2$ respectively (a 45° sector of the test structure is presented and Fig. 3.1 is a schematic of the full test structure).

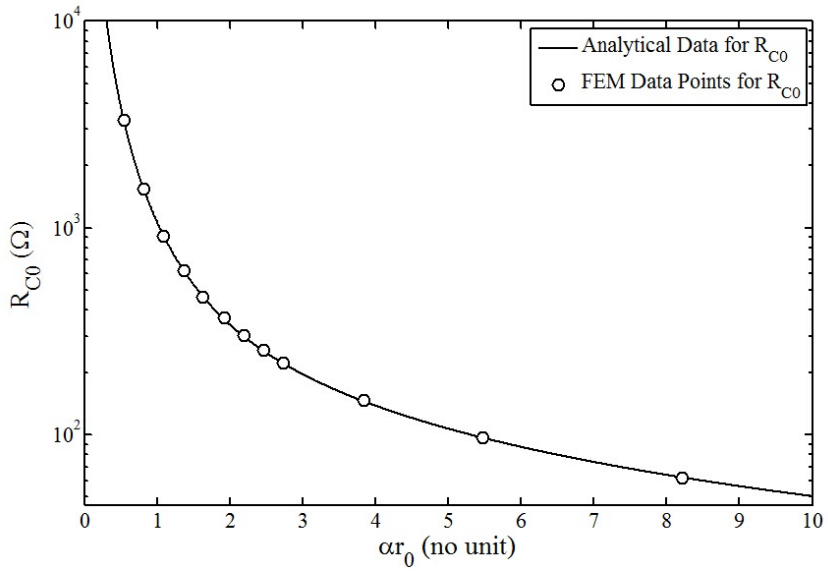

Figure 3.6: Central dot contact resistance R_{C0} versus αr_0 for the test structure shown in Fig. 3.1 (ranging from zero to ten). Analytical results for R_{C0} using equation 3.3 and FEM data points are presented. $R_{SH} = 3000\ \Omega/\square$ and $\rho_c = 1 \times 10^{-4}\ \Omega \cdot cm^2$.

R_P is a constant of 193.7 Ω because r_1/r_0 is fixed at 1.5 and the constant value of R_P is obtained from equation 3.5 which here (in this example) only has fixed values. The FEM results for R_P are in excellent agreement with equation 3.5. The difference for R_P is less than 0.6%.

R_{C1} from the FEM is obtained from the potential difference between the semiconductor at r_1 and the electrode surface. Like R_{C0} from the FEM, the equipotentials below the leading edge are almost vertical (see Fig. 3.4). R_{C1} from the FEM is determined by dividing this potential difference by the input current, I.

The comparison of the analytical results from equation 3.6 and from the FEM models for the outer contact resistance, R_{C1}, is shown in Fig. 3.7. The results are in good agreement for $0 \leq \alpha r_0 \leq 10$ which covers the most practical values of αr_0.

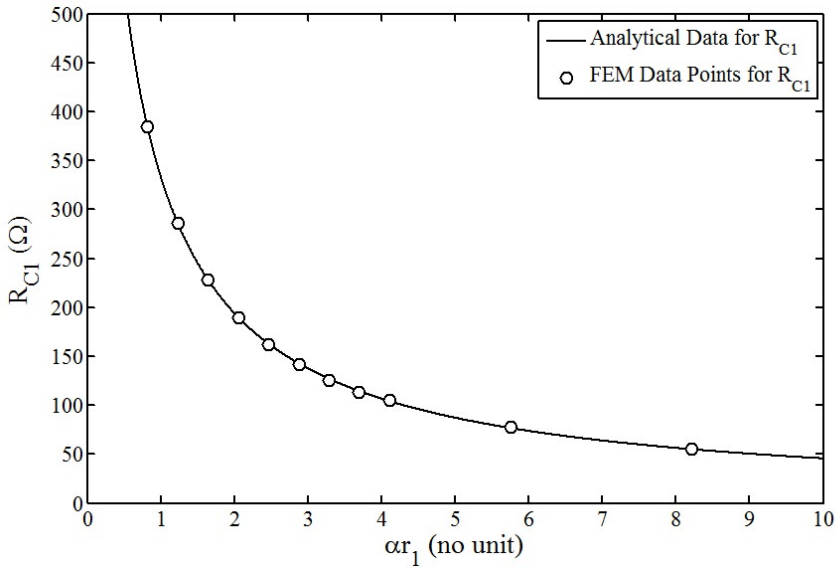

Figure 3.7: Outer area contact resistance R_{C1} versus αr_1 for the test structure shown in Fig. 3.1 (ranging from zero to ten). Analytical results using equation 3.6 and FEM data points are presented. $R_{SH} = 3000\ \Omega/\square$, $\rho_c = 1 \times 10^{-4}\ \Omega \cdot cm^2$, $r_1/r_0 = 1.5$, and $r_1^{'}/r_1 = 10$.

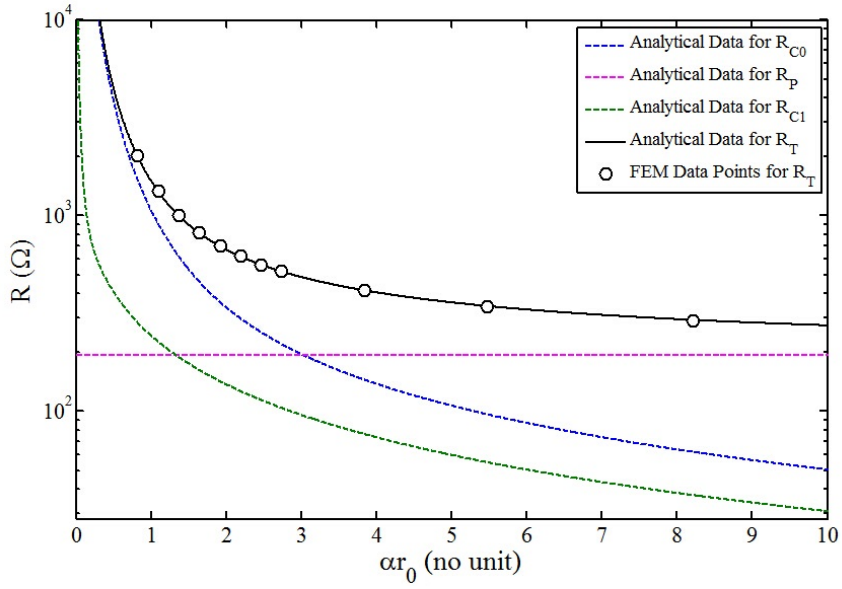

Figure 3.8: Comparison of R_{C0}, R_P, R_{C1}, R_T as a function of αr_0 for the test structure shown in Fig. 3.1 (in the range from zero to ten). $R_{SH} = 3000\ \Omega/\square$, $\rho_c = 1 \times 10^{-4}\ \Omega \cdot cm^2$, $r_1/r_0 = 1.5$ and $r_1^{'}/r_1 = 10$.

In Fig. 3.8, the three components of R_T are plotted. From the figure, the analytical and FEM results are in good agreement for increasing αr_0. As αr_0 increases (to ≥ 4), R_T does not change much and approaches R_P. Inspection of equations 3.3, 3.5 and 3.6 shows that the general case is that R_T approaches R_P when $\alpha r_0 \gg 1/\ln(r_1/r_0)$.

3.3 Methodology to Extract Specific Contact Resistivity Using The Two-Contact Circular Test Structure

The complete test pattern used to extract ρ_c is shown in Fig. 3.9. The structure consists of three central dot electrodes surrounded by a metal plane. The inner radius r_1 of the outer contact is the same for all three patterns. With regard to $r_1^{'}$ of Fig. 3.1 and equation 3.6, the question arises as to what should be the minimum spacing between the three contact structures in Fig. 3.9 (this figure is effectively three of the structure shown in Fig. 3.1 but with the outer electrode having an infinite outer radius). They should be far enough away from each other that the effective $r_1^{'}$ for each is infinite. In this context, the minimum value for $r_1^{'}$ depends on α (or $L_T = 1/\alpha$) and r_1. Investigation of equation 3.6 shows that for $r_1^{'} - r_1 > 5L_T$ (beyond $5L_T$ it does not matter that the outer contact as shown in Fig. 3.1, is not a ring), the value of R_{C1} remains unchanged. α is of course unknown but for practical values of R_{SH} and ρ_c and known L_T, a value of $r_1^{'} - r_1 > 50\ \mu m$ is ample. Hence, the suggested distance between adjacent structures in Fig. 3.9 is 50 μm.

The relationship between r_{01}, r_{02} and r_{03} are given by equations 3.9 and 3.10:

$$\frac{r_{02}}{r_{01}} = x \tag{3.9}$$

$$\frac{r_{03}}{r_{01}} = y \tag{3.10}$$

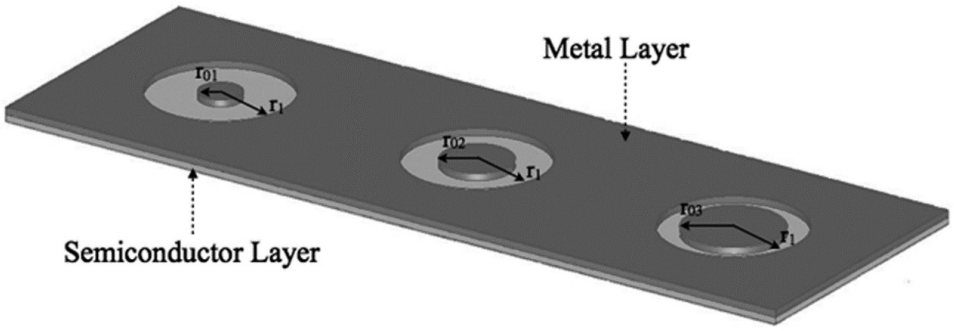

Figure 3.9: Structure used to extract R_{SH} and ρ_c. It consists of three pairs of two-contact circular test structures with different radii of the central dots.

Determining the resistance between the central dot and the outer electrode for each of the three contact structures in Fig. 3.9

$$R_{T1} = R_{C01} + R_{P1} + R_{C1} \tag{3.11}$$

$$R_{T2} = R_{C02} + R_{P2} + R_{C1} \tag{3.12}$$

$$R_{T3} = R_{C03} + R_{P3} + R_{C1} \tag{3.13}$$

Hence

$$R_{T1} - R_{T3} = (R_{P1} - R_{P3}) + (R_{C01} - R_{C03}) \tag{3.14}$$

Substituting equations 3.3 and 3.5 into equation 3.14, we get:

$$R_{T1} - R_{T3} = \frac{R_{SH}}{2\pi}\left(\ln y + F'\right) mm \tag{3.15}$$

where

$$F' = \frac{I_0\left(\alpha r_{01}\right)}{\alpha r_{01} I_1\left(\alpha r_{01}\right)} - \frac{I_0\left(\alpha r_{03}\right)}{\alpha r_{03} I_1\left(\alpha r_{03}\right)} \tag{3.16}$$

Similarly,

$$R_{T1} - R_{T2} = (R_{P1} - R_{P2}) + (R_{C01} - R_{C02}) = \frac{R_{SH}}{2\pi} (\ln x + F) \tag{3.17}$$

where

$$F = \frac{I_0 (\alpha r_{01})}{\alpha r_{01} I_1 (\alpha r_{01})} - \frac{I_0 (\alpha r_{02})}{\alpha r_{02} I_1 (\alpha r_{02})} \tag{3.18}$$

Let K be the ratio of R_{T1} - R_{T3} and R_{T1} - R_{T2}:

$$K = \frac{R_{T1} - R_{T3}}{R_{T1} - R_{T2}} = \frac{F' + \ln y}{F + \ln x} \tag{3.19}$$

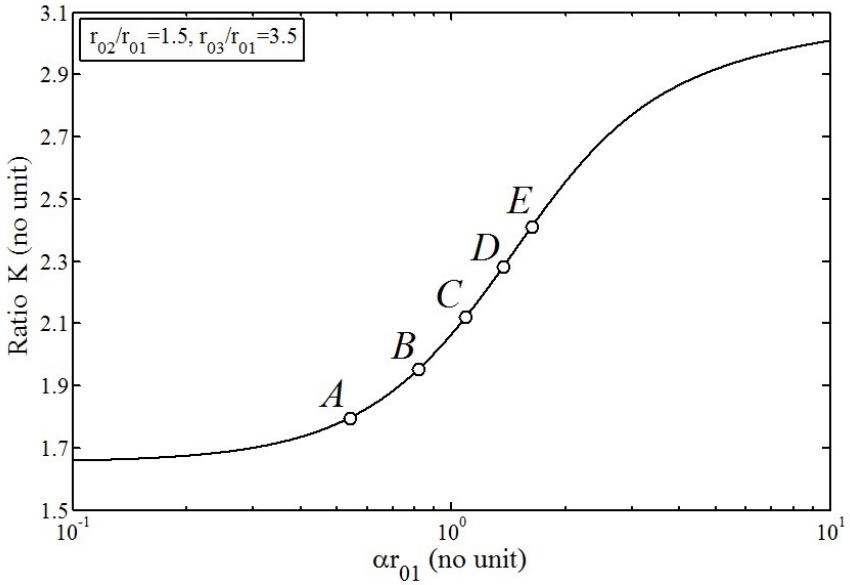

Figure 3.10: The ratio K versus αr_{01} for given ratios of radii $r_{02}/r_{01} = 1.5$, and $r_{03}/r_{01} = 3.5$. Points A, B, C, D and E correspond to r_{01}, being 1 μm, 1.5 μm, 2 μm, 2.5 μm and 3 μm respectively.

In order to extract ρ_c from the given structure, $x = 1.5$ and $y = 3.5$ were used because these ratios give workable K versus αr_{01} curves. In Fig. 3.10, r_{01} varies from 1 μm, 1.5 μm, 2 μm, 2.5 μm to 3 μm and the points A to E mark the location of the five sets of data obtained from FEM models of these structures.

The solid line indicates the ratio K as a function of αr_{01}. The graphic illustrates how to get αr_{01} and hence α values using experimentally determined K values and the corresponding αr_{01} values for points A to E are 0.54, 0.82, 1.09, 1.37 and 1.63 respectively in this example.

Fig. 3.11 shows how to get the values of $F^{'}$ using the αr_{01} values obtained in Fig. 3.10. Points $A^{'}$ to $E^{'}$ represent points A to E in Fig. 3.10 and the corresponding $F^{'}$ values obtained in Fig. 3.10 are 6.2, 2.8, 1.6, 1.1 and 0.8 respectively.

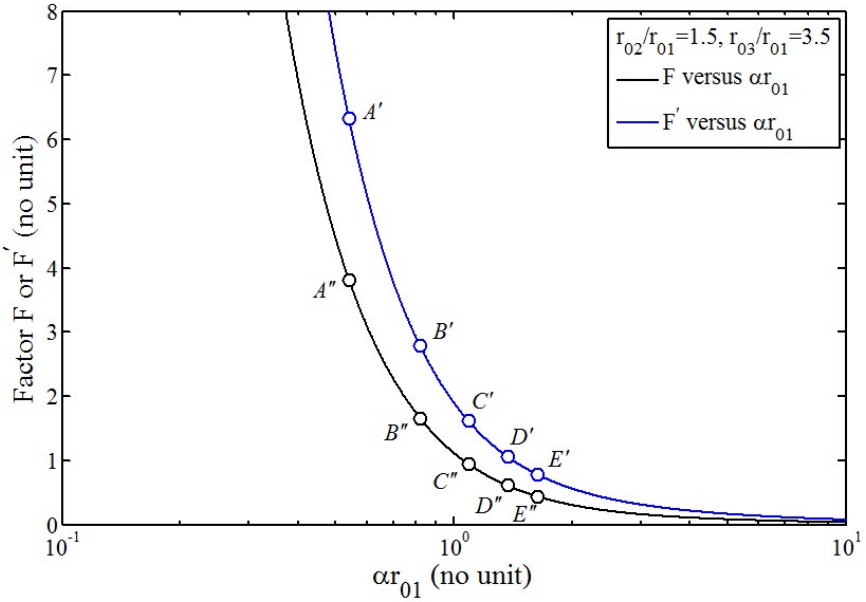

Figure 3.11: F and $F^{'}$ versus αr_{01} for given ratios of radii ($r_{02}/r_{01} = 1.5$, and $r_{03}/r_{01} = 3.5$). Points $A^{'}$ to $E^{'}$ and $A^{''}$ to $E^{''}$ represent points A to E in Fig. 3.10.

R_{SH} is calculated from equation 3.15 once $F^{'}$ is known. Using equation 3.4, ρ_c can now be found. In this example the extracted ρ_c using the five sets of data obtained by FEM are very close to the given ρ_c in FEM. The difference for ρ_c is less than 2%. This small error is likely due to the finite depth of the semiconductor layer [Holland et al., 1997] in the FEM model. Fig. 3.11 also shows F as a function of αr_{01}. An alternative way to extract ρ_c is by determining F using points $A^{''}$ to $E^{''}$. Also, it can be used to verify the value of ρ_c obtained using $F^{'}$.

Note that the contact resistances for any size area contact can be determined using the analytical equations 3.3, 3.4 and 3.6. When ρ_c and R_{SH} are determined for a particular contact making process, the contact resistance for a contact of any area, made with this process, can be determined using these equations.

For the circular test structure presented here, r_0, r_1, $r_1^{'}$, R_{SH} and ρ_c determine the total resistance R_T. Results show that analytical equations can be used to determine ρ_c if R_T is measured and ρ_c and R_{SH} are the only unknown parameters. In order to verify that the structure is universal, R_{SH} and ρ_c are scaled by factors m and n respectively. By using equations 3.2, 3.3, 3.5 and 3.6, the total resistance can be written in the following form

$$R_T\left(mR_{SH}, n\rho_c, \frac{\sqrt{n}}{\sqrt{m}}r_0, \frac{\sqrt{n}}{\sqrt{m}}r_1, \frac{\sqrt{n}}{\sqrt{m}}r_1^{'}\right) = mR_T\left(R_{SH}, \rho_c, r_0, r_1, r_1^{'}\right) \quad (3.20)$$

Equation 3.20 is similar to the scaling equation reported in [Loh et al., 1985] for the cross-bridge Kelvin resistor (CBKR) test structure. Examination of equations 3.16, 3.18, 3.19 and 3.20 shows that scaling R_{SH} and ρ_c will not change the plots in Fig. 3.10 and Fig. 3.11 and the shape of the plots in Fig. 3.6-Fig. 3.8 will also be the same with the Y-axis scaled by a factor of m. (Equation 3.20 was confirmed by using FEM and analytical modeling). Thus, the structure is universal and applicable for ohmic contacts where the resistive effects of the semiconductor layer and the contact interface can be described by R_{SH} and ρ_c respectively and by the geometry of the electrodes in the test structure. Scaling may be used to determine appropriate values of r_0 so that suitable points are obtained on the F versus αr_{01} or $F^{'}$ versus αr_{01} curves. With $m = n = 0.001$, equation 3.20 shows that the example geometry used here could also be used for $R_{SH} = 3\ \Omega/\square$ and $\rho_c = 1 \times 10^{-7}\ \Omega \cdot cm^2$. Figs. 3.10 and 3.11 would be unchanged and Fig. 3.8 would be scaled by a factor of 0.001.

It can be seen from Fig. 3.12 that an example data point P and its related points $P^{'}$ and $P^{''}$ are located on a very sensitive region of the curves in both (a) and

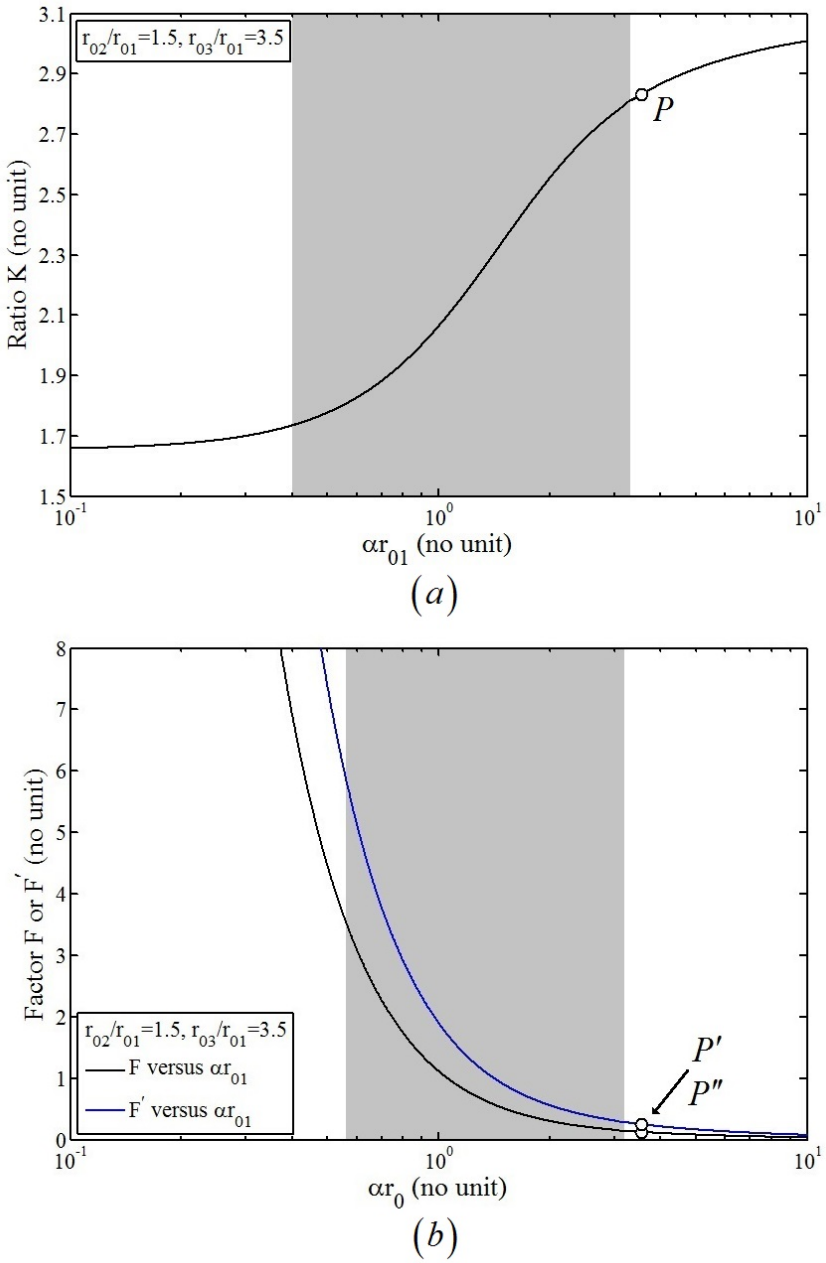

Figure 3.12: (a) K versus αr_{01} for given ratios of radii, $x = r_{02}/r_{01} = 1.5$, $y = r_{03}/r_{01} = 3.5$, in which gray area is the most useful region to obtain αr_{01}; (b) F and $F^{'}$ versus αr_{01} for given rations of radii $x = r_{02}/r_{01} = 1.5$, $y = r_{03}/r_{01} = 3.5$, the gray area is the most useful region to obtain F and $F^{'}$.

(b). A small error both in resistance and geometry measurement will lead to a significant difference in R_{SH} and ρ_c. Therefore, a smaller value of αr_{01} is required to locate the relevant data point within the gray region in Fig. 3.12 which is not so sensitive. This issue can be solved by reducing the geometry dimensions (i.e. r_{01}, r_{02} and r_{03}) or adjusting the values of x and y (smaller x and lager y are more appropriate).

An alternative method to determine ρ_c and R_{SH} using the two-contact circular test structure is using reduced analytical expressions. This method and the contribution of R_P to the total resistance R_T are discussed in Appendix B. It also involves investigation of the relationship between R_T and αr_0 and is somewhat similar to the investigation and reporting in this chapter.

3.4 Summary

A new methodology, which uses three pairs of the two-contact circular test structures, was demonstrated to derive ρ_c and R_{SH} by eliminating the outer contact resistance R_{C1} from developed equations and also eliminating the necessity for independent R_{SH} measurement. Furthermore, the scaling behavior was discussed to show that the stucture is universal for use with different metal to semiconductor ohmic contacts. Confidence in the value of ρ_c obtained by this test structure can be increased by using several test structures where only r_0 is varied and the structures are all scaled uniformly (different geometries should all give the same ρ_c and R_{SH}). The sensitivity of this method was then discussed. This issue of sensitivity to small error in measurements can be mitigated by reducing the test structure dimensions (choosing appropriate geometries) and changing the ratios (x and y) of the radii.

The new two-contact circular test structure was presented and it consists of a central dot electrode and an outer electrode. FEM was used to demonstrate the accuracy of the analytical model developed for the two-contact circular test structure. Results showed that, for appropriate geometry (chosen from several easy to fabricate test structures), this test structure can be used to accurately and

conveniently determine R_{SH} and ρ_c. This was demonstrated by using an ohmic contact with the values of R_{SH} and ρ_c being 3000 $\Omega/\square$ and 1×10^{-4} $\Omega \cdot cm^2$ respectively. Smaller values of R_{SH} and ρ_c can be determined using appropriate scaling of the test structure geometry. There was excellent agreement between the analytical and FEM results, and both of them indicated that ρ_c can be extracted accurately when $0.5 < \alpha r_0 < 10$.

Chapter 4

Two-Contact Circular Test Structure for Determining Specific Contact Resistivity of Contacts to Bulk Semiconductors

A novel method to extract the specific contact resistivity ρ_c for three-dimensional (3-D) contact structures using a two-contact circular test structure derived from investigation of the conventional three-electrode circular transmission line model (CTLM) is presented. This method is developed using finite element modeling (FEM) of ohmic contacts between a metal layer and a semiconductor substrate and the scaling behavior of this method is also determined and discussed in this chapter.

4.1 Three-Dimensional (3-D) Effects

The cross-bridge Kelvin resistor (CBKR) and the transmission line model (TLM) patterns are commonly used to determine ρ_c. Analysis using the CBKR and the TLM is based on a two-dimensional (2-D) model which assumes no voltage drop in the semiconductor layer in the vertical direction. However, [Berger, 1972] and

[Loh et al., 1987] recognized that this vertical voltage drop in a semiconductor layer has a significant effect on extracting ρ_c using both the TLM and the CBKR techniques. They pointed out that in some circumstances this could lead to a significant error in derivation of ρ_c when using the TLM. The magnitude of this error in the TLM was qualified using the parameter η [Berger, 1972]

$$\eta = \frac{\rho_c}{\rho_b \cdot t} \tag{4.1}$$

where t is the thickness of the semiconductor and ρ_b is the semiconductor resistivity.

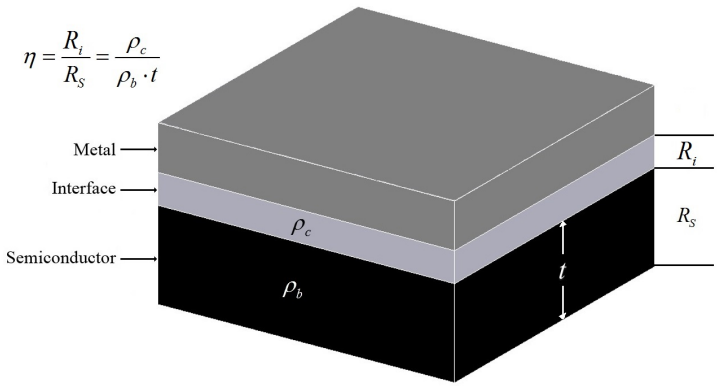

Figure 4.1: Comparison of the contact interfacial resistance, R_i, and vertical semiconductor resistance, R_S, for defining η.

From Fig. 4.1 we can find that η can be also considered as the ratio of the contact resistance R_i to the vertical semiconductor resistance R_S. In ideal circumstances, the semiconductor thickness, t, is assumed to be zero. In other words, the ohmic contact only forms in the interface layer and there is no current flow vertically in the semiconductor layer. Therefore, the value of η is infinite. This model is purely 2-D and there is no vertical voltage drop in the semiconductor layer. However, in reality, a non-zero value for thickness, t, gives a finite value for η. When $\eta = 1$ the interfacial contact resistance is the same as the semiconductor resistance. Therefore, when $\eta \leq 1$, the semiconductor resistance, R_S, which is caused

by the vertical voltage drop will influence the determination of ρ_c from the TLM. Alloyed ohmic contacts to semiconductors such as Au/Ge/Ni to GaAs and metal to silicides to Si should be analysed using 3-D models [Reeves and Harrison, 1995].

The reducing size of semiconductor devices has led to reductions in the active layer thickness [Moore, 1965]. In addition, the continued improvement in ohmic contact technology has also resulted in lowering of the minimum value of ρ_c which can be obtained. [Ohmi, 1995] has reported a value of ρ_c which is as low as $3.3 \times 10^{-9}\ \Omega \cdot cm^2$. Thus, the values of $\eta \leq 1$ will certainly arise and it is not appropriate to neglect the vertical voltage drop anymore. Furthermore, the prevalence of micro-electro-mechanical system (MEMS) semiconductor devices suggests the need for a 3-D test structure for determining ρ_c of contacts to such devices. Similarly discrete components like power diodes use ohmic contacts to substrates and characterising ohmic contacts is important to minimise power loss.

Fig. 4.2 shows the distributions of the voltage contours in the semiconductor region of a metal to semiconductor ohmic contact determined using FEM. Fig. 4.2 (a) shows a 2-D situation with an η value of 10 compared to (b) and (c) where there are 3-D effects because η has values of 0.5 and 0.01 respectively. Apparently, the crowding of voltage contours near the leading edge of the contact increases as ρ_c decreases. This increasing crowding results in a shortened current transfer length, L_T, the distance at which most of the current transfers from the semiconductor layer to the metal layer. The values of L_T for Fig. 4.2 (a), (b) and (c) are 1.11 μm, 0.25 μm and 0.035 μm respectively. These three figures clearly show that the vertical drop in voltage is becoming significant with an increasing crowding of voltage contours near the leading edge and a decreasing current transfer length.

Table 4.1 shows the ρ_c settings used in the FEM analysis and the extracted specific contact resistivity $\rho_c^{'}$ obtained using the equation [Berger, 1969]

$$V(x) = \frac{I\sqrt{R_{SH}\rho_c}}{W} \frac{\cosh\left[(L-x)/L_T\right]}{\sinh\left[L/L_T\right]} \tag{4.2}$$

where L and W are the contact length and width respectively. L_T is the transfer

length which is the distance from the leading edge of the contact at which $1/e$ of the current has entered the metal layer [Schroder, 2006]

$$L_T = \sqrt{\frac{\rho_c}{R_{SH}}} \tag{4.3}$$

Please note that x is zero when determining $\rho_c^{'}$ from equation 4.2 using FEM results.

Table 4.1: Metal to semiconductor ohmic contact parameters in FEM for contact models shown in Fig. 4.2 (a), (b) and (c).

Figure 4.2	ρ_c [1]	$\rho_c^{'}$ [2]	Error	η
(a)	1×10^{-4}	1.043×10^{-4}	4.3%	10
(b)	5×10^{-6}	7.423×10^{-6}	48.5%	0.5
(c)	1×10^{-7}	7.503×10^{-7}	650%	0.01

[1] true specific contact resistivity used in FEM $[\Omega \cdot cm^2]$.
[2] extracted specific contact resistivity from FEM $[\Omega \cdot cm^2]$.

The error (shown in Table 4.1) indicates that when $\eta \leq 1$, the 2-D analytical expressions for determining ρ_c will lead to errors and a 3-D analysis should be implemented. Correction factors are commonly used to increase the accuracy of derived ρ_c in 3-D circumstances when using the CBKR and the TLM [Holland et al., 2004], but not in the technique with the two-contact circular test structure presented in this thesis.

4.2 The Two-Contact Circular Test Structure in 3-D Circumstances

As in the the CBKR and the TLM geometries, 3-D effects influence the derivation of ρ_c. Similarly for the conventional CTLM and the two-contact circular test structure as well. To investigate the effects on the two-contact circular test structure, a purely 3-D model (where depth effects of semiconductor layer are maximised) is created in FEM.

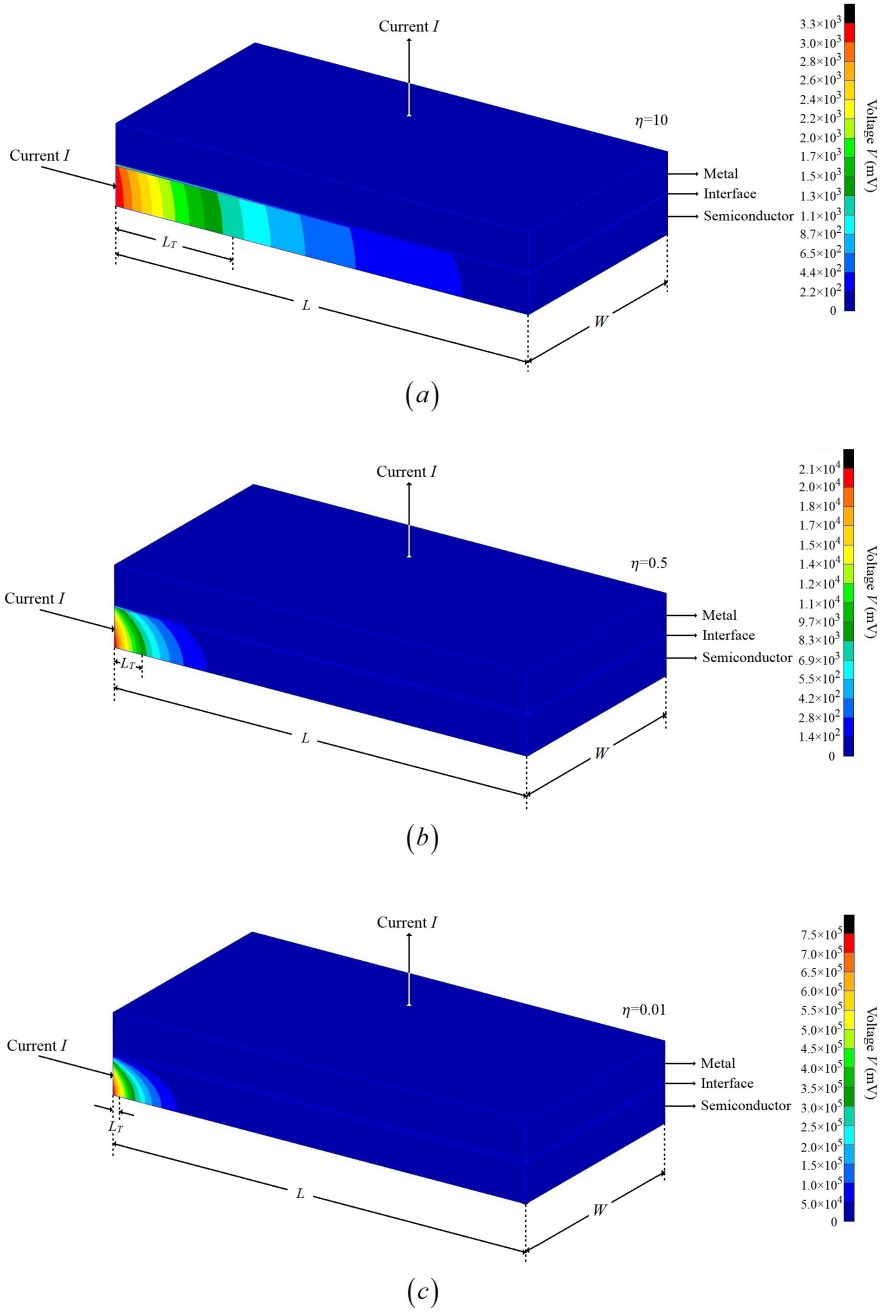

Figure 4.2: Distribution of voltage contours in the semiconductor region of a metal to semiconductor ohmic contact where $L = 4\ \mu m$, $W = 2\ \mu m$, $t = 0.35\ \mu m$, $\rho_b = 0.285\ \Omega \cdot cm$ and ρ_c values of $(a)\ 1 \times 10^{-4}\ \Omega \cdot cm^2$, $(b)\ 5 \times 10^{-6}\ \Omega \cdot cm^2$ and $(c)\ 1 \times 10^{-7}\ \Omega \cdot cm^2$. The values of L_T for (a), (b) and (c) are 1.11 μm, 0.25 μm and 0.035 μm and the corresponding η values are 10, 0.5 and 0.01 respectively.

According to equation 4.1, the test structure is assumed to be fabricated on a semiconductor substrate which has a relatively large thickness to ensure that $\eta \leq 1$. The test pattern for determining ρ_c in such a 3-D circumstance is shown in Fig. 4.3 and consists of a central dot contact and a ring contact. The radius of the central dot is r_0 and the inner and outer radii of the outer electrode are r_1 and $r_1^{'}$ respectively. Mesa isolation is not needed, as is the case for all the circular type test structures.

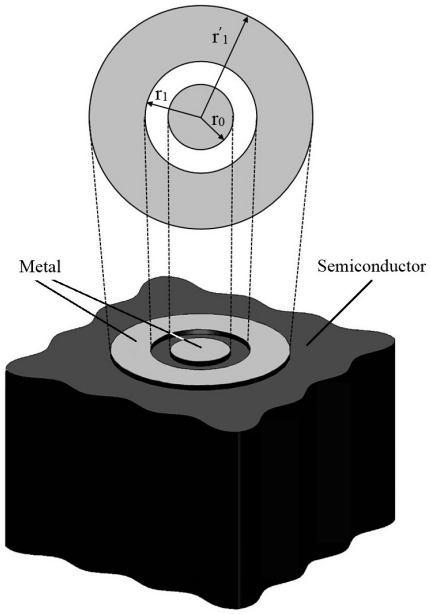

Figure 4.3: Isotropic view of a schematic of the proposed 3-D two-contact circular test structure.

In this chapter, r_0, r_1, $r_1^{'}$, ρ_b and ρ_c are all the parameters which are required to determine the total resistance R_T that is between the two electrodes. It can be written in the following form which is useful in the study of the scaling behavior of this method (discussed later).

$$R_T = R_T \left\{ r_0, r_1, r'_1, \rho_b, \rho_c \right\} \tag{4.4}$$

By measuring R_T, the value of ρ_c can be calculated with the resistivity of the semiconductor layer ρ_b and the geometry sizes known.

4.3 Modeling of The Two-Contact Circular Test Structure in 3-D Circumstances

The analytical solutions to the current-voltage (I-V) relationship of the proposed test structure were deemed to be too difficult to obtain. Therefore, a graphical method to determine ρ_c which is developed using FEM of ohmic contacts between a metal layer and a semiconductor substrate is presented. FEM can be used to accurately model the electrical behavior of ohmic contacts between a metal and a semiconductor. Creating a model requires the following information: (i) test structure geometry, (ii) conductivity of each layer in the structure and (iii) specific contact resistivity ρ_c of each interface in the structure [Holland et al., 2009].

Fig. 4.4 shows a section of the FEM model used to develop solutions for the 3-D ohmic contact test structure. A 45° sector is modeled to reduce the time taken for analysis to run. The current is injected at the center electrode and the equipotential of the outer electrode is set to zero. The voltage contours in this figure shows that when the thickness of the semiconductor layer, t, is beyond a certain value $t^{'}$, little current goes through the bottom of the semiconductor substrate. What is meant by this is that when metal contacts to the substrate directly, the thickness of the semiconductor layer, t, can be considered as infinite beyond this thickness, $t^{'}$ (relatively small compare to typical substrate thickness). From the crowding of the voltage contours which is underneath the central dot metal contact, it can be found that there is a significant vertical voltage drop in the semiconductor substrate ($\eta \ll 1$). Fig. 4.5 illuminates the current densities of the same model which is shown in Fig. 4.4.

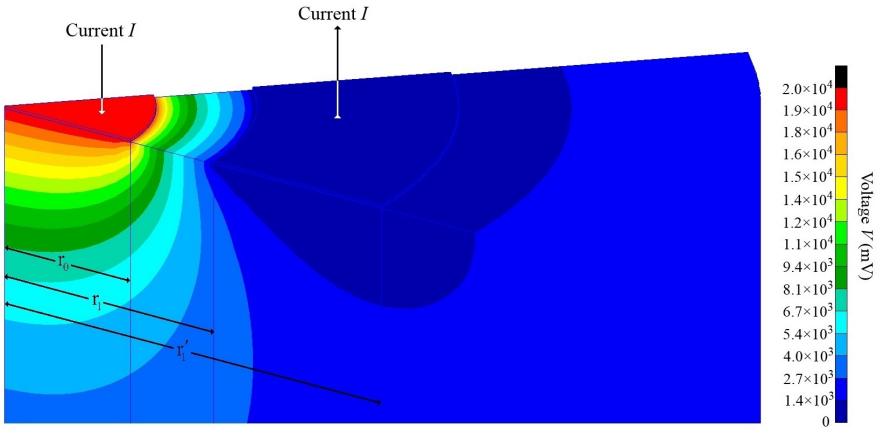

Figure 4.4: Equipotentials (in millivolts) in the semiconductor layer in a 3-D situation for the FEM example where $r_0 = 15\ \mu m$, $r_1 = 25\ \mu m$ and $r_1^{'} = 45\ \mu m$. The bulk semiconductor resistivity, ρ_b, and specific contact resistivity, ρ_c, are set as $0.08\ \Omega \cdot cm$ and $1 \times 10^{-4}\ \Omega \cdot cm^2$ respectively (a 45° sector of the test structure is presented and Fig. 4.3 is a schematic of the full test structure).

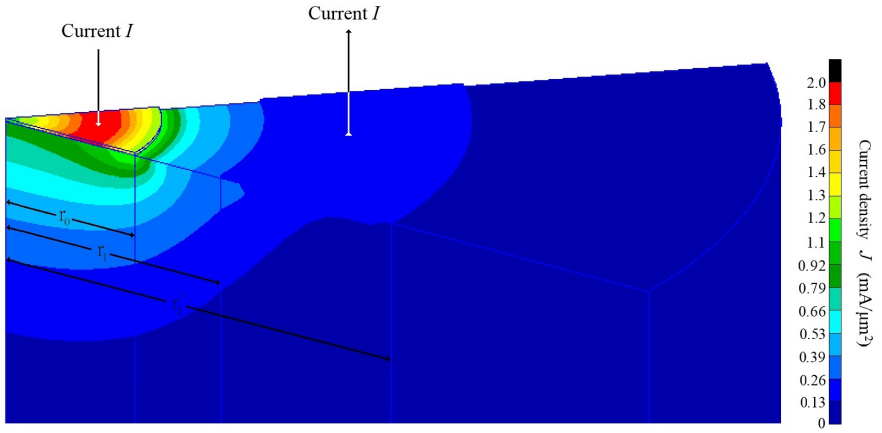

Figure 4.5: Current densities (in milliamperes per square micrometers) in the semiconductor layer in a 3-D situation for the FEM example where $r_0 = 15\ \mu m$, $r_1 = 25\ \mu m$ and $r_1^{'} = 45\ \mu m$. The bulk semiconductor resistivity, ρ_b, and specific contact resistivity, ρ_c, are set as $0.08\ \Omega \cdot cm$ and $1 \times 10^{-4}\ \Omega \cdot cm^2$ respectively (a 45° sector of the test structure is presented and Fig. 4.3 is a schematic of the full test structure).

4.4 A Novel Method for Determining Specific Contact Resistivity in 3-D Circumstances Using The Two-Contact Circular Test Structure

In this section, a number of 3-D models are analyzed using FEM with ρ_b and ρ_c varying from 0.001 $\Omega \cdot cm$ to 0.01 $\Omega \cdot cm$ and 1×10^{-8} $\Omega \cdot cm^2$ to 1×10^{-3} $\Omega \cdot cm^2$ respectively. The geometry size is fixed ($r_0 = 3$ μm, $r_1 = 5$ μm and $r_1^{'} = 9$ μm, because this ratio, 3:5:9, can keep the contribution of the resistance R_P which is due to the semiconductor ring and has no information on ρ_c to the total resistance R_T small) and the thickness of the semiconductor layer is set to be large enough to make sure the model is 3-D and little current goes through the bottom of the substrate. Beyond the thickness $t^{'}$, the value of R_T will not change for any ρ_b, ρ_c combination for increasing t. Fig. 4.6 can be generated by plotting R_T as a function of ρ_c with variable ρ_b.

From Fig. 4.6, the right curve (or interpolate between curves) can be selected with known semiconductor resistivity, ρ_b, and the value of, ρ_c, can be found using the experimentally determined total resistance R_T.

The scaling behavior of this method is shown in equation 4.5. This is similar to the scaling equation reported in [Loh et al., 1985] for the CBKR

$$R_T \left\{ mr_0, mr_1, mr_1^{'}, mn\rho_b, m^2 n\rho_c, mt^{'} \right\} = nR_T \left\{ r_0, r_1, r_1^{'}, \rho_b, \rho_c, t^{'} \right\} \tag{4.5}$$

Using equation 4.5, the plots in Fig. 4.6 will be the same with ρ_c, R_T and ρ_b scaled by factors of $m^2 n$, n and mn respectively. Thus, the structure is universal and applicable for ohmic contacts where the resistive effects of the semiconductor and the contact can be described by ρ_b and the geometry of the electrodes. For example, when $m = 1$ and $n = 10$, Fig. 4.7 which has the same shape of plots in Fig. 4.6 but for a new set of ρ_b.

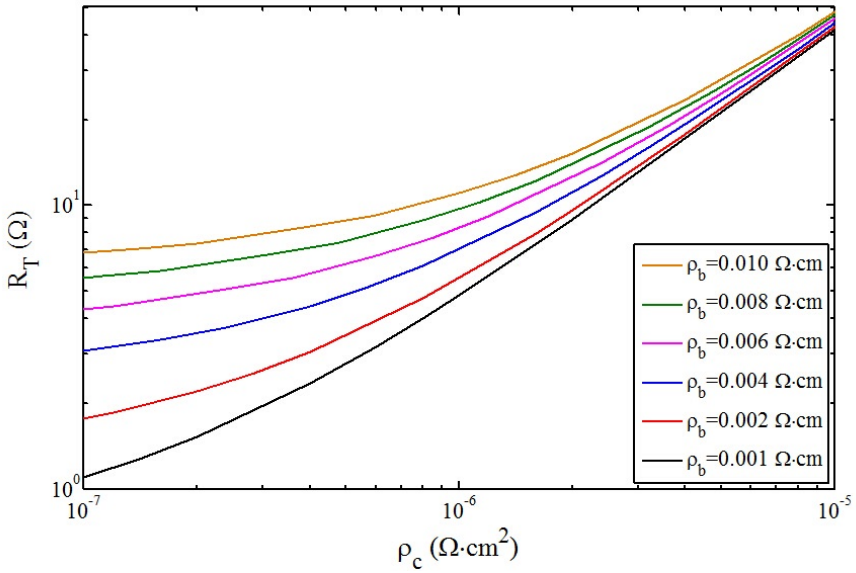

Figure 4.6: FEM analysis results showing R_T plotted as a function of ρ_c with ρ_b varying from 0.001 $\Omega \cdot cm$ to 0.01 $\Omega \cdot cm$. Geometry is fixed: $r_0 = 3\ \mu m$, $r_1 = 5\ \mu m$ and $r_1^{'} = 9\ \mu m$.

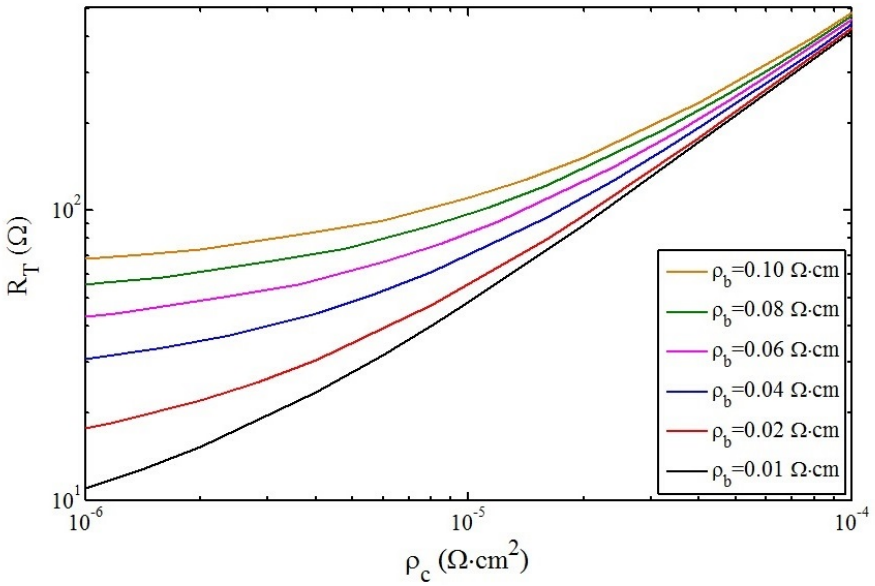

Figure 4.7: FEM analysis results showing R_T plotted as a function of ρ_c with ρ_b varying from 0.01 $\Omega \cdot cm$ to 0.1 $\Omega \cdot cm$. Geometry is fixed: $r_0 = 3\ \mu m$, $r_1 = 5\ \mu m$ and $r_1^{'} = 9\ \mu m$.

4.5 Summary

A novel method for determining ρ_c between a metal and a semiconductor ohmic contact in 3-D circumstances (e.g. contact to bulk semiconductor) using a two-contact circular test structure was presented. The method was developed using a FEM program. The results showed that with known semiconductor substrate resistivity, ρ_b, fixed geometry, and using the scaling equation 4.5, as required, ρ_c can be determined conveniently from plots of R_T versus ρ_c as reported in this chapter.

Chapter 5

Fabrication of The Two-Contact Circular Ohmic Contact Test Structure

The design and fabrication of the two-contact circular test structure for several metal to semiconductor ohmic contacts are described in detail in this chapter. This test structure is used to determine the specific contact resistivity ρ_c between a metal and semiconductor ohmic contact in both two-dimensional (2-D) and three-dimensional (3-D) circumstances using the methods described in Chapter 3 and 4. The fabrication processes include wafer cleaning, photolithography, metal evaporation, wet etching, lift off and annealing. Electrical testing results and analysis of the results obtained using the fabricated structures will be discussed in Chapter 6.

5.1 Mask Design

5.1.1 Mask for The Two-Contact Circular Test Structure for Contacts to 2-D Semiconductor Layers

The electronic design automation (EDA) tool, Cadence, was used as a photolithographic mask design program. The mask was designed for both the wet etching and the lift off techniques with r_{01} varying from 3 μm to 15 μm. As presented in Chapter 3, r_{02} and r_{03} are always 1.5 and 3.5 times greater than r_{01} because these ratios can keep the contact resistance to be a significant part of the total resistance in the electrical testing, thus, increasing the accuracy in extracting ρ_c. In addition, these ratios can reduce the effect of the measurement error on extracting ρ_c when using the evaluation technique presented in Chapter 3 (see Fig. 3.12). The design was then transferred to a mask with chromium patterns.

Fig. 5.1 and Fig. 5.2 show the mask designs for both the wet etching and the lift off techniques. The black regions are the chromium on the mask which can block the UV light used in photolithography and the white regions are the glass which are transparent. The complete test structure consists of three different two-contact circular test patterns. The radii of the central dots for the complete test structure (see Fig. 3.9) from left to right are r_{01}, r_{02} and r_{03} respectively. The numbers in the two figures represent the radii (in micrometers) of the central dot r_{01}. The relatively small features are in the centre of the mask because this area has a better resolution during the fabrication. Both of the mask designs can be used to fabricate identical two-contact circular test structures but using different techniques.

Fig. 5.1 shows the mask design for contacts to 2-D semiconductor layers using the wet etching technique. Similar to the photographic developer used for photoresist, this technique uses liquid-phase etchants for different materials. The samples can be immersed in a bath of etchant, which must be agitated to achieve good process control. For example, a hydrofluoric acid (HF) solution is commonly used to etch Ti. Wet etchants are usually isotropic, which leads to large bias when

etching thick films and multi-layer materials. However, material removal rate for wet etching is very fast and can be easily changed by varying temperature or the concentration of the etchants. Fig. 5.3 (a) shows the simplified wet etching process using positive photoresist. The fabrication procedures are metalization, photoresist spinning, exposure, development, metal etching and photoresist removal in sequence.

Fig. 5.2 presents the mask design for the lift off technique. Compared to the wet etching technique, the lift off technique is more attractive. Fig. 5.3 (b) shows the basic lift off process. An inverse pattern (photoresist) is first created on the surface of the substrate. The target material is deposited over the whole area of the sample, staying on both the surface of the substrate and the top of the inverse pattern (photoresist). When the inverse pattern is washed away (photoresist in acetone), the material on the top is lifted off and removed together with the inverse pattern below. The target material remains in the regions where it had direct contact with the surface of the substrate. Lift off is more appropriate for multi-layer target materials and thick films since there is no isotropic etching problem and when compared to the poor controllability of the wet etching technique, it is more suitable for small patterns. However, the biggest issue is that unwanted part of the target materials may remain on the substrate after lift off. In addition, the lifted off target materials may become reattached to the surface of the substrate and it is very difficult to remove these undesirable materials after drying the samples.

5.1.2 Mask for The Two-Contact Circular Test Structure for Contacts to Bulk Semiconductors

Similar to Fig. 5.1 and Fig. 5.2, Fig. 5.4 shows the design for contacts to bulk semiconductors using the lift off technique. As presented in Chapter 4, the test structure designs have r_0 from 3 μm to 30 μm and the ratio of r_0, r_1 and $r_1^{'}$ are kept to be 3:5:9 because this ratio can keep the contact resistance to be a significant part of the total resistance in the electrical testing and therefore increase the

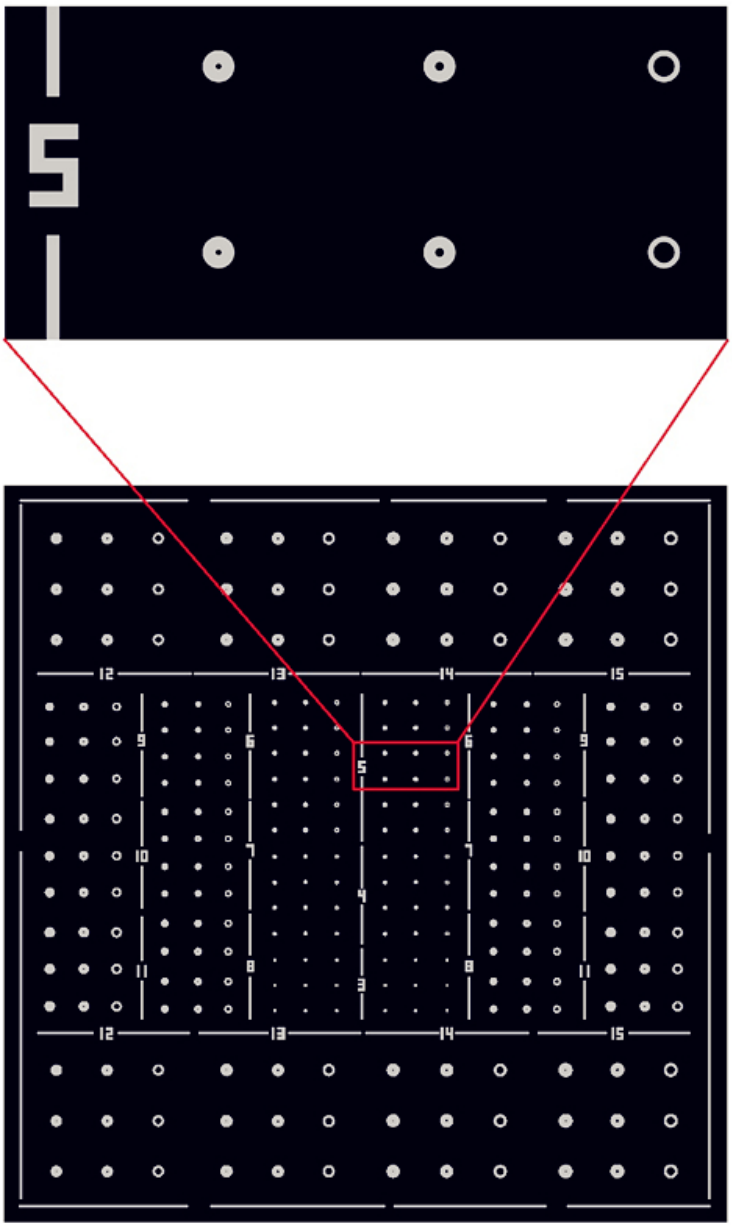

Figure 5.1: Mask design for the two-contact test structure for contacts to 2-D semiconductor layers for the wet etching technique. The black regions are the chromium on the mask and the white regions are the glass which are transparent. The numbers represent the radii of the central dot r_{01} (e.g. in the top figure "5" refers to the left most dot contact being 5 μm radius).

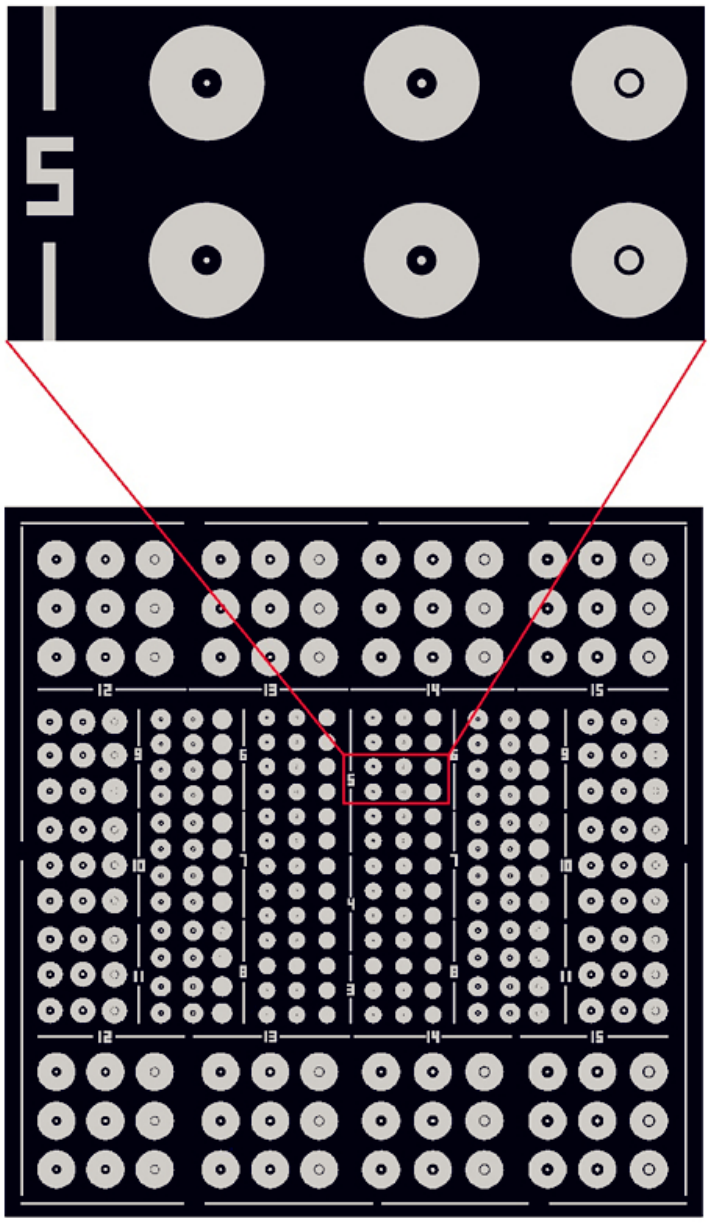

Figure 5.2: Mask design for the two-contact circular test structure for contacts to 2-D semiconductor layers for the lift off technique. The black regions are the chromium on the mask and the white regions are the glass which are transparent. The numbers represent the radii of the central dot r_{01} (e.g. in the top figure "5" refers to the left most dot contact being 5 μm radius).

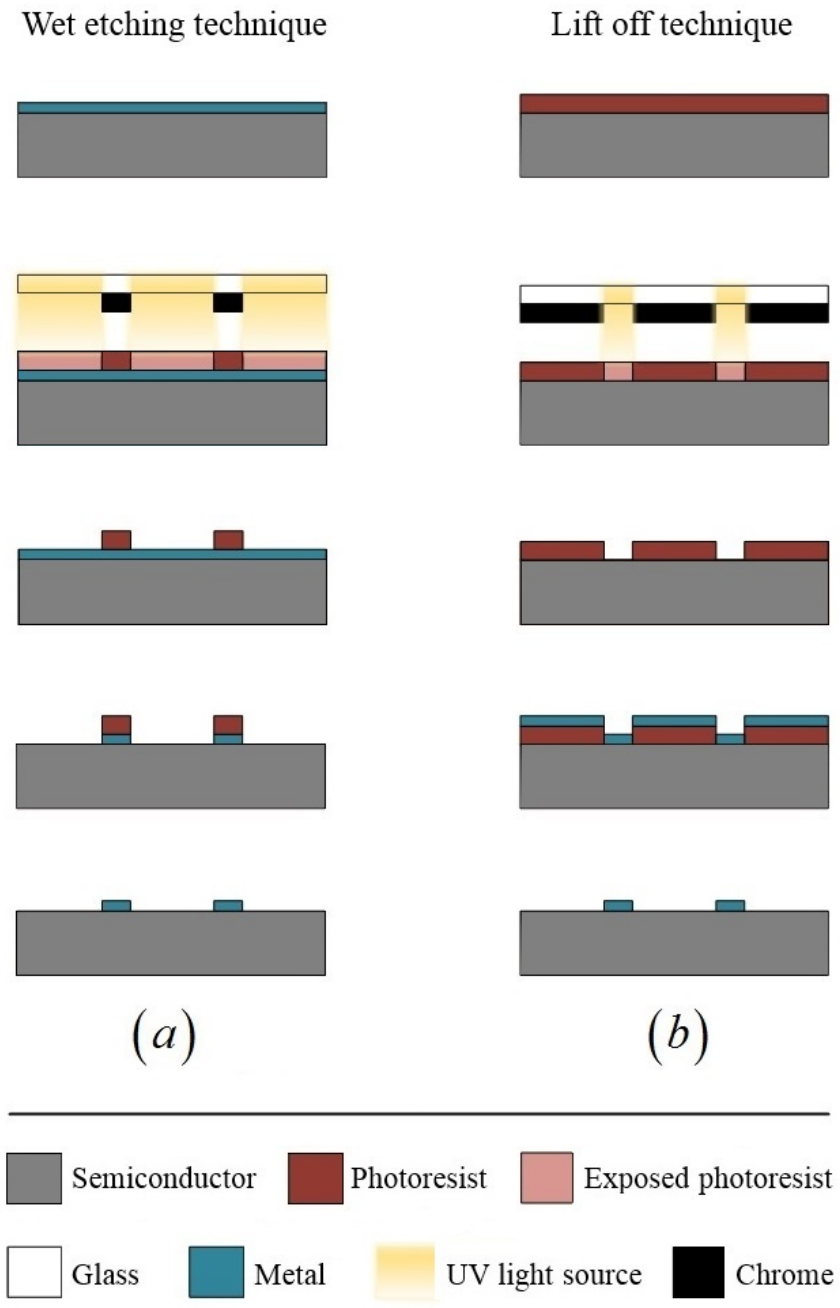

Figure 5.3: Simplified illustrations of (a) the wet etching technique using positive photoresist, (b) the lift off technique using positive photoresist for the same patterns.

accuracy when extracting ρ_c using the two-contact circular test structure. The radii ratios are also appropriate for practical fabrication of suitably small test structures.

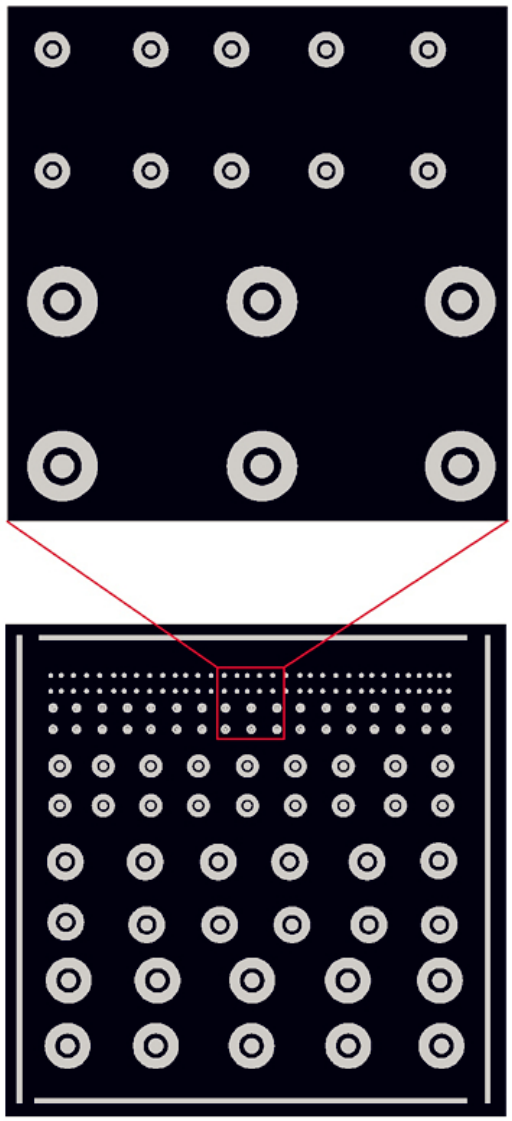

Figure 5.4: Mask design for the two-contact test structure for contacts to bulk semiconductors for the lift off technique. The black regions are the chromium on the mask and the white regions are the glass which are transparent. The radius of the central dot r_0 varying from 3 μm to 30 μm.

5.2 Metal to 2-D Semiconductor Layers Ohmic Contacts

A number of metals were evaporated on the epitaxial layer of n-type 3C-SiC which was grown on three inch wafers of p-type Si <100> by low pressure chemical vapor deposition (LPCVD) in a hot wall reactor [Wang et al., 2009]. The 3C-SiC epitaxial layer has different doping concentrations, therefore different resistivities. The film of 3C-SiC was 1.1 μm thick and the p-type Si had a thickness of approximate 300 μm. The two-contact circular test structures were then fabricated using the masks shown in Fig. 5.1 and Fig. 5.2 using either the wet etching or the lift off technique.

5.2.1 Formation of Ni to 3C-SiC Ohmic Contacts

The n-type 3C-SiC epitaxial layer with 1.1 μm thick was grown on a three inch Si wafer. The wafer was diced into square pieces with dimensions of 1×1 cm^2. It is very important to have an ultra clean SiC film without any native oxides or contamination before evaporating Ni. The cleaning process is shown below;

1. Immerse the sample in AZ100 solvent for 30 minutes at 85°C.
2. Rinse the sample in deionised water for 2 minutes.
3. Immerse the sample in 3% HF for 30 seconds.
4. Rinse the sample in a sequence of acetone, isopropal alcohol (IPA) and deionised (DI) water.
5. Dry the sample with high purity pressured nitrogen gas.

After cleaning, the sample was loaded into an evaporation chamber and a Ni layer of 200 nm thickness was deposited on the 3C-SiC layer by electron beam evaporation. The evaporation settings are shown in Table 5.1.

The procedure of the patterning using the wet etching technique is as follows:

1. Rinse the sample in a sequence of acetone, IPA and DI water.
2. Bake the sample in an oven for 10 minutes at 110°C for dehydration.
3. Spin on hexamethyldisilazane (HMDS) at 4000 r.m.p. for 10 seconds.
4. Spin on AZ4562 photoresist at 4000 r.m.p. for 15 seconds.
5. Soft bake on the hot plate at 95°C for 90 seconds.
6. Expose the sample using MJB3 mask aligner for 8 seconds.
7. Develop the sample using AZ400K:DI water (1:4) for 10 seconds.
8. Hard bake in an oven at 110°C for 1 minute.
9. Cool the sample down for 5 minutes and etch the sample in Ni etchant (100 ml 70% hydrochloric acid, 50 g $(NH_4)_2Ce(NO_3)_6$, 150 ml DI water) at room temperature for 30 seconds.
10. Rinse the sample in DI water and dry it using high purity pressured nitrogen gas.

Table 5.1: Electron beam evaporator conditions for Ni on 3C-SiC.

Material	Nickel
Thickness	200 nm
Pressure	1.4×10^{-7} $mbar$
Rate	0.20 $nm/sec.$

The sample was then examined under an optical microscope and the patterned photoresist was removed using acetone followed by IPA and DI water. Nitrogen gas was used to dry the sample. An initial current-voltage (I-V) testing was taken and a linear I-V curve shows that an ohmic contact has been formed between as-deposit Ni and 3C-SiC film. Fig. 5.5 shows an optical micrograph of sections of the patterns. Note that for the 2-D test structure the test structure pattern for determining ρ_c and R_{SH} come as a series of three dot electrodes. In Fig. 5.5 there are eight such patterns, all the same.

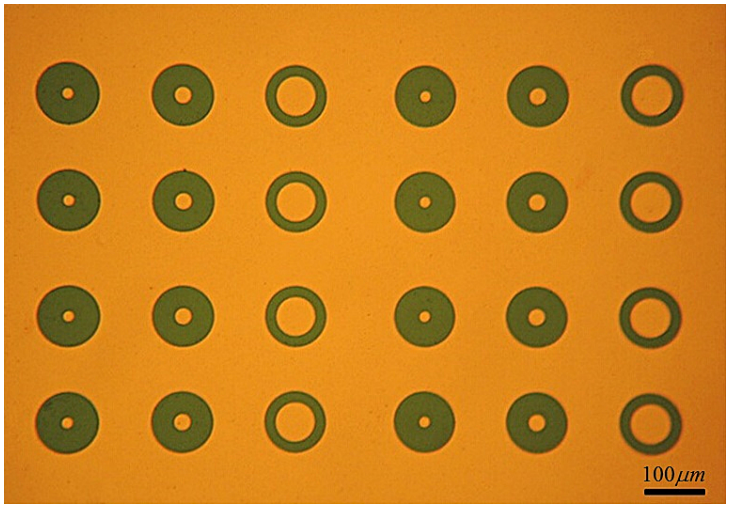

Figure 5.5: Optical micrograph of the two-contact circular test structures fabricated on epitaxial 3C-SiC using wet etching technique, the metal layer is Ni and the radii of the central electrodes shown are 10 μm, 15 μm and 35 μm respectively.

5.2.2 Formation of Ti to 3C-SiC Ohmic Contacts

The sample described in this section has a much more lightly doped n-type 3C-SiC epitaxial layer compare to the sample described in Section 5.2.1. As for all good contacts, the sample cleaning procedures must be done before the test structure fabrication. The cleaning process is the same as that in Section 5.2.1. After cleaning, the sample was loaded into an evaporation chamber and a Ti layer of 400 nm thickness was deposited on the 3C-SiC layer by electron beam evaporation. The evaporation settings are shown in Table 5.2.

Table 5.2: Electron beam evaporator conditions for Ti on 3C-SiC.

Material	Titanium
Thickness	400 nm
Pressure	1.7×10^{-7} $mbar$
Rate	0.15 $nm/sec.$

The procedure of the patterning using the wet etching technique is the same as that for Ni to 3C-SiC ohmic contacts in Section 5.2.1 but using a Ti etchant (1%

HF) instead of the Ni etchant. The sample was etched at room temperature for 85 seconds.

Finally, the sample was examined under an optical microscope and the patterned photoresist was removed using acetone followed by IPA and DI water and high purity pressured nitrogen gas was used to dry the sample.

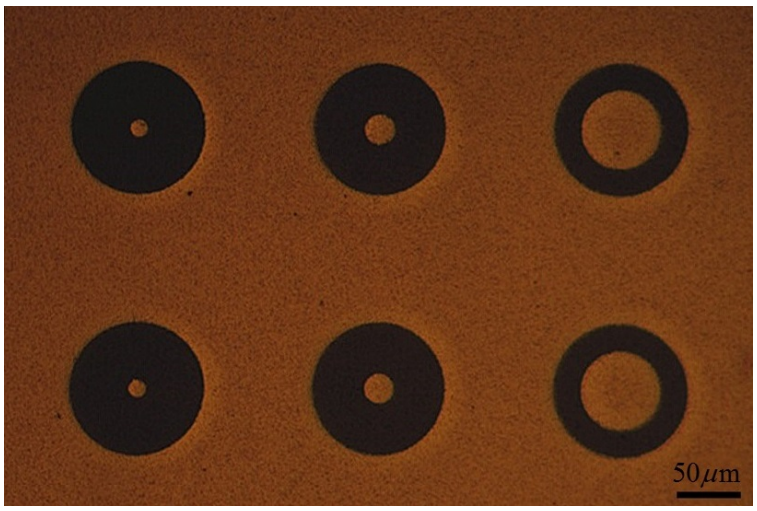

Figure 5.6: Optical micrograph of the two-contact circular test structures fabricated on epitaxial 3C-SiC using the wet etching technique, the metal layer is Ti and the radii of the central electrodes shown are 9 μm, 13.5 μm and 31.5 μm respectively.

Fig. 5.6 shows an optical micrograph of one of many test structures formed on the SiC/Si substrate. The smallest features formed were the circular electrodes of approximately 2.5 μm radius. The sample was then taken for an initial I-V testing. A linear I-V curve indicates that an ohmic contact has been formed between as-deposit Ti and 3C-SiC film. But linear I-V only occurs for highly doped semiconductors if no heat treatment is applied.

5.2.3 Formation of Au/Ni/Ti to Ion Implanted 3C-SiC Ohmic Contacts

The n-type 3C-SiC epitaxial layer was 1.1 μm thick with a carrier concentration of 1×10^{20} cm^{-3} doped with N during epitaxial layer formation. The layer of 3C-SiC was implanted with either C or P ions at -196°C using an energy of 5 keV and samples were prepared with doses in the range $10^{13} - 10^{15}$ $ions/cm^2$. These ion species were selected on the basis of calculations using the TRIM (transport and range of ions in matter) software which predicted distinctly different profiles for different energy depositions for P and C ions in SiC. Note that the 3C-SiC epitaxial layer was made n-type during epi growth. The ion implantation was not for doping. It was to see if the damage at low energy ion implant improves or worsen ρ_c.

Figs. 5.7 and 5.8 show TRIM simulations of the concentration of P and C ions versus depth and the distribution of energy deposition resulting from an implantation at 5 keV into SiC. The TRIM code has simulated the cumulative effects of individual ions in their collisions through the substrate. These effects include resulting implanted species concentration profile any damage distribution which is related to energy distribution. In Fig. 5.7, the implanted P ions have exhibited a higher level of peak concentration than for the C ions. Also, the peak in P concentration in Fig. 5.7 was evident at a shallower depth ($5 - 10$ nm) than the maximum level of C which was located at $10 - 15$ nm below the surface. Fig. 5.8 shows that the distribution of energy deposition was similar in profile to the ion concentration versus depth in Fig. 5.7. However, the plots in Fig. 5.8 have predicted a slightly shallower depth for the maximum peak than the equivalent peak evident in Fig. 5.7. In Fig. 5.8, the peak in energy deposition was located at 5 μm for P ions and $5 - 10$ μm for C. The TRIM simulations have also predicted a linear increase in both the concentration of implanted P or C ions and the energy deposition with dose. Figs. 5.7 and 5.8 were plotted using a dose of 1×10^{15} $ions/cm^2$. Note that the samples were not heat treated before metal deposition.

The samples were then cleaned as before. The two-contact circular test structures were patterned using the lift off technique as follows:

1. Bake the samples in the oven for 10 minutes at 110°C for dehydration.
2. Spin on AZ1512 photoresist at 3000 r.m.p. for 20 seconds.
3. Soft bake on the hot plate at 95°C for 90 seconds.
4. Expose the samples using MJB3 mask aligner for 8 seconds.
5. Immerse the samples into chlorobenzene for 1 minute.
6. Rinse the samples in DI water for 3 minutes to remove the chlorobenzene.
7. Develop the samples using AZ400K:DI water (1:4) for 25 seconds.
8. Rinse the samples in DI water and dry it using high purity pressured nitrogen gas.

After that, the samples were examined under an optical microscope and loaded into an evaporation chamber and the Ti, Ni and Au layers with thicknesses of 50 μm, 50 μm and 50 μm respectively were deposited on the SiC layer in sequence by electron beam evaporation. The evaporation settings are shown in Table 5.3.

Table 5.3: Electron beam evaporator conditions for Au/Ni/Ti on 3C-SiC.

Material	Gold	Nickel	Titanium
Thickness	50 nm	50 nm	50 nm
Pressure	4.0×10^{-7} $mbar$	2.6×10^{-7} $mbar$	3.9×10^{-7} $mbar$
Rate	0.20 $nm/sec.$	0.10 $nm/sec.$	0.10 $nm/sec.$

Lift off was completed by immersing the samples into acetone in an ultrasonic bath for approximately one minute. The samples were then rinsed with acetone, IPA and DI water followed by blowing dry with high purity pressured nitrogen gas. After examining the patterns under an optical microscope, all the samples (with ion implanted with doses in the range $10^{13} - 10^{15}$ $ions/cm^2$) were taken for

I-V testing. The linear I-V curves show that ohmic contact exists on all the samples (as-deposited Au/Ni/Ti on ion implanted 3C-SiC). Fig. 5.9 shows an optical micrograph of examples of the two-contact circular test structures fabricated on ion implanted 3C-SiC film.

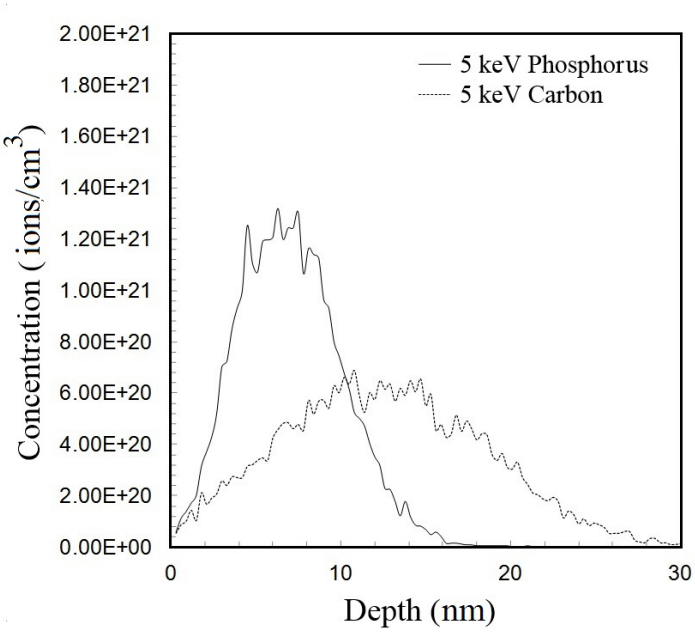

Figure 5.7: TRIM simulation of P and C ion concentrations after implantation into SiC at 5 keV at a dose of 1×10^{15} $ions/cm^2$.

5.3 Metal to Bulk Semiconductors Ohmic Contacts

Ni was evaporated on a p-type Ge substrate with a thickness of 220 μm and Ti was evaporated on a n-type 4H-SiC substrate with a thickness of 330 μm. The two-contact circular test structures were then fabricated with the mask shown in Fig. 5.4 using the lift off technique.

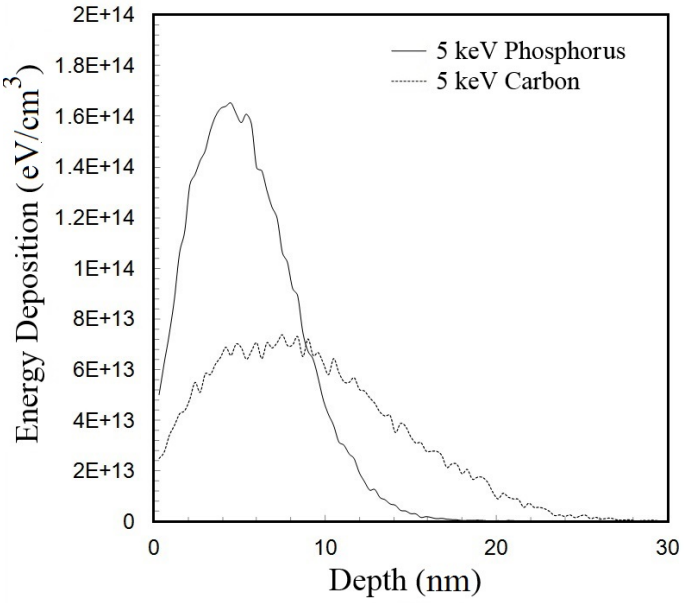

Figure 5.8: TRIM simulation of P and C distribution of energy deposition after implantation into SiC at 5 keV at a dose of 1×10^{15} $ions/cm^2$.

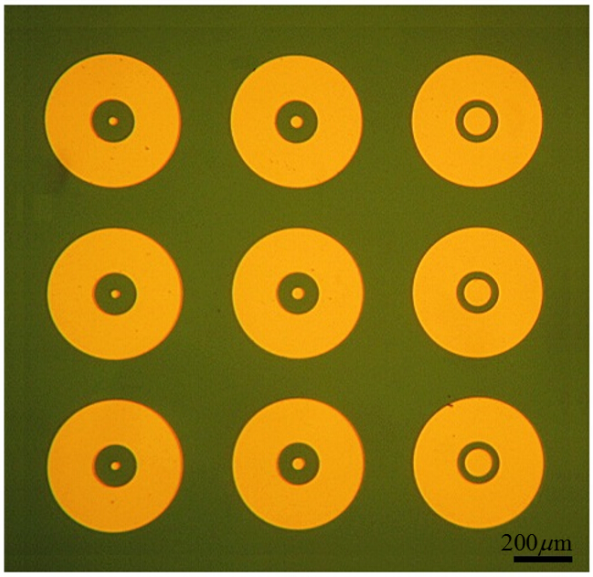

Figure 5.9: Optical micrograph of the two-contact circular test structures fabricated on epitaxial 3C-SiC using the lift off technique, the metal layer is Au/Ni/Ti and the radii of the central electrodes shown are 14 μm, 21 μm and 49 μm respectively.

5.3.1 Formation of Ni to Bulk Ge Ohmic Contacts

The p-type three inch Ge wafer was diced into squares with dimensions of $1 \times 1\ cm^2$. The resistivity for the Ge substrate was determined before the wafer was diced using the four point probe technique [Valdes, 1952] and it was determined to be $0.035\ \Omega \cdot cm$. The contamination and native oxides on the Ge substrate must be removed to obtain the best ohmic contact. The cleaning procedures are the same as those presented in Section 5.2.1 and the two-contact circular test structures were patterned on Ge substrate. The patterning process using the lift off technique has been presented in Section 5.2.3.

The samples were examined under an optical microscope and loaded into an evaporation chamber and a Ni layer with a thickness of 200 nm was deposited on the Ge substrate by electron beam evaporation. The evaporation settings are the same as those shown in Table 5.1.

Lift off was completed by immersing the sample into acetone in an ultrasonic bath for approximately one minute. The sample was then rinsed with acetone, IPA and DI water followed by blowing dry with high purity pressured nitrogen gas. After examining the patterns under the microscope, the sample was taken for an initial I-V testing. The linear I-V curve indicates that ohmic contact exists between as-deposited Ni and Ge substrate.

Fig. 5.10 shows an optical micrograph of examples of the two-contact circular test structures fabricated on Ge substrate. The electrodes formed were replicas of the mask pattern. The boundaries of the electrodes were well defined and circular, hence suitable for use. These is unlikely to be any error due to the electrodes not becoming circular. However it is important to measure the actual radii to make sure that the test structure technique is applied accurately.

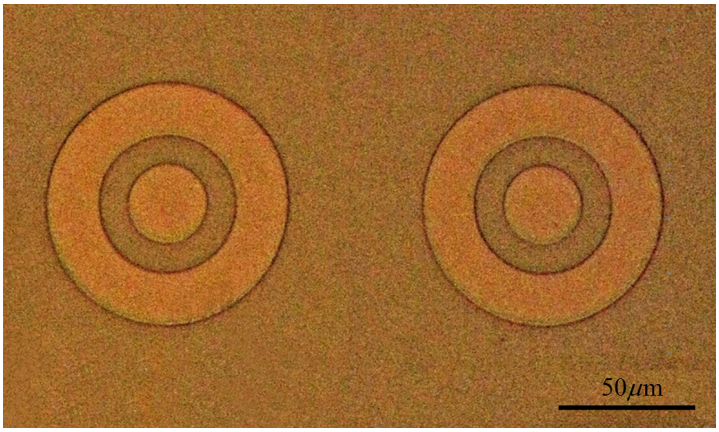

Figure 5.10: Optical micrograph of the two-contact circular test structures fabricated on bulk Ge using the lift off technique, the metal layer is Ni and r_0, r_1 and $r_1^{'}$ are 15 μm, 25 μm and 45 μm respectively.

5.3.2 Formation of Ti to Bulk 4H-SiC Ohmic Contacts

The n-type two inch 4H-SiC wafer was diced into squares with dimensions of $1 \times 1\ cm^2$. The resistivity for the 4H-SiC substrate was 0.01 $\Omega \cdot cm$. The cleaning procedures and the patterning process using the lift off technique are the same as those presented in Section 5.2.1 and Section 5.2.3.

After the patterning, the sample was examined under an optical microscope and loaded into an evaporation chamber and a Ti layer with a thickness of 150 nm was deposited on the 4H-SiC substrate by electron beam evaporation. The evaporation settings are shown in Table 5.4.

Table 5.4: Electron beam evaporator conditions for Ti on 4H-SiC.

Material	Titanium
Thickness	150 nm
Pressure	2.2×10^{-7} $mbar$
Rate	0.10 $nm/sec.$

Lift off was completed by immersing the sample into acetone in an ultrasonic bath for approximately one minute. The sample was then rinsed with acetone,

IPA and DI water followed by blowing dry with high purity pressured nitrogen gas.

Fig. 5.11 shows an optical micrograph of one example of the two-contact circular test structures fabricated on 4H-SiC substrate. After examining the patterns under a microscope, the sample was taken for an initial I-V testing. The non-linear I-V curve indicates that Schottky contacts exist between as-deposited Ti and the 4H-SiC substrate. Therefore, a heat treatment must be done to change the contacts to be ohmic and this heat treatment also helps to repair the damaged lattice near the interface between Ti and SiC substrate.

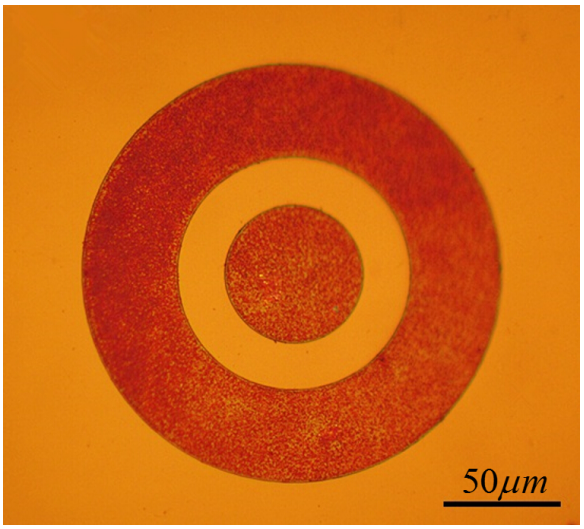

Figure 5.11: Optical micrograph of the two-contact circular test structures fabricated on bulk 4H-SiC substrate using the lift off technique, the metal layer is Ti and r_0, r_1 and $r_1^{'}$ are 30 μm, 50 μm and 90 μm respectively.

It has been reported that the heat treatment temperature must be at least 950°C to make the Ti to SiC contacts to be ohmic and a temperature of 1100°C is sufficient to ensure most contacts become ohmic and have a low contact resistance [Chang et al., 2005]. After annealing the sample at 1100°C in argon gas for 30 minutes, the I-V characteristic became linear which indicates that ohmic contacts have been formed between Ti and 4H-SiC.

5.4 Summary

Two-contact circular test structures were fabricated on n-type epitaxial 3C-SiC, p-type Ge substrate and n-type bulk 4H-SiC using either the wet etching or the lift off technique. The contact metals used in the experiments are Ni, Ti and Au/Ni/Ti. The fabrication procedures were described in detail and the masks for the photolithography were also presented. The linear I-V characteristics of the contacts on these samples showed that ohmic contacts have been formed between metal and semiconductor layers.

The samples were further tested for determining ρ_c and sheet resistance R_{SH} (reported in the next chapter) using the techniques presented in Chapter 3 and 4 and the electrical testing results verified the theories and FEM results discussed in these earlier chapters.

Chapter 6

Electrical Testing Results and Analysis

This chapter reports on the electrical testing that was performed on test structure samples with different metals to different semiconductors. These semiconductors include epitaxial 3C-SiC and 4H-SiC substrates. These were fabricated as reported in Chapter 5 using the methods presented in Chapter 3 and 4 to determine ρ_c. In addition, some samples with Ni to Ge substrate ohmic contacts were tested as well to verify the ρ_c evaluation technique described in Chapter 4.

The semiconductor SiC has shown exceptional properties in devices used in harsh environments such as at elevated temperatures and high power levels. Recent developments in the high quality epitaxial layers of 3C-, 4H- and 6H-SiC have enabled the large-scale fabrication of these devices. An important requirement in the realization of high power devices on SiC has been the ability to form ohmic contacts with characteristics of low contact resistance and high thermal stability. The two-contact circular test structure [Pan et al., 2013] is convenient to use for investigating SiC in both two-dimensional (2-D) and three-dimensional (3-D) situations.

6.1 Equipment Setup

The equipment used for measurements consists of three micro-manipulators with probe tip radius of 0.6 μm, a Keithley 2410 current source which can determine the voltage at the same time and an optical microscope with a maximum magnification of $\times$250. As shown in Fig. 6.1, the test pattern is inspected through the optical microscope. Probe 1 is on the right side, and is landed on the central electrode and connected to one polarity of the Keithley 2410. Probes 2 and 3 are on the left side, and are landed on the outer electrode to keep it at an equipotential and connected to the other polarity of the Keithley 2410. 1 μA is supplied by the Keithley 2410 and simultaneously, the voltage difference between the two metal electrodes is shown. Hence, the total resistance between the electrodes can be determined. The current-voltage (I-V) characteristic between the electrodes can be observed on a computer by connecting the Keithley 2410 to it and using the LabTracer software supplied by Keithley Instruments Inc.

6.2 Specific Contact Resistivity Evaluation Using The Two-Contact Circular Test Structure for Contacts to 2-D Semiconductor Layers

6.2.1 Ni to 3C-SiC Ohmic Contacts

The schematic of the cross-section of a fabricated two-contact circular test structure for determining R_{SH} and ρ_c for Ni to low resistivity n-type epitaxial 3C-SiC on p-type Si substrate for 2-D circumstances is shown in Fig. 6.2. The thicknesses of the Ni layer, the SiC layer and the Si substrate are 200 nm, 1.1 μm and 300 μm respectively. The SiC layer was very heavily doped with a N doping concentration of 1×10^{20} cm^{-3}. A low value of ρ_c between Ni and heavily doped n-type 3C-SiC epitaxially formed on <100> Si substrates was obtained. The I-V characteristic of each two-contact pattern of contacts between the Ni layer and epitaxial SiC were ohmic.

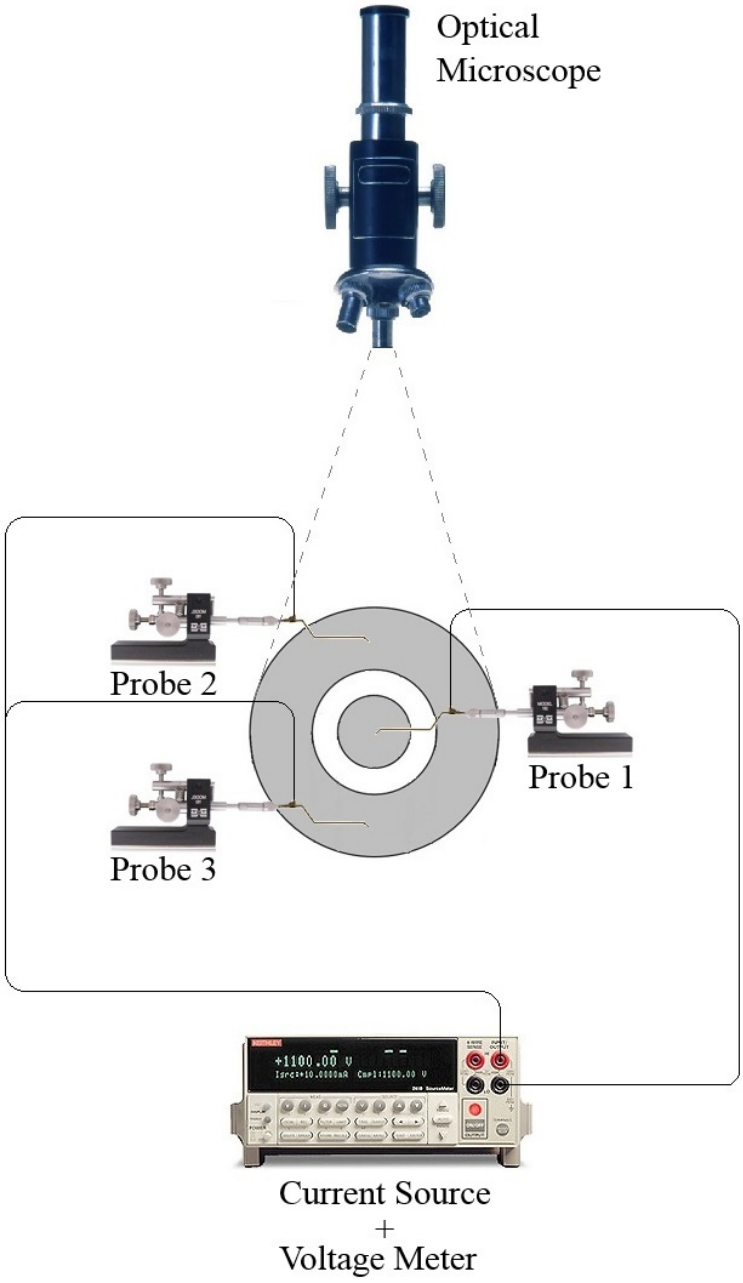

Figure 6.1: Equipment setup for the two-contact circular test structure to determine the total resistance between the two electrodes.

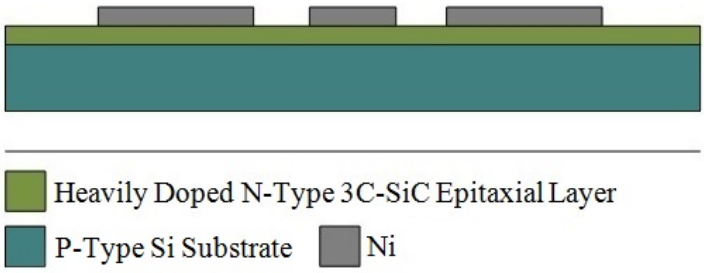

Figure 6.2: Schematic of the cross-section of the fabricated two-contact circular test structure for Ni contacts to very heavily doped n-type 3C-SiC epitaxial layer grown on p-type Si substrate for the 2-D circumstance. The Ni layer, SiC epitaxial layer and Si substrate have thicknesses of 200 nm, 1.1 μm and 300 μm respectively.

Table 6.1: Experimental results for R_{SH} and ρ_c using the two-contact circular test structure for as-deposited Ni to epitaxial 3C-SiC. The Ni layer and the 3C-SiC layer have thicknesses of 200 nm and 1.1 μm respectively. The 3C-SiC layer was very heavily doped with a N doping concentration of 1×10^{20} cm^{-3}. The radius of the central dot contact r_{01} varies from 6 μm to 12 μm. $r_{02}/r_{01} = 1.5$ and $r_{03}/r_{01} = 3.5$ (see Fig. 3.9).

Pattern	αr_0 (no unit)	R_{SH} ($\Omega/\square$)	ρ_c ($\Omega \cdot cm^2$)
1	2.74	27.78	1.3×10^{-6}
2	4.35	30.35	1.2×10^{-6}
3	4.22	29.37	1.3×10^{-6}
4	3.63	29.80	2.4×10^{-6}
5	2.46	28.30	3.6×10^{-6}
6	3.09	28.49	1.2×10^{-6}
7	3.72	29.25	0.8×10^{-6}
8	4.08	28.44	2.4×10^{-6}
9	1.93	27.51	5.7×10^{-6}
10	3.60	29.71	3.2×10^{-6}

As shown in Table 6.1, using the two-contact circular test structure and the method presented in Chapter 3, the experimentally determined ρ_c of as-deposited Ni to n-type 3C-SiC was determined to be $(0.8 - 5.7) \times 10^{-6}$ $\Omega \cdot cm^2$. The sheet resistance R_{SH} is also determined by the novel test structure and the average value is 28.90 $\Omega/\square$ for the SiC layer. The value of R_{SH} was also determined using the Van der Pauw technique [VanderPauw, 1958] and results were consistent

with the results from the two-contact circular test structure.

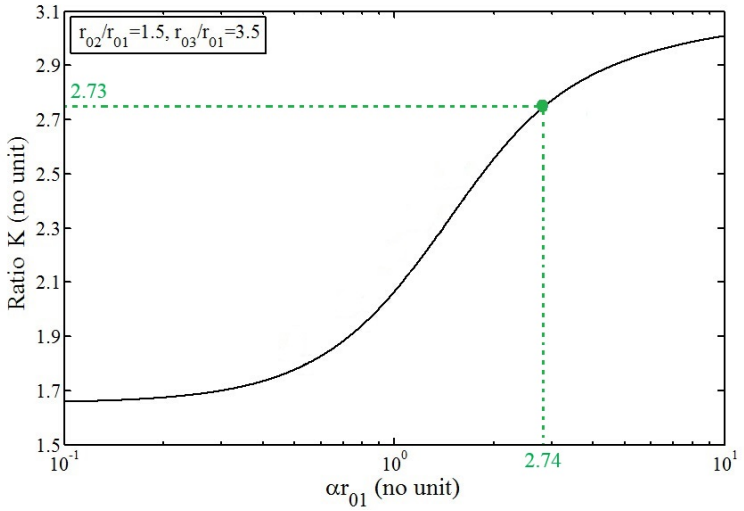

Figure 6.3: The ratio K versus αr_{01} for given ratios of radii ($r_{02}/r_{01} = 1.5$, and $r_{03}/r_{01} = 3.5$). The dash line shows how to obtain the value of αr_{01} using experimentally determined K. Note that αr_{01} is obtained by solving the relevant equation for the given K and is not required to be done graphically.

Here Pattern 1 (results shown at the top of Table 6.1) is taken as an example to demonstrate how to use the two-contact circular test structure and the corresponding ρ_c evaluation technique described in Chapter 3. Pattern 1 consists of three two-contact circular test structures with values of the central dot contact radii r_{01}, r_{02} and r_{03} being 6 μm, 9 μm and 21 μm respectively. The corresponding three total resistances R_{T1}, R_{T2} and R_{T3} were experimentally determined to be 13.2 Ω, 10.6 Ω and 6.1 Ω respectively. The ratio K for these resistances can be calculated using equation 3.19 and it is 2.73. The value of αr_{01} can be found with this known K from Fig. 6.3 which is 2.74 (as demonstrated in Fig. 6.3). Using this value of αr_{01}, $F^{'}$ can be found as shown in Fig. 6.4 and it is 0.35 (The value of F can also be found by choosing the alternative curve in Fig. 6.4). The technique demonstrated by this example using Fig. 6.3 and Fig. 6.4 is for demonstrating only, the actual K, F, $F^{'}$ values are obtained by solving the relevant equations after resistance measurements have been obtained. With known $F^{'}$, R_{SH} can be determined to be 27.78 $\Omega/\square$ using equation 3.15. Finally,

the value of ρ_c can be calculated using equation 3.4 with known R_{SH} and α. As reported in Table 6.1, it is $1.3 \times 10^{-6}\ \Omega \cdot cm^2$. Note that Fig. 6.3 and Fig. 6.4 can be created by using the analytical equations presented in Chapter 3 and they are universal if the scaling equation 3.20 is considered.

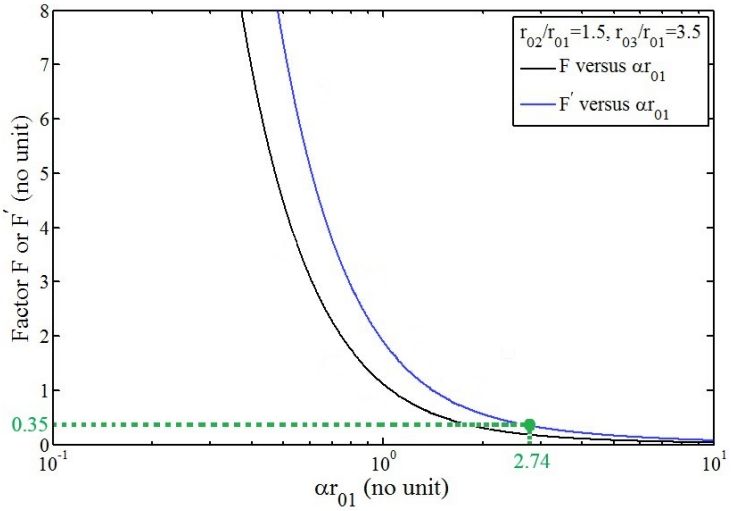

Figure 6.4: F and $F^{'}$ versus αr_{01} for given ratios of radii ($r_{02}/r_{01} = 1.5$, and $r_{03}/r_{01} = 3.5$). The dash line shows how to obtain the value of $F^{'}$ using the known value of αr_{01} obtained in Fig. 6.3. $F^{'}$ can be further used to extract R_{SH} and ρ_c. Note that $F^{'}$ or F is obtained by solving the relevant equation for the given αr_{01} and is not required to be done graphically.

6.2.2 Ti to 3C-SiC Ohmic Contacts

Fig. 6.5 shows a schematic of the cross-section of the fabricated two-contact circular test structure for determining R_{SH} and ρ_c for Ti to high resistivity n-type epitaxial 3C-SiC on p-type Si substrate for the 2-D circumstance. The contact metal is Ti which has a thickness of 400 nm. A lightly doped n-type 3C-SiC epitaxial layer has a thickness of 1.1 μm was grown on a p-type Si substrate with a thickness of 300 μm.

Figure 6.5: Schematic of the cross-section of the fabricated two-contact circular test structure for Ti contacts to a lightly doped n-type 3C-SiC epitaxial layer grown on p-type Si substrate for the 2-D circumstance. The Ti layer, SiC epitaxial layer and Si substrate have the thicknesses of 400 nm, 1.1 μm and 300 μm respectively.

Table 6.2: Experimental results for R_{SH} and ρ_c using the two-contact circular test structure for as-deposited Ti to 3C-SiC. The Ti layer and the 3C-SiC layer have thicknesses of 400 nm and 1.1 μm respectively. The 3C-SiC layer was lightly doped. The radius of the central dot contact r_{01} varies from 6 μm to 12 μm. $r_{02}/r_{01} = 1.5$ and $r_{03}/r_{01} = 3.5$ (see Fig. 3.9).

Pattern	αr_0 (no unit)	R_{SH} $(\Omega/\square)$	ρ_c $(\Omega \cdot cm^2)$
1	3.97	8.6×10^4	3.7×10^{-4}
2	4.18	7.8×10^4	3.0×10^{-4}
3	4.33	8.3×10^4	3.8×10^{-4}
4	3.93	8.2×10^4	4.0×10^{-4}
5	4.01	8.8×10^4	4.6×10^{-4}
6	4.53	8.3×10^4	3.4×10^{-4}
7	5.55	7.8×10^4	3.2×10^{-4}
8	4.27	8.1×10^4	6.3×10^{-4}
9	4.96	7.9×10^4	3.7×10^{-4}
10	3.95	8.2×10^4	7.5×10^{-4}
11	5.47	8.1×10^4	3.1×10^{-4}

ρ_c between Ti and 3C-SiC was determined using the two-contact circular test structure and the method used with this test structure to determine R_{SH} and ρ_c, is presented in Chapter 3. The I-V characteristic of each two-electrode pattern of contacts between the Ti layer and epitaxial SiC were ohmic. Table 6.2 summarizes the results for the patterns where the dimensions vary from $r_{01} = 2.59\ \mu m$, $r_{02} = 5.56\ \mu m$, $r_{03} = 17.46\ \mu m$ to $r_{01} = 3.57\ \mu m$, $r_{02} = 6.75\ \mu m$, $r_{03} = 19.84\ \mu m$. Note that these values are the measured radii which are different from the designed radii. This difference is due to the fabrication conditions. The measurements were performed using 1 μA current. The average values of R_{SH} and ρ_c are $8.2 \times 10^4\ \Omega/\square$ and $4.2 \times 10^{-4}\ \Omega \cdot cm^2$ respectively.

As can be seen from Table 6.2, the values of both R_{SH} and ρ_c show only small variation between the results for test structures of the same and different geometries. This gives confidence in the values obtained by the two-contact circular test structure.

6.2.3 Au/Ni/Ti to Ion Implanted 3C-SiC Ohmic Contacts

The most commonly used ohmic contacts to n-type SiC have consisted of the deposition of a layer of metal (Ni, Ti, Co, Pd or Pt [Feng, 2004]) or C [Lieten et al., 2008] followed by annealing at $\sim 1000°C$. However, the high temperatures required for the localized formation of metal silicides or carbides at the interface has resulted in a degradation of the underlying SiC and a roughening of the metal surface [Feng, 2004]. To investigate its effects on ohmic contacts, ion implantation has previously been used in SiC although very high temperatures ($\sim 1500°C$) have been required for activation [Hui et al., 2006]. An alternative method of modifying the interfacial properties of SiC without the use of high energy ion implantation and high temperatures has been the prior implantation with low energy ions. The bombardment of polycrystalline SiC with low energy Ar ions at 330, 450 and 540 eV has been reported to reduce both the surface energy and internal stress within the layer [Liu et al., 2010]. In Cr to n-type SiC contacts, [Grodzicki et al., 2009] have shown a transition from a non-linear to

a linear I-V response following the bombardment of n-type SiC with Ar ions at 1.2 keV.

In this work, the two-contact circular test structure is used to investigate the effect of ion implantation at low implant energy. Here the effect of prior implantation of n-type SiC with low energy ions on the electrical characteristics of Au/Ni/Ti contacts was examined. Variation in the implant species (C and P) and dose ($10^{13} - 10^{15}$ $ions/cm^2$) were used in investigating for the first time the properties of these contacts. The contact metal (first deposited) is Ti and was selected because of the ability of this metal to form ohmic contacts on n-type SiC at a relatively lower annealing temperature compared to alternative metals [Pan et al., 2013].

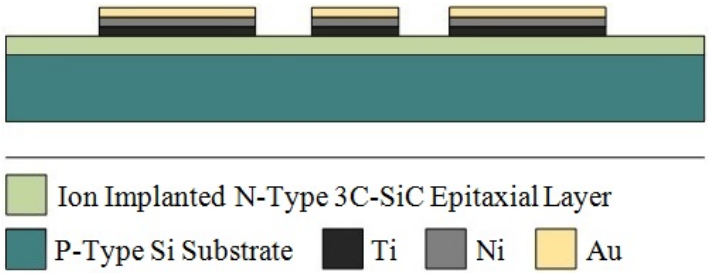

Figure 6.6: Schematic of the cross-section of the fabricated two-contact circular test structure for Au/Ni/Ti contacts to ion implanted (causing damage) and heavily doped (during epitaxial growth) n-type 3C-SiC epitaxial layer grown on p-type Si substrate for the 2-D circumstance. The Au, Ni and Ti layers have the same thickness of 50 μm and the 3C-SiC layer and Si substrate have thicknesses of 1.1 μm and 300 μm respectively. The 3C-SiC layer was very heavily doped with a N doping concentration of $1{\times}10^{20}$ cm^{-3}.

As shown in Fig. 6.6, Ti, Ni and Au layers, with the thickness of 50 μm for each of them, were evaporated on ion implanted 3C-SiC epitaxial layer (with a thickness of 1.1 μm) in sequence. The SiC layer was very heavy doped with a doping concentration of 1×10^{20} cm^{-3}. The reason for using Au/Ni/Ti ohmic contact system is: (i) ohmic contact can be formed between as-deposited Ti and heavy doped SiC [Alok et al., 1993], (ii) Au layer can prevent Ti oxide formation and is easy to probe [Chang et al., 2005] and (iii) the insertion of a Ni layer improves

the thermal stability of Ti ohmic contacts [Mochizuki et al., 1994]. Future work will examine the annealing properties of these Au/Ni/Ti ohmic contacts.

The I-V characteristic of each two-electrode pattern of contacts between the Au/Ni/Ti layer and epitaxial SiC were ohmic. Fig. 6.7 and Fig. 6.8 show the plots of current (I) versus voltage (V) for Au/Ni/Ti contacts on both the unimplanted and ion implanted SiC with both C and P ions. For the unimplanted samples, the I-V response was ohmic with a relatively low resistance. For each of the C and P implants, Fig. 6.7 and Fig. 6.8 also show that I-V plots were linear with a decrease in slope or increase in the resistance of the Au/Ni/Ti contacts with increase in implant dose.

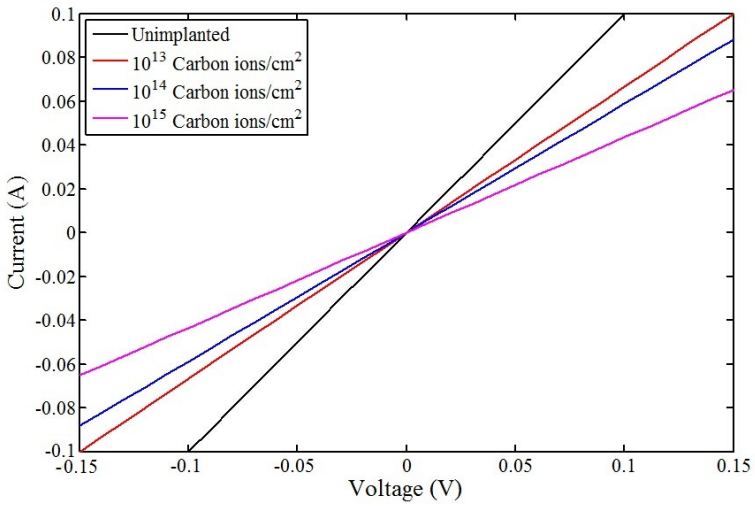

Figure 6.7: Plots of I-V characteristics for Au/Ni/Ti contacts on unimplanted n-type epitaxial 3C-SiC and after implantation with C ions at doses of 1×10^{13}, 1×10^{14} and 1×10^{15} $ions/cm^2$. The n-type epitaxial 3C-SiC layer has a N doping concentration of 1×10^{20} cm^{-3}. The Au, Ni and Ti layers have the same thickness of 50 μm and the 3C-SiC layer and Si substrate have thicknesses of 1.1 μm and 300 μm respectively.

Fig. 6.9 shows measurements of R_{SH} plotted as a function of implant dose. The average value of R_{SH} for the unimplanted samples was determined to be 26.5 $\Omega/\square$. It shows that the implantation of the SiC with C ions at a dose of

1×10^{13} $ions/cm^2$ has resulted in only a small increase in R_{SH}. However, the implantation at higher doses of 1×10^{14} and 1×10^{15} C $ions/cm^2$ has resulted in a sharp rise in R_{SH}. In comparison, the implantation of SiC with P ions has resulted in negligible change in R_{SH} for surfaces implanted with lower doses and a significant increase at 1×10^{15} phosphorus $ions/cm^2$. Fig. 6.9 shows that the increase in R_{SH} with dose was greater in magnitude for C ion implants than with an equivalent dose of P ions. The trends in both Fig. 5.7 and Fig. 5.8 in Chapter 5 have indicated that the deeper penetration of the lower mass C ions into SiC had a greater effect in increasing both R_{SH} and ρ_c than the shallower damage generated by the higher mass P ions. The similarity between the effects of dose on R_{SH} below the contact interface and ρ_c was consistent with the direct dependence of ρ_c on semiconductor resistivity ρ_b within the model for the two-contact circular test structure [Pan et al., 2013].

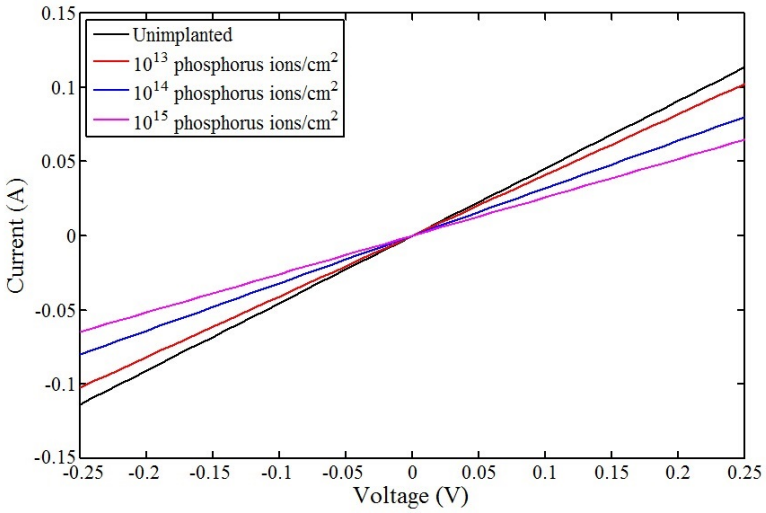

Figure 6.8: Plots of I-V characteristics for Au/Ni/Ti contacts on unimplanted n-type epitaxial 3C-SiC and after implantation with P ions at doses of 1×10^{13}, 1×10^{14} and 1×10^{15} $ions/cm^2$. The n-type epitaxial 3C-SiC layer has a N doping concentration of 1×10^{20} cm^{-3}. The Au, Ni and Ti layers have the same thickness of 50 μm and the 3C-SiC layer and Si substrate have thicknesses of 1.1 μm and 300 μm respectively.

The measurements of ρ_c versus implant dose for Au/Ni/Ti contacts have been

plotted in Fig. 6.10. For the unimplanted SiC, the value of ρ_c was determined to be $1.3 \times 10^{-6}\ \Omega \cdot cm^2$. With implantation at doses of 1×10^{13} and 1×10^{14} C $ions/cm^2$, the magnitude of ρ_c was greater by a factor of ~ 2 than the value for the unimplanted SiC. In Fig. 6.10, a steep rise in ρ_c was evident only at an implant dose of 1×10^{15} C $ions/cm^2$. The implantation with C ions at 1×10^{15} C $ions/cm^2$ has resulted in a higher value of $\rho_c = 1.8 \times 10^{-4}\ \Omega \cdot cm^2$ than for P implants at this dose for which $\rho_c = 4.1 \times 10^{-5}\ \Omega \cdot cm^2$. The reason for this increasing in ρ_c is, before a dose of 1×10^{15} $ions/cm^2$, the defect concentration arising from damage production during implantation tend to saturate at a certain concentration. This certain concentration is far below that required for amorphization in 3C-SiC. After a threshold dose of 1×10^{15} $ions/cm^2$, the concentration of implanted atoms become significant and the surface of the epitaxial 3C-SiC layer, where ρ_c is extracted from, is seriously damaged [Zhong et al., 2004].

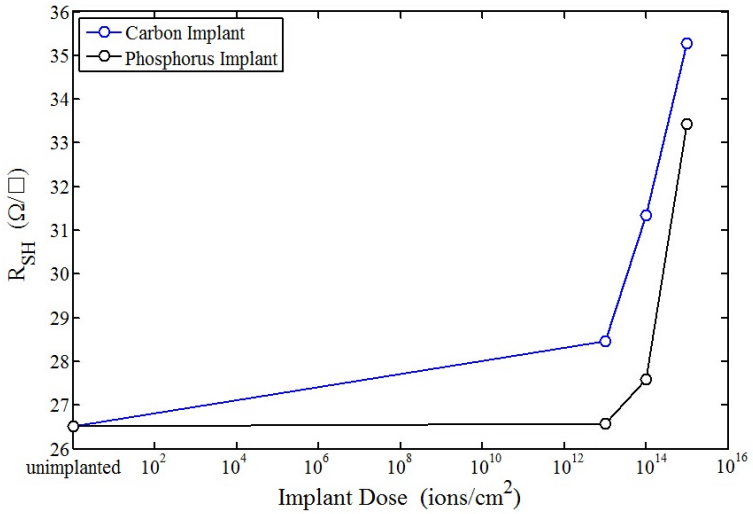

Figure 6.9: Sheet resistance, R_{SH}, versus dose for Au/Ni/Ti contacts to unimplanted SiC and implanted with C or P ions at 5 keV. The n-type epitaxial 3C-SiC layer has a N doping concentration of $1 \times 10^{20}\ cm^{-3}$. The Au, Ni and Ti layers have the same thickness of 50 μm and the 3C-SiC layer and Si substrate have thicknesses of 1.1 μm and 300 μm respectively. The radius of the central dot contact r_{01} varies from 6 μm to 12 μm. $r_{02}/r_{01} = 1.5$ and $r_{03}/r_{01} = 3.5$ (see Fig. 3.9). Experimental data are shown in Appendix D.

Previous studies of the damage induced by P implantation in 3C-SiC by [Song et al., 2011] have identified the formation of high densities of dislocation loops following implantation with P ions at $20-250\ keV$ and similarly in 4H-SiC [Chunjuan et al., 2012]. In addition, [Takeda et al., 2014] have reported four types of damage after low energy ($20\ keV$) implantation in 6H-SiC. The type of damage was shown as dependent on the ion concentration. Based on the levels of ion concentration required for different types of damage, the results in [Takeda et al., 2014] have indicated that for the results reported in this thesis, the samples are located either in a zone of (i) negligible damage to the crystal structure or (ii) extensive formation of defect structures and damage to the lattice. These two levels of damage were consistent with (i) the low dose region characterised by little change in R_{SH} and ρ_c and (ii) the higher dose region (1×10^{15} C $ions/cm^2$) which was accompanied by a sharp increase in both R_{SH} and ρ_c.

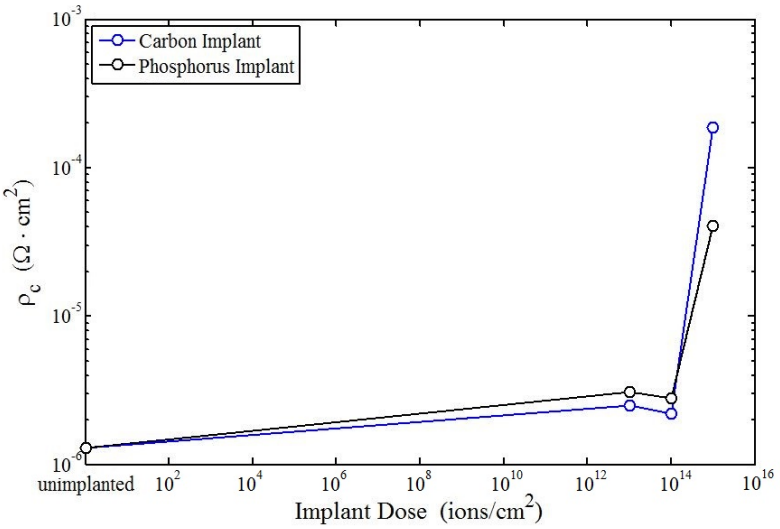

Figure 6.10: Specific contact resistance, ρ_c, versus dose for Au/Ni/Ti contacts to unimplanted SiC and implanted with C or P ions at 5 keV. The n-type epitaxial 3C-SiC layer has a N doping concentration of $1 \times 10^{20}\ cm^{-3}$. The Au, Ni and Ti layers have the same thickness of 50 μm and the 3C-SiC layer and Si substrate have thicknesses of 1.1 μm and 300 μm respectively. The radius of the central dot contact r_{01} varies from 6 μm to 12 μm. $r_{02}/r_{01} = 1.5$ and $r_{03}/r_{01} = 3.5$ (see Fig. 3.9). Experimental data are shown in Appendix D.

The low energy implantation of 3C-SiC with P or C ions at doses of 10^{13} –

10^{15} $ions/cm^2$ has resulted in an increase in specific contact resistivity, ρ_c, of Au/Ni/Ti contacts. A sharp increase in ρ_c was evident for an increased implant dose of 1×10^{15} $ions/cm^2$. This trend in ρ_c, has correlated with a rise in sheet resistance, R_{SH}, of SiC with increase in implant dose. The implantation of SiC with C ions has resulted in higher values of R_{SH} at each dose compared with the equivalent implants using P ions. However, the implantation of SiC with C ions has resulted in lower values of ρ_c at each dose compared with the equivalent implants using P ions, except at the dose 1×10^{15} cm^{-2}.

The implantations in SiC used in previous studies [Song et al., 2011] have been performed at higher energies ($20 - 250$ keV) than the 5 keV used in the present work. However, the equivalence of ion concentration has allowed some comparison of the results.

6.3 Specific Contact Resistivity Evaluation Using The Two-Contact Circular Test Structure for Contacts to Bulk Semiconductors

6.3.1 Ni to Bulk Ge Ohmic Contacts

In Fig. 6.11, a cross-section of the fabricated two-contact circular test structure for determining ρ_c for Ni to p-type Ge substrate for 3-D circumstances is presented. The thickness of the contact metal, Ni, is 200 nm. The p-type Ge substrate has a thickness of 220 μm which can be considered as infinite when using the ρ_c evaluation technique reported in Chapter 4.

The resistivity for the Ge substrates was determined before the wafer was diced using the four point probe technique [Valdes, 1952] and it was determined to be $0.035\ \Omega \cdot cm$. The total resistance measurements between the two electrodes were taken for ten different dimensions of the two-contact circular test patterns. The I-V characteristic of each two-contact circular pattern indicates that ohmic

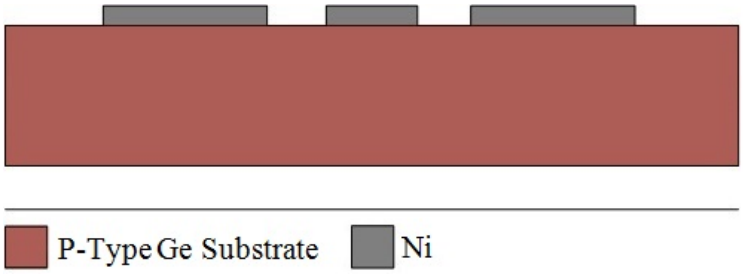

Figure 6.11: Schematic of the cross-section of the fabricated two-contact circular test structure for determining ρ_c for Ni to p-type Ge substrate for the 3-D circumstance. The Ni layer and the Ge substrate have thicknesses of 200 nm and 220 μm respectively. The Ge substrate has a resistivity of 0.035 $\Omega \cdot cm$.

contacts were generated between as-deposited Ni and Ge. As shown in Table 6.3, the measured total resistance R_T ranged from 4.43 Ω to 17.23 Ω for patterns with different dimensions. The values of ρ_c were then determined using the method presented in Chapter 4 and varied from 2.3×10^{-6} $\Omega \cdot cm^2$ to 2.7×10^{-5} $\Omega \cdot cm^2$.

Table 6.3: Experimental results for ρ_c using the two-contact circular test structure for as-deposited Ni to a p-type Ge substrate. The Ni layer and the Ge substrate have thicknesses of 200 nm and 220 μm respectively. The Ge substrate has a resistivity of 0.035 $\Omega \cdot cm$.

Pattern	Size	R_T (Ω)	ρ_c ($\Omega \cdot cm^2$)
1	A[1]	15.68	3.7×10^{-6}
2	A[1]	17.23	6.5×10^{-6}
3	A[1]	14.77	2.3×10^{-6}
4	B[2]	6.98	1.3×10^{-5}
5	B[2]	6.48	1.1×10^{-5}
6	B[2]	5.93	7.9×10^{-6}
7	B[2]	5.54	5.3×10^{-6}
8	B[2]	6.06	8.8×10^{-6}
9	C[3]	4.43	2.1×10^{-5}
10	C[3]	4.78	2.7×10^{-5}

[1] $r_0 = 6$ μm, $r_1 = 10$ μm, $r_1^{'} = 18$ μm.
[2] $r_0 = 15$ μm, $r_1 = 25$ μm, $r_1^{'} = 45$ μm.
[3] $r_0 = 24$ μm, $r_1 = 40$ μm, $r_1^{'} = 72$ μm.

The results show that with known semiconductor substrate resistivity ρ_b, fixed geometry, and using scaling equation 4.5, as required, ρ_c can be determined conveniently from universal plots of R_T versus ρ_c as presented in Fig. 4.6 in Chapter 4.

Fig. 6.12 shows how to use the graphical method to extract ρ_c in 3-D circumstances described in Chapter 4. Pattern 1 (results shown at the top of Table 6.3) is taken as an example. Fig. 4.6 is scaled to Fig. 6.12 using the scaling equation 4.5 (note that $m = 2$ and $n = 1.75$ for this example). The curve which is shown at the top of Fig. 6.12 represents the top curve shown in Fig. 4.6 with a new value of $\rho_b = 0.035\ \Omega \cdot cm$ using the scaling equation 4.5. This value is the bulk Ge resistivity determined using the four point probe technique in this section. The total resistance R_T of Pattern 1 is determined to be 15.68 Ω. Using this value and the dash line in Fig. 6.12, ρ_c with the value of $3.7 \times 10^{-6}\ \Omega \cdot cm^2$ can be easily found.

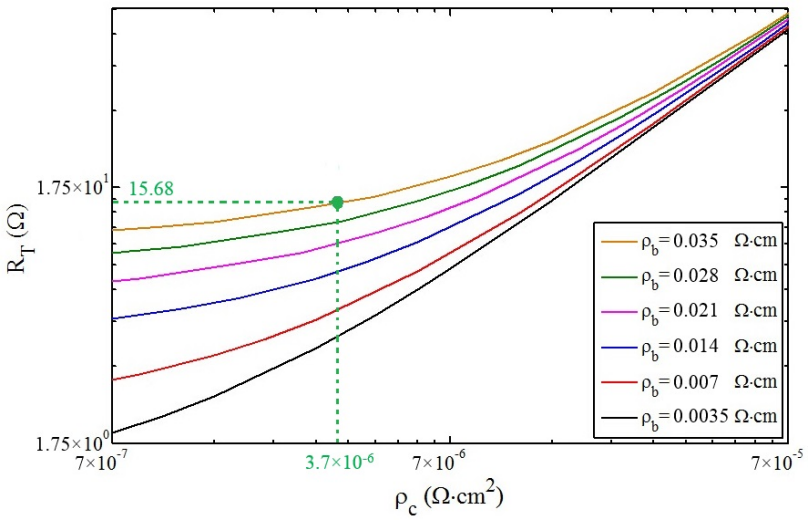

Figure 6.12: FEM analysis results showing R_T plotted as a function of ρ_c with ρ_b varying from 0.0035 $\Omega \cdot cm$ to 0.035 $\Omega \cdot cm$. Geometry is fixed: $r_0 = 6\ \mu m$, $r_1 = 10\ \mu m$ and $r_1^{'} = 18\ \mu m$. The dash line shows how to obtain ρ_c using experimentally determined R_T. Note that this figure is created by scaling Fig. 4.6 using scaling equation 4.5.

6.3.2 Ti to Bulk 4H-SiC Ohmic Contacts

Fig. 6.13 shows a schematic of the cross-section of the fabricated two-contact circular test structure for determining ρ_c for Ti to n-type 4H-SiC substrate. The contact metal Ni and n-type 4H-SiC have thicknesses of 150 nm and 330 μm respectively.

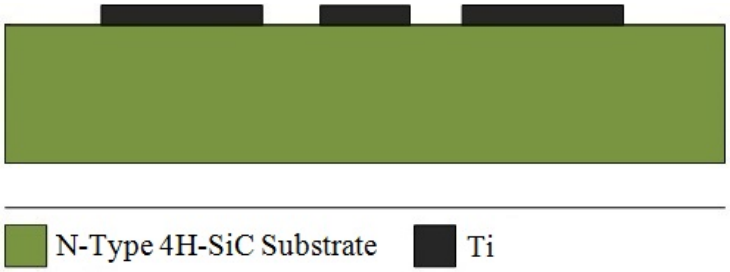

Figure 6.13: Schematic of the cross-section of the fabricated two-contact circular test structure for determining ρ_c for Ti to n-type 4H-SiC substrate for the 3-D circumstance. The Ti layer and the 4H-SiC substrate have thicknesses of 150 nm and 330 μm respectively. The n-type 4H-SiC substrate has a resistivity of 0.01 $\Omega \cdot cm$.

The resistivity for the 4H-SiC substrates was determined before the wafer was diced, using the four point probe technique and it was determined to be 0.01 $\Omega{\cdot}cm$. The total resistance measurements between the two electrodes were taken for ten different dimensions of the two-contact circular test patterns. After annealing the samples in argon gas at 1100°C for 30 minutes, the I-V characteristic of each two-contact circular pattern indicates that ohmic contacts were generated between Ti and 4H-SiC. As shown in Table 6.4, the measured total resistance R_T ranged from 63 Ω to 150 Ω for patterns with different dimensions. The values of ρ_c were then determined using the method presented in Chapter 4 and varied from 1.8×10^{-3} $\Omega \cdot cm^2$ to 2.5×10^{-3} $\Omega \cdot cm^2$.

Table 6.4: Experimental results for ρ_c using the two-contact circular test structure for Ti to a n-type 4H-SiC substrate. The Ti layer and the 4H-SiC substrate have thicknesses of 150 nm and 330 μm respectively. The 4H-SiC substrate has a resistivity of 0.01 $\Omega \cdot cm$.

Pattern	Size	R_T (Ω)	ρ_c ($\Omega \cdot cm^2$)
1	A[1]	125	1.8×10^{-3}
2	A[1]	129	1.9×10^{-3}
3	A[1]	137	2.1×10^{-3}
4	A[1]	150	2.5×10^{-3}
5	A[1]	140	2.4×10^{-3}
6	B[2]	70	1.5×10^{-3}
7	B[2]	63	1.3×10^{-3}
8	B[2]	98	2.1×10^{-3}
9	B[2]	96	2.1×10^{-3}
10	B[2]	100	2.2×10^{-3}

[1] $r_0 = 24\ \mu m$, $r_1 = 40\ \mu m$, $r_1^{'} = 72\ \mu m$.
[2] $r_0 = 30\ \mu m$, $r_1 = 50\ \mu m$, $r_1^{'} = 90\ \mu m$.

6.4 Summary

This chapter provides the experimental results for the new techniques presented in Chapter 3 and 4 to accurately determine the values of ρ_c between metal and semiconductor in both 2-D (e.g. thin epitaxial layer) and 3-D (e.g. thick substrate) circumstances. The two-contact circular test structures were used and the samples were prepared as described in Chapter 5.

The values of ρ_c of Ni to 3C-SiC (very heavily doped with a doping concentration of $1 \times 10^{20}\ cm^{-3}$ and has thickness of 1.1 μm) ohmic contacts and Ti to 3C-SiC (lightly doped and has thickness of 1.1 μm) were determined to be $(0.8 - 5.7) \times 10^{-6}\ \Omega \cdot cm^2$ and $(3.0 - 7.5) \times 10^{-4}\ \Omega \cdot cm^2$ respectively. The effect of low energy implantation of P or C ions in 3C-SiC (very heavily doped with a doping concentration of $1 \times 10^{20}\ cm^{-3}$ and has thickness of 1.1 μm) on the properties of Au/Ni/Ti contacts has been examined for doses in the range $10^{13} - 10^{15}\ ions/cm^2$. This effect has resulted in an increase in specific contact resistance, ρ_c, of Au/Ni/Ti contacts. A sharp increase in ρ_c was evident for an

implant dose of 1×10^5 $ions/cm^2$. This trend in ρ_c, has correlated with a rise in sheet resistance, R_{SH}, of SiC with increase in implant dose. The values of ρ_c of Ni to bulk Ge (resistivity of 0.035 $\Omega \cdot cm$) and Ti to 4H-SiC substrate (resistivity of 0.01 $\Omega \cdot cm$) ohmic contacts were determined to be $(2.3 - 27) \times 10^{-6}$ $\Omega \cdot cm^2$ and $(1.8 - 2.5) \times 10^{-3}$ $\Omega \cdot cm^2$ respectively. Lower ρ_c can be obtained by heat treatment since it improves the ohmic contact between metal and semiconductor and reduces the total resistance. However, smaller patterns are required according to the scaling equation 4.5.

Chapter 7

Conclusion and Future Research

7.1 Conclusion

This thesis introduces new ohmic contact test structures and the methods for ohmic contact characterisation between a metal and semiconductor in both two-dimensional (2-D) and three-dimensional (3-D) circumstances using these test structures. The issues with regards to error correction, difficulty in analysing results and difficulty in fabrication, lead to the development of the new test structures reported here. These issues are summarised as follows:

(i) Active layer definition
A mesa isolation or selective area doping is commonly required for characterising ohmic contacts to the active layer (e.g. n^+ epitaxial on n^- substrate, diffused or implanted active layer) when using the transmission line model (TLM) or the cross-bridge Kelvin resistor (CBKR) test structures. The current behavior can be confined by using mesa isolation. However, For some semiconductor compounds such as SiC and GaAs, mesa isolation can be very difficult. In the test structure reported here there is no requirement regarding the active layer to have a mesa isolation other than ensuring that it extends as far as the outer electrode.

(ii) Contact misalignment and overlap
The analytical expressions for some test structures such as the TLM and the CBKR are based on the ideal models. However, in an actual contact,

misalignment and overlap always occurs. Therefore, error corrections are always required, otherwise the analytical expressions will give incorrect values for ρ_c. For the test structure reported here, the fabricated test structure can be regarded as ideal. This comes about because the electrodes are circular as designed and remain circular after fabrication. Analytical solutions are offered using the actual electrode radii and the actual measured resistances with no correction factor as there is for the above test structure due to misalignment and overlap.

(iii) Equipotential problem

The new test structure presented here do not have this problem. It occurs in the circular transmission line model (CTLM) where there is an annular ring, one of the three concentric electrodes in the CTLM test structure. It is known that it is difficult (but essential for accurate analysing to determine ρ_c) to have this electrode at an equipotential because it is necessarily narrow. This problem will affect the accuracy of the electrical testing results. Increasing the number of the probes (and shorting them all together) can help to solve this issue but will make the testing very difficult. The new test structure do have circular concentric electrodes but only two of them and neither is an annular ring. The outer electrode of the new test structure could be designed and fabricated to give a wide annular ring but this is not required. In fact, the boundary of the outer electrode can extend to infinite.

(iv) Complicated analytical expressions

The CTLM, for example, is simple to be fabricated. However, the analytical expressions are quite complicated. This issue increases the difficulty in analysing results. The new test structures reported in this thesis are also relatively simple to be fabricated but do not have the same difficulty in processing the results to determine R_{SH} and ρ_c.

(v) Vertical voltage drop

This is a big issue for all of the 2-D test structures. Error corrections are required to correct the electrical testing results. When the semiconductor layer in a metal-to-semiconductor contact is neither true 2-D nor true 3-D,

there will always be some error, and error correction is required. For the test structure presented here, accurate results can be always determined when semiconductor layer can be regarded as truly 2-D or 3-D. The test structure reported here for the 3-D situation is the first ever to be reported that is suitable for metal contacts to thick active layers or to a substrate.

In summary, all of the above issues with conventional test structures have been addressed and improved by the novel test structures developed for ohmic contact characterisation in both 2-D and 3-D circumstances during this Ph.D. programme. The corresponding methods for determining ρ_c have also been presented and demonstrated using finite element modeling (FEM). The two-contact circular test structure does not require mesa isolation and correction factors are unnecessary. Furthermore, the analytical expressions are relatively simple compared to the conventional CTLM test structure.

7.1.1 The Two-Contact Circular Test Structure for The 2-D Circumstance

The novel two-contact circular test structure consists of a central dot electrode and an outer electrode. The analytical equations were developed and it has been demonstrated using FEM. A number of models with the values of R_{SH} and ρ_c being 3 $\Omega/\square$ to 3000 $\Omega/\square$ and 1×10^{-9} $\Omega \cdot cm^2$ to 1×10^{-2} $\Omega \cdot cm^2$ respectively were modeled for demonstrating the new test structure. Results showed that there was excellent agreement between analytical and FEM results.

Three pairs of the two-contact circular test structures were demonstrated to derive R_{SH} and ρ_c by eliminating the outer contact resistance R_{C1} from developed analytical expressions. The scaling equation was also given to show that the structure is universal for use with different metal to semiconductor ohmic contacts.

A number of metal to semiconductor ohmic contacts have been fabricated to examine the two-contact circular test structure for contacts to 2-D semiconductor layers (2-D circumstances) using both the wet etching and the lift off techniques. The values of ρ_c for Ni to heavily doped n-type epitaxial 3C-SiC ohmic contacts and Ti to lightly doped n-type epitaxial 3C-SiC were determined to be $(0.8 - 5.7) \times 10^{-6}\ \Omega \cdot cm^2$ and $(3.0 - 7.5) \times 10^{-4}\ \Omega \cdot cm^2$ respectively using the two-contact circular test structure and its corresponding analytical method. In addition, the effect of low energy implantation on the properties of Au/Ni/Ti contacts to heavily doped n-type epitaxial 3C-SiC was investigated using this new test structure. The experimental results showed that ρ_c increases with the increasing dose of the implanted ions. The accuracy of the test structure is valuable in being able to identify the effects of small changes in processing on electrical properties (R_{SH} and ρ_c).

7.1.2 The Two-Contact Circular Test Structure for The 3-D Circumstance

To investigate the two-contact circular test structure for 3-D circumstances, a number of 3-D models were analyzed using FEM with semiconductor resistivity ρ_b and specific contact resistivity ρ_c varying from $0.001\ \Omega \cdot cm$ to $0.01\ \Omega \cdot cm$ and $1 \times 10^{-8}\ \Omega \cdot cm^2$ to $1 \times 10^{-3}\ \Omega \cdot cm^2$ respectively. The geometry size was fixed. Results showed that with known semiconductor resistivity ρ_b, fixed geometry, ρ_c can be determined easily and accurately using a graphical method. This method is suitable to different metal to semiconductor contacts for the 3-D circumstance using the scaling equation which was given in this thesis as well.

To demonstrate the novel test structure for contacts to bulk semiconductors (3-D circumstances), a number of metal contacts were fabricated on semiconductor substrates using the lift off technique. The values of ρ_c of Ni to p-type bulk Ge and Ti to n-type 4H-SiC substrate ohmic contacts were determined to be $(2.3 - 27) \times 10^{-6}\ \Omega \cdot cm^2$ and $(1.8 - 2.5) \times 10^{-3}\ \Omega \cdot cm^2$ respectively using the

two-contact circular test structure and the corresponding method. Prior to the work for this Ph.D. programme, there are no reported test structures for determining the specific contact resistivity of ohmic contact to bulk semiconductors (e.g. substrates or thick epitaxial layers).

7.2 Future Research

The two-contact circular ohmic contact test structure and its ρ_c evaluation techniques in both 2-D and 3-D circumstances can be applied to any metal to semiconductor contacts using scaling equations to obtain accurate results. Furthermore, most of the samples investigated here are ohmic contacts without heat treatment. Future work will examine the effects of heat treatment on these different metal to semiconductor contacts, especially the implanted Au/Ni/Ti contacts.

An alternative method using reduced two-contact circular test structure analytical expressions to extract ρ_c in 2-D circumstances is shown in Appendix B. This method has been analysed using FEM. Future work will examine on this method using experimental results.

Another novel test structure which is a combination of the TLM and the CTLM is presented in Appendix E. FEM shows that there is excellent agreement between the analytical expressions and modeling results. It has the same advantages as the two-contact circular test structure has but simpler analytical equations. There is scope for further development of this test structure, including experimental work.

Appendix A

The Definitions of The Functions for Use in The CTLM Test Structure

$$A(r,x) = I_1(\alpha r) \cdot K_0(\alpha x) + I_0(\alpha x) \cdot K_1(\alpha r) \tag{A.1}$$

$$B(r,x) = I_1(\alpha x) \cdot K_0(\alpha r) + I_0(\alpha r) \cdot K_1(\alpha x) \tag{A.2}$$

$$C(r,x) = I_1(\alpha r) \cdot K_1(\alpha x) - I_1(\alpha x) \cdot K_1(\alpha r) \tag{A.3}$$

$$D(r,x) = I_0(\alpha x) \cdot K_0(\alpha r) - I_0(\alpha r) \cdot K_0(\alpha x) \tag{A.4}$$

$$E(r) = I_0(\alpha r) / I_1(\alpha r) \tag{A.5}$$

Note that I_0 and I_1 are the zeroth and first order modified Bessel functions of the first kind respectively. K_0 and K_1 are the zeroth and first order modified Bessel functions of the second kind respectively.

Appendix B

Proposed Two-Contact Circular Test Structure −− An Alternative Specific Contact Resistivity Evaluation Technique for 2-D Circumstances

B.1 Using Reduced Analytical Expressions of The Two-Contact Circular Test Structure for Determining Specific Contact Resistivity

In this section, an alternative method for determining ρ_c in two-dimensional (2-D) circumstances using the two-contact test structure presented in Chapter 3 is

discussed and demonstrated using finite element modeling (FEM).

As discussed in Chapter 3, equation 3.3 gives the full analytical expression for the central dot contact resistance R_{C0}. Note that I_0 and I_1 are the zeroth and first order modified Bessel function of the first kind respectively and equations B.1 and B.2 are the asymptotic forms of the zeroth and first order modified Bessel function of the first kind.

$$I_0\left(\alpha r_0\right) = \left[1 + \frac{\left(\alpha r_0/2\right)^2}{1} + \frac{\left(\alpha r_0/2\right)^4}{2 \cdot 2} + \cdots\right] \tag{B.1}$$

$$I_1\left(\alpha r_0\right) = \frac{\alpha r_0}{2}\left[1 + \frac{\left(\alpha r_0/2\right)^2}{2} + \frac{\left(\alpha r_0/2\right)^4}{2 \cdot 2 \cdot 3} + \cdots\right] \tag{B.2}$$

For small values of αr_{01}, the terms in equations B.1 and B.2 can be reduced. In order to examine the accuracy of a limited number of terms, the effect of using only the first term, the first two terms and the first three terms in equations B.1 and B.2 are considered separately.

Firstly, considering the first term in equations B.1 and B.2, after substituting equations 3.4, B.1 and B.2 in equation 3.3, a reduced equation for R_{C0} can be obtained

$$R'_{C0} = \frac{R_{SH}}{\pi\alpha^2 r_0^2} \tag{B.3}$$

Note that this is the equation for R_{C0}, when the current is uniform across the interface. This occurs for long transfer lengths i.e. $\alpha r_0 \ll 1$.

Secondly, considering the first two terms in equations B.1 and B.2, I_0 is divided by I_1, and then equations 3.4, B.1 and B.2 are substituted in equation 3.3, hence:

$$R''_{C0} = R'_{C0}\left(1 + \frac{\alpha^2 r_0^2}{\alpha^2 r_0^2 + 8}\right) \tag{B.4}$$

Finally, considering the first three terms in equations B.1 and B.2

$$R'''_{C0} = R'_{C0}\left(1 + \frac{2\alpha^4 r_0^4 + 24\alpha^2 r_0^2}{\alpha^4 r_0^4 + 24\alpha^2 r_0^2 + 192}\right) \tag{B.5}$$

As shown in equation 3.5, the parasitic resistance R_P is only determined by the ratio of r_1 and r_0 since the sheet resistance R_{SH} is always the same. Therefore, R_P is a constant if the ratio of r_1 and r_0 does not change.

The outer electrode contact resistance is a function of r_1 and $r_1^{'}$ and it is given in equation 3.6, where K_0 and K_1 are the zeroth and first order modified Bessel function of the second kind respectively. Note that αr_1 and $\alpha r_1^{'}$ used in the analytical model are large values compared to αr_0. The asymptotic forms of I_0, I_1, K_0 and K_1 for large values are shown below, where $x = \alpha r \gg 1$.

$$I_0(x) = \frac{e^x}{\sqrt{2\pi x}}\left(1 + \frac{1}{8x} + \frac{9}{128x^2} + \cdots\right) \tag{B.6}$$

$$I_1(x) = \frac{e^x}{\sqrt{2\pi x}}\left(1 - \frac{3}{8x} - \frac{15}{128x^2} - \cdots\right) \tag{B.7}$$

$$K_0(x) = \sqrt{\frac{\pi}{2x}}e^{-x}\left(1 - \frac{1}{8x} + \frac{9}{128x^2} - \cdots\right) \tag{B.8}$$

$$K_1(x) = \sqrt{\frac{\pi}{2x}}e^{-x}\left(1 + \frac{3}{8x} - \frac{15}{128x^2} + \cdots\right) \tag{B.9}$$

For large values of x, terms after the second term in equations B.6 - B.9 can be neglected. Considering the first term in equations B.6 - B.9, using αr_1 and $\alpha r_1^{'}$ to replace x and substitute them in equation 3.6

$$R_{C1} = \frac{R_{SH}}{2\pi\alpha r_1}\coth\left(\alpha r_1^{'} - \alpha r_1\right) \tag{B.10}$$

As reported by [Marlow and Das, 1982], equation B.10 can be reduced to

$$R'_{C1} = \frac{R_{SH}}{2\pi\alpha r_1}, \ where\ r'_1 \to \infty \coth\left(\alpha r'_1 - \alpha r_1\right) \to 1 \tag{B.11}$$

Considering the first two terms in equations B.6 - B.9, equation 3.6 can be written as:

$$R_{C1} = \frac{R_{SH}}{2\pi\alpha r_1} \frac{(1 - 1/8\alpha r_1) + e^{2\alpha r_1 - 2\alpha r'_1}\left[\frac{(1+1/8\alpha r_1)(1+3/8\alpha r_1)}{(1-3/8\alpha r_1)}\right]}{(1 + 3/8\alpha r_1) - e^{2\alpha r_1 - 2\alpha r'_1}\left[\frac{(1-3/8\alpha r_1)\left(1+3/8\alpha r'_1\right)}{\left(1-3/8\alpha r'_1\right)}\right]} \tag{B.12}$$

Since r'_1 is much greater than r_1, equation B.12 can be reduced to:

$$R''_{C1} = R'_{C1}\left(1 - \frac{4}{8\alpha r_1 + 3}\right) \tag{B.13}$$

The details of the modeling are similar to those in section 2 Chapter 3. An ohmic contact with a semiconductor sheet resistance (R_{SH}) and specific contact resistance (ρ_c) values of 3000 $\Omega/\square$ and $1 \times 10^{-4}\ \Omega \cdot cm^2$ respectively are used as an example in both the analytical model and FEM. Since the metal contacts are assumed to be at an equipotential, this implies zero resistance for the metal layer. The values of r_0 range from 1 μm to 5 μm, and the corresponding values of r_1 are from 1.5 μm to 7.5 μm, which are always 1.5 times greater than the values of r_0 (to keep the contribution of R_P to the total resistance R_T small). The values of r'_1 are 10 times greater than r_0 in the FEM analysis (when r'_1 is beyond a certain value, it does not matter that the outer ring contact shown in Fig. 3.1 as a ring, is not a ring). Scaling of these parameters is presented later to show how these parameters affect the behavior and accuracy of the proposed test structure.

Fig. B.1 shows a comparison of results obtained using equations B.3 - B.5 for R_{C0}. It is clearly seen that equations B.4 and B.5 match the FEM results better than equation B.3. There is a turning region for all the plots in Fig. B.1 when αr_0 is approximately 2 to 4. Beyond this region of αr_0, R_{C0} changes slightly

and tends towards zero. In this case, R_{C0} is not a significant part in the total resistance R_T, and hence structures with $\alpha r_0 > 4$ are not appropriate to extract ρ_c.

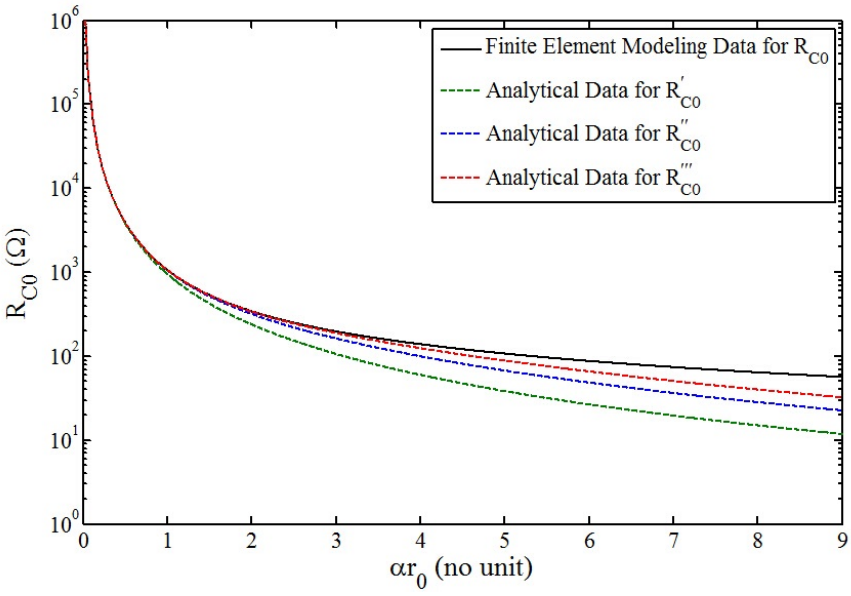

Figure B.1: Comparison of the central dot electrode resistance R_{C0} with αr_0 ranging from zero to nine. The analytical results using equations B.3 - B.5 and FEM data are presented. $R_{SH} = 3000\ \Omega/\square$, $\rho_c = 1 \times 10^{-4}\ \Omega \cdot cm^2$, r_0 is from 1 μm to 15 μm.

There is a slight difference between equation B.5 and FEM when αr_0 is greater than 3. That is probably because 3 is not a small value for equation B.5 and does not meet the constraint of this equation. Similarly, there is a mismatching for equation B.4 when αr_0 is greater than 2. Equation B.3 has a greater error than equations B.4 and B.5 and it is concluded that equation B.3 is acceptable only when αr_0 is less than 1.

Considering the FEM as giving the exact value of R_{C0}, by calculating the data obtained from the analytical and FEM results, the average error for equations B.3 - B.5 when $\alpha r_0 > 4$ are 26.89%, 7.95% and 2.30% respectively. Inspection of Fig. B.1 indicates that equations B.4 and B.5 are acceptable to calculate the central dot contact resistance R_{C0} with equation B.5 being the most accurate.

The FEM results have good agreement on the analytical results using equation 3.5 for the parasitic resistance R_P with increasing r_0. The average error for R_P is only 0.44%, which demonstrates the good matching between analytical and the FEM models.

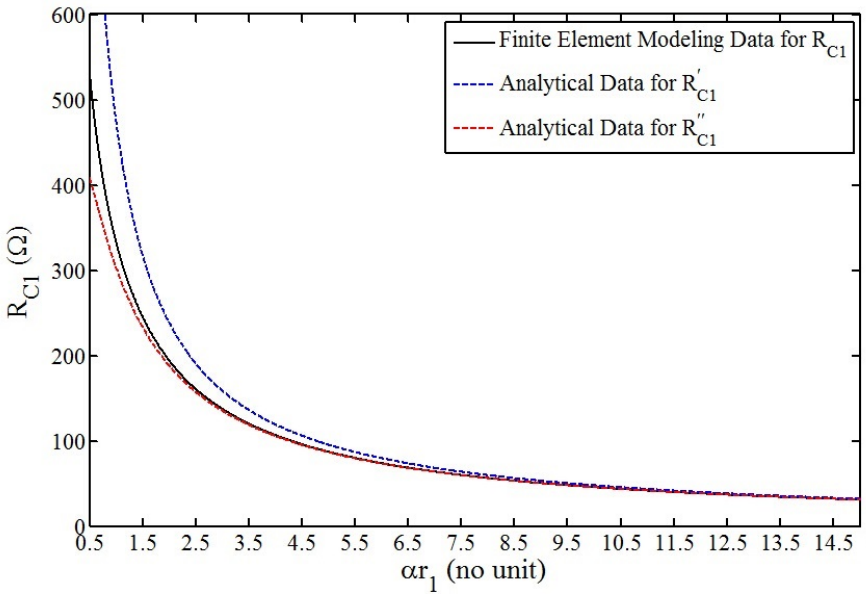

Figure B.2: Comparison of central dot electrode resistance R_{C1} with αr_1 ranging from 0.5 to 15. The analytical results using equations B.11 - B.13 and FEM data are presented. $R_{SH} = 3000\ \Omega/\square$, $\rho_c = 1 \times 10^{-4}\ \Omega \cdot cm^2$, r_0 is from 1 μm to 15 μm, $r_1/r_0 = 1.5$ and $r_1^{'}/r_0 = 10$.

Comparison of results from equations B.11, B.13 and FEM models for the outer contact resistance R_{C1} is shown in Fig. B.2. It shows that equation B.11 is acceptable only when αr_1 is much greater than 10. As expected, equation B.13 matches the FEM result more closely than equation B.11 and is useful for $\alpha r_1 \geq 2$.

Again considering the FEM results as giving the exact value of R_{C1}, the average error of equations B.11 and B.13 when αr_1 is less than 15 are 21.85% and 3.79% respectively. It can be seen that equation B.13 is more appropriate for the two contact circular test structure than equation B.11.

It can be seen from Fig. B.1 and Fig. B.2 that for the central dot contact equation B.5 is the most appropriate; for the outer electrode contact resistance equation B.13 is more appropriate than equation B.11. Considering the maximum number (three) of terms used here for the relevant contributing resistances, the most accurate equation for the total resistance R_T can be written as

$$R_T = R_{C0}^{'''} + R_P + R_{C1}^{''} \tag{B.14}$$

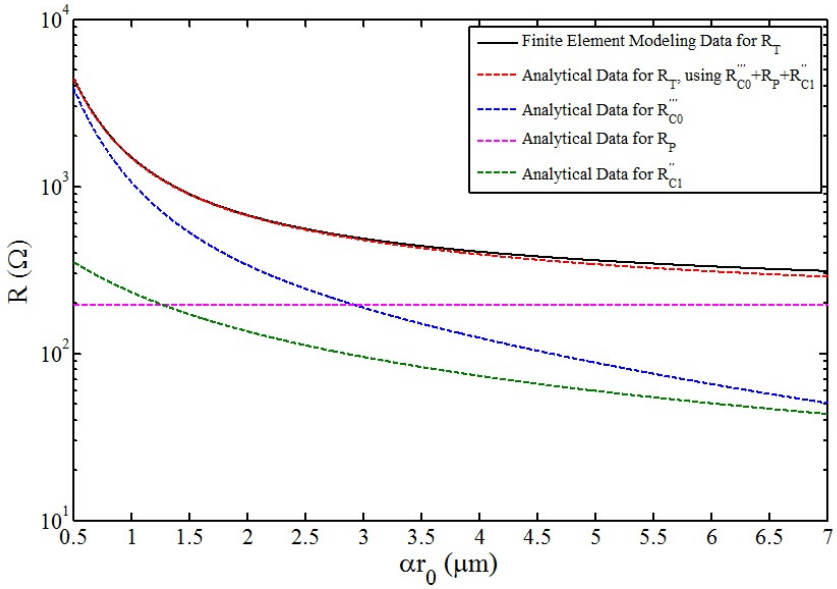

Figure B.3: Comparison of central dot contact $R_{C0}^{'''}$, parasitic contact R_P, outer contact resistance $R_{C1}^{''}$ and total resistance R_T with αr_0 ranging from zero to nine. The analytical results using equations B.5, 3.5, B.13, B.14 and FEM data of R_T are presented. $R_{SH} = 3000\ \Omega/\square$, $\rho_c = 1 \times 10^{-4}\ \Omega \cdot cm^2$, r_0 is from 1 μm to 15 μm, $r_1/r_0 = 1.5$, and $r_1^{'}/r_0 = 10$.

In Fig. B.3, a comparison of the analytical results of the three components of R_T using equation B.14 is presented. From the figure it can be seen that the analytical and FEM results have good agreement with increasing r_0. There is a turning region when αr_0 is about 2 to 4 for the curves of R_T. As described above, beyond this region, R_T does not change much and is very close to the parasitic

resistance R_P. In other words, R_P dominates the total resistance R_T completely when $r_1/r_0 = 1.5$ and αr_0 is greater than 4. In this situation, it is difficult to extract ρ_c accurately.

In order to avoid this undesirable situation for the given geometry, αr_0 should be less than 4, which is also a constraint in this example. However, the constraint of αr_0 is different when the ratio of r_1/r_0 is different (discussed later).

Again considering the FEM result as giving the exact value of the total resistance R_T, the average error of equation B.14 when $\alpha r_0 < 4$ is 1.49%, which is acceptable for extracting ρ_c.

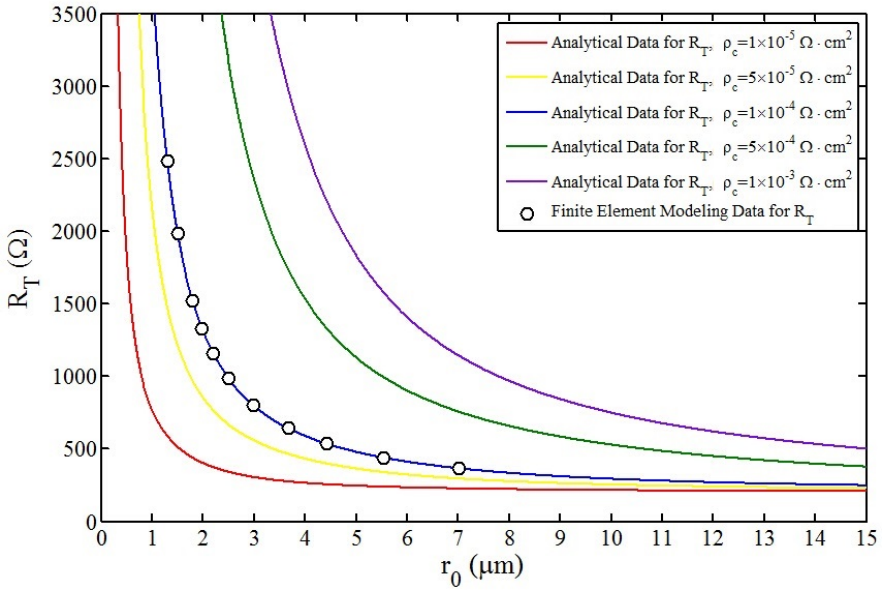

Figure B.4: Plots of the total resistance R_T versus the radius of the central dot r_0. R_T values are given using equation B.14 for different values of ρ_c. $R_{SH} = 3000\ \Omega/\square$, r_0 is from 1 μm to 15 μm, $r_1/r_0 = 1.5$ (here FEM data emulates experimental data).

Fig. B.4 shows the results for R_T from application of the two contact circular test structure for determining ρ_c in this example.

Plotting the R_T values obtained in the experiment (here FEM data emulates experimental data) and the analytical equation for R_T (here using equation B.14) with different ρ_c values in Fig. B.4 will accurately give the actual ρ_c. From the figure it can be seen that the FEM data fits the curve of $\rho_c = 1 \times 10^{-4}\ \Omega \cdot cm^2$ rather than other curves. What is meant by this is that the data belongs to the curve of $\rho_c = 1 \times 10^{-4}\ \Omega \cdot cm^2$ and then we can confidently say that the ρ_c values extracted from the FEM data are accurate and close to the actual ρ_c values.

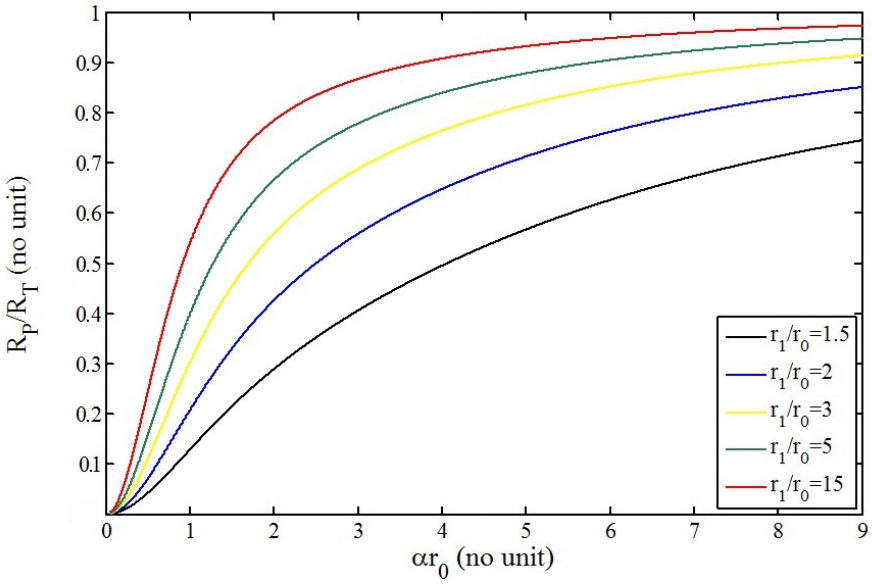

Figure B.5: Plots of the ratio R_P/R_T versus αr_0. Results for $r_1/r_0 = 1.5$, 2, 3, 5 and 15 are presented.

In order to extract an accurate ρ_c from the total resistance R_T, the effect of parasitic resistance needs to be minimized. Hence, only a small contribution of R_P is desired as R_P gives no information on ρ_c.

Equation B.14 is used as an example to obtain the contributions of R_{C0}, R_P and R_{C1} in the total resistance R_T. As shown in Fig. B.5, there are two factors that affect the contribution of R_P: r_1/r_0 and αr_0. In order to minimize the effect of parasitic resistance R_P, r_1/r_0 and αr_0 should be as small as possible.

From Fig. B.5 it can be seen that it is acceptable that R_P is less than 50% of R_T. In this case, for $r_1/r_0 = 1.5$, which is used in the example, αr_0 should be less than about 4. It is the same value that observed in Fig. B.3. For $r_1/r_0 = 2$ and 3, αr_0 should be less than about 2.5 and 1.5 respectively. Thus, αr_0 should be reduced to maintain an acceptable contribution of R_P when r_1/r_0 is increasing.

It is clearly seen that when $\alpha r_0 > 4$ or the ratio r_1/r_0 is large, R_P will dominate the total resistance R_T. This shows that it is possible to control the contribution of parasitic resistance to the total resistance by selecting the appropriate geometry.

B.2 Summary

The analytical equations of the two-contact circular test structure for the 2-D circumstance were analysed and reduced by considering the effect of using only the first term, the first two terms and the first three terms of the asymptotic forms of the Bessel functions. FEM has been used to demonstrate the accuracy of the reduced analytical expressions for the two-contact circular test structure by using an ohmic contact example with the values of a semiconductor sheet resistance (R_{SH}) and specific contact resistivity (ρ_c) of 3000 $\Omega/\square$ and 1×10^{-4} $\Omega \cdot cm^2$ respectively. Results showed that, for appropriate geometry, these reduced analytical expressions can be used to extract ρ_c conveniently and accurately using the two-contact circular test structure.

The contributions of R_{C0}, R_P and R_{C1} to the total resistance R_T with various ratios of r_1/r_0 were also presented. Results showed that, the contribution of R_P, which has no information on ρ_c, to the total resistance R_T has to be minimized by reducing the geometries or the ratio of r_1/r_0 to increase the accuracy when extracting ρ_c using the analytical expressions.

Appendix C

Proposed Fabrication Schedule for The Two-Contact Circular Test Structure −− A Two-Layer Metal Electrode Design for Extremely Small Contacts

For some ohmic contacts such as Ni to very heavily doped Si (with a doping concentration $> 10^{20}\ cm^{-3}$) contacts, the value of ρ_c can be extremely low. Furthermore, heat treatment can improve ohmic contacts and reduce ρ_c by several magnitudes. Therefore, when using the two-contact circular test structure in these situations, the total resistance R_T between the two electrodes will be unmeasurable or too small that the measurement error will have a significant effect on it. Reducing the pattern size can increase the resistance to solve this problem. However, it is challenging to probe on a small pattern (e.g. a dot with a radius of 3 μm or less) using micro-manipulators.

To solve this probing problem, a two-layer metal contact design for small contacts using the two-contact circular test structure is presented. A schematic of the cross-section of this structure is shown in Fig. C.1. It can be seen from the figure that the contact areas have been extended by using two metal layers.

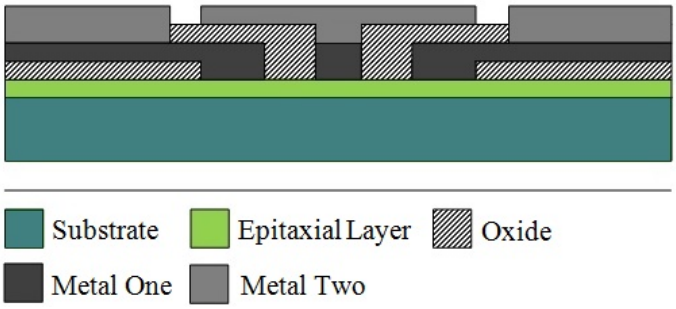

Figure C.1: Schematic of the cross-section of the fabricated two-contact circular test structure for the 2-D circumstance using a two-layer metal electrode design. The extended metal electrodes can be used for probing when the actual contacts are extremely small and difficult for probing.

A mask set comprising of four masks is design for this structure shown in Fig. C.2 and Fig. C.3 is a flow chart for demonstrating the fabrication process using the given masks and positive photoresist (both cross-section and top view of the sample are presented). An oxide layer is put on the epitaxial layer, mask one is then used for etching the oxide to create the initial contact windows. Metal one is evaporated on the surface of the sample and mask two is used to isolate the central dot contact. A second oxide layer is then put on the sample followed by wet etching using mask three to create the openings for metal two. Finally metal two is evaporated on the surface of the sample and mask four is used to separate the central contact and outer contact.

Note that the same mask set and fabrication process can be applied to the contacts in 3-D situations (e.g. contacts to bulk substrates, thick epitaxial layers and so on).

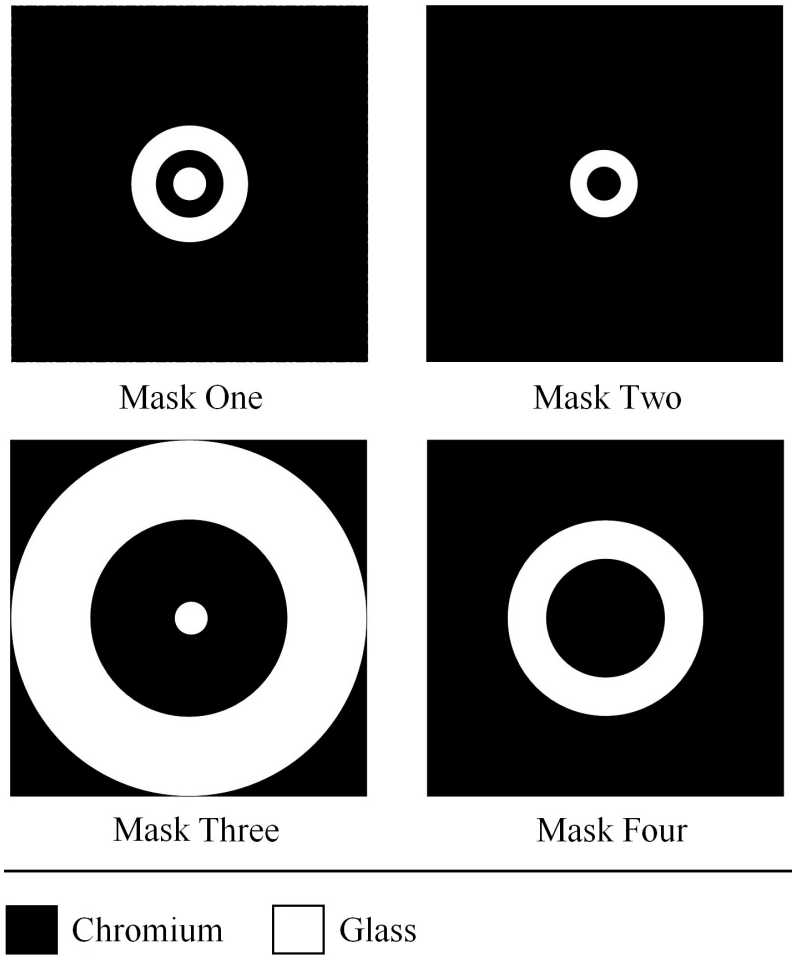

Figure C.2: Mask design for the two-contact test structure for contacts to 2-D semiconductor layers for the wet etching technique. The black regions are the chromium on the mask and the white regions are the glass which are transparent. Mask one is used to etch the first oxide layer, mask two is used to etch the fist metal layer, mask three and mask four are used two etch the second oxide layer and metal two respectively.

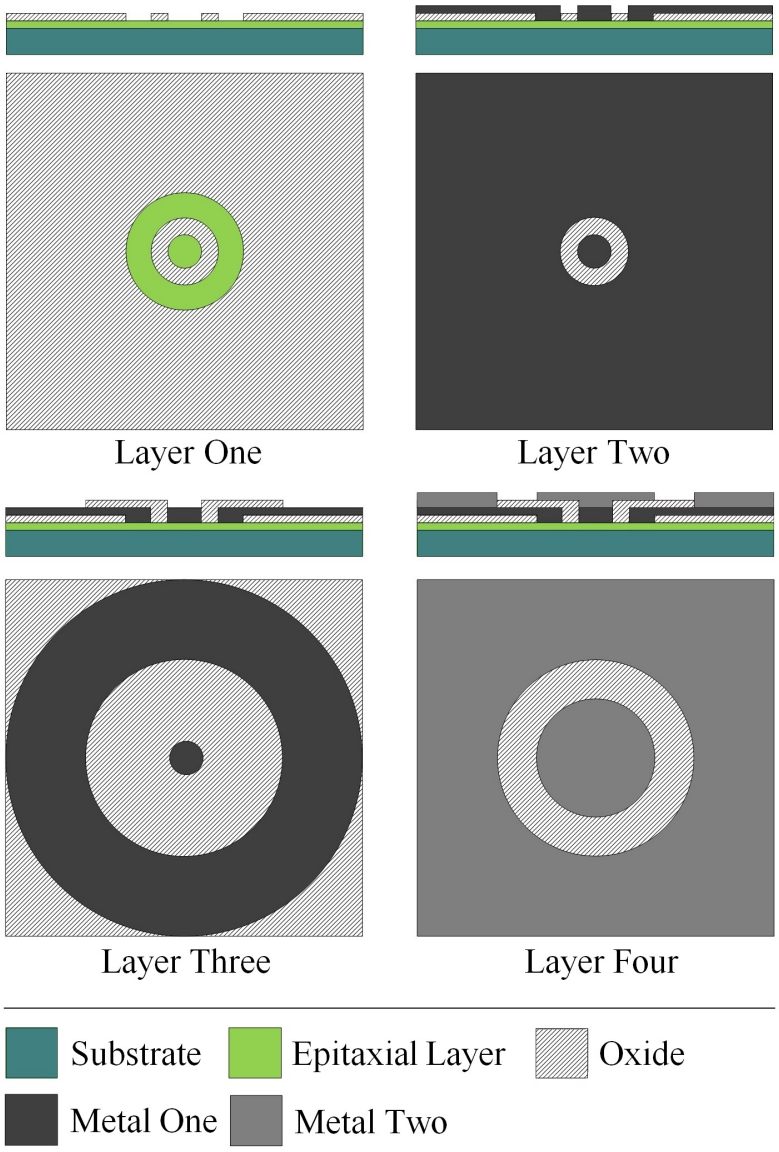

Figure C.3: Schematics of both the cross-section and top view of the fabricated two-contact circular test structure with extended metal contacts. Layer one to layer four are fabricated in sequence using mask one to mask four presented in Fig. C.2 using the wet etching technique.

Appendix D

Experimental Data for Au/Ni/Ti to Ion Implanted 3C-SiC Ohmic Contacts

The experimental data for R_{SH} and ρ_c using the two-contact circular test structure for as-deposited Au/Ni/Ti to unimplanted 3C-SiC and ion implanted 3C-SiC with either C or P ions at doses of 1×10^{13}, 1×10^{14} and 1×10^{15} $ions/cm^2$ are shown in Table D.1 and Table D.2. Note that these data are used to generate Fig. 6.9 and Fig. 6.10.

Table D.1: Experimental results for R_{SH} and ρ_c using the two-contact circular test structure for as-deposited Au/Ni/Ti to unimplanted 3C-SiC and ion implanted 3C-SiC with C ions at doses of 1×10^{13}, 1×10^{14} and 1×10^{15} $ions/cm^2$. The Au, Ni and Ti layers have thicknesses of 50 μm for each of them. The very heavily doped n-type 3C-SiC epitaxial layer has a thickness of 1.1 μm and the thickness of the p-type Si substrate is 300 μm. The radius of the central dot contact r_{01} varies from 6 μm to 12 μm. $r_{02}/r_{01} = 1.5$ and $r_{03}/r_{01} = 3.5$ (see Fig. 3.9).

Pattern	Dose Type	R_{SH} ($\Omega/\square$)	ρ_c ($\Omega \cdot cm^2$)
1	Un[1]	27.3	1.4×10^{-6}
2	Un[1]	27.2	1.3×10^{-6}
3	Un[1]	28.4	1.0×10^{-6}
4	Un[1]	23.7	2.1×10^{-6}
5	Un[1]	27.0	8.4×10^{-7}
6	Un[1]	25.2	1.1×10^{-6}
7	C13[2]	26.8	7.2×10^{-6}
8	C13[2]	28.6	1.1×10^{-6}
9	C13[2]	30.5	2.0×10^{-6}
10	C13[2]	26.3	1.1×10^{-6}
11	C13[2]	30.1	1.2×10^{-6}
12	C14[3]	29.1	2.5×10^{-6}
13	C14[3]	29.5	2.3×10^{-6}
14	C14[3]	31.1	2.0×10^{-6}
15	C14[3]	29.1	3.9×10^{-6}
16	C14[3]	33.3	3.6×10^{-7}
17	C14[3]	31.0	2.6×10^{-6}
18	C14[3]	33.2	2.7×10^{-6}
19	C14[3]	35.4	1.3×10^{-6}
20	C15[4]	34.2	1.9×10^{-4}
21	C15[4]	33.0	1.9×10^{-4}
22	C15[4]	30.0	1.9×10^{-4}
23	C15[4]	42.3	1.8×10^{-4}
24	C15[4]	37.3	1.9×10^{-4}
25	C15[4]	36.0	1.9×10^{-4}
26	C15[4]	34.2	1.8×10^{-4}

[1] Au/Ni/Ti contacts on unimplanted 3C-SiC.
[2] Au/Ni/Ti contacts on ion implanted 3C-SiC with C ions at dose of 1×10^{13} $ions/cm^2$.
[3] Au/Ni/Ti contacts on ion implanted 3C-SiC with C ions at dose of 1×10^{14} $ions/cm^2$.
[4] Au/Ni/Ti contacts on ion implanted 3C-SiC with C ions at dose of 1×10^{15} $ions/cm^2$.

Table D.2: Experimental results for R_{SH} and ρ_c using the two-contact circular test structure for as-deposited Au/Ni/Ti to ion implanted 3C-SiC with P ions at doses of 1×10^{13}, 1×10^{14} and 1×10^{15} $ions/cm^2$. The Au, Ni and Ti layers have thicknesses of 50 μm for each of them. The very heavily doped n-type 3C-SiC epitaxial layer has a thickness of 1.1 μm and the thickness of the p-type Si substrate is 300 μm. The radius of the central dot contact r_{01} varies from 6 μm to 12 μm. $r_{02}/r_{01} = 1.5$ and $r_{03}/r_{01} = 3.5$ (see Fig. 3.9).

Pattern	Dose Type	R_{SH} ($\Omega/\square$)	ρ_c ($\Omega \cdot cm^2$)
1	P13[1]	28.1	1.5×10^{-6}
2	P13[1]	26.0	2.5×10^{-6}
3	P13[1]	27.5	1.2×10^{-6}
4	P13[1]	28.1	2.7×10^{-6}
5	P13[1]	25.8	4.2×10^{-6}
6	P13[1]	24.0	6.4×10^{-6}
7	P14[2]	29.8	1.3×10^{-6}
8	P14[2]	29.3	3.9×10^{-6}
9	P14[2]	23.9	3.2×10^{-6}
10	P14[2]	28.0	2.1×10^{-6}
11	P14[2]	31.1	7.0×10^{-7}
12	P14[2]	28.8	2.6×10^{-6}
13	P14[2]	22.3	5.9×10^{-6}
14	P15[3]	35.0	4.6×10^{-5}
15	P15[3]	37.4	3.4×10^{-5}
16	P15[3]	31.9	4.1×10^{-5}
17	P15[3]	29.4	4.2×10^{-5}

[1] Au/Ni/Ti contacts on ion implanted 3C-SiC with P ions at dose of 1×10^{13} $ions/cm^2$.
[2] Au/Ni/Ti contacts on ion implanted 3C-SiC with P ions at dose of 1×10^{14} $ions/cm^2$.
[3] Au/Ni/Ti contacts on ion implanted 3C-SiC with P ions at dose of 1×10^{15} $ions/cm^2$.

Appendix E

Proposed New Test Structure −− Combined TLM-CTLM Test Structure for Determining Specific Contact Resistivity of Contacts to 2-D Semiconductor Layers

A novel test structure, which is a combination of the circular transmission line model (CTLM) and the transmission line model (TLM), is presented. It has the same simple analytical equations to determine ρ_c as TLM but eliminates the necessity of mesa isolation using the CTLM portion which simplifies the fabrication. In addition, there are no correction factor for this test structure.

E.1 The Combined TLM-CTLM Model

The model consists of two half-CTLM patterns and a TLM pattern between them. As shown in Fig. E.1, the width and the length of the central TLM rectangle contact are W and $2L$ respectively. The length of the TLM rectangular contacts for the outer contact is L. The gap between the central contact and the outer electrode is d.

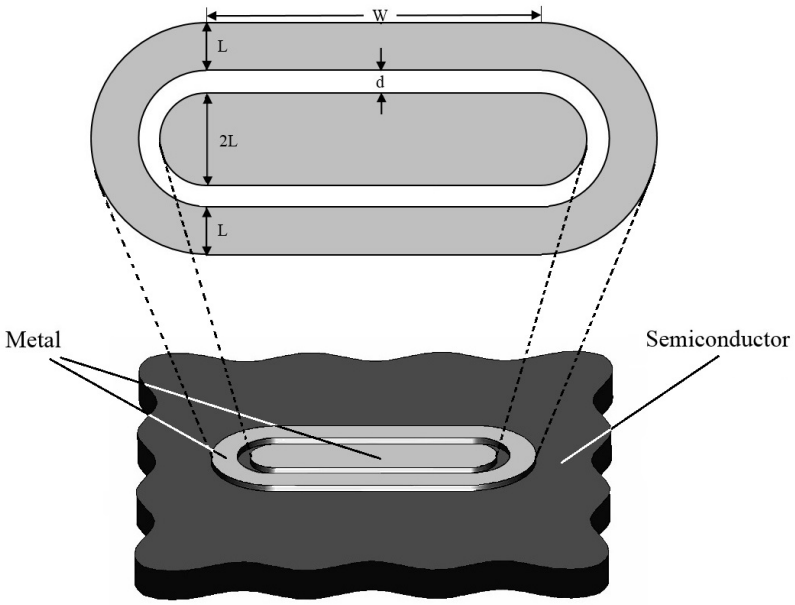

Figure E.1: Isometric view of the combined TLM-CTLM test structure. Total resistance R_T is measured between the central electrode and the outer electrode.

When current is injected into the central electrode and flows out from the outer electrode, the total resistance R_T between the central and the outer electrodes can be determined by measuring the voltage between the electrodes

$$R_T = \frac{V}{I} \tag{E.1}$$

Fig. E.2 shows the resistance representation of the model in Fig. E.1. R_T consists

of the resistance R_A due to the CTLM part and the resistance R_B due to the TLM part which is the middle part of the proposed test structure. Since R_A and R_B are in parallel, R_T can be written as

$$R_T = \frac{1}{\frac{1}{2R_A} + \frac{1}{R_B} + \frac{1}{2R_A}} = \frac{R_A \cdot R_B}{R_A + R_B} \tag{E.2}$$

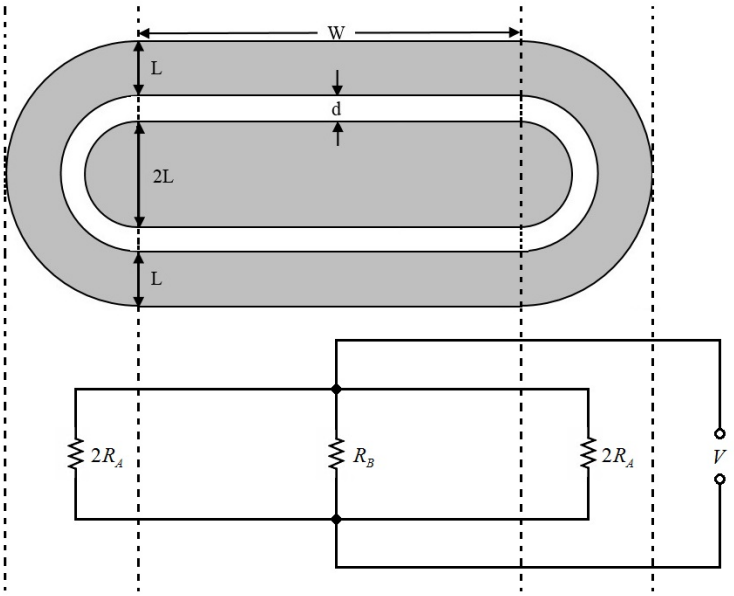

Figure E.2: Schematic of the combined TLM-CTLM test structure. Total resistance R_T consists of R_A and R_B.

The components of the analytical model for R_T are determined as follows.

A. Resistance R_A Due to The CTLM Portion

The two half-CTLM patterns can be considered as a whole CTLM test structure. As reported in previous work [Pan et al., 2013], R_A consists of the central dot contact resistance R_{C0}, the resistance due to the semiconductor ring R_P and the outer electrode resistance R_{C1}

$$R_A = R_{C0} + R_P + R_{C1} \tag{E.3}$$

B. Resistance R_B Due to The TLM Portion

The resistance due to the TLM portion in the middle of the proposed test structure can be considered as two equal resistances which are the total resistances between two rectangular electrodes with the same size $(L \times W)$ in parallel

$$R_B = \frac{1}{2}(\frac{R_{SH} \cdot d}{W} + 2R_C) \tag{E.4}$$

where R_C is the contact resistance under each rectangular electrode

$$R_C = \frac{\sqrt{R_{SH} \cdot \rho_c}}{W} \coth(L/L_T) \tag{E.5}$$

L_T is the transfer length, which is defined as

$$L_T = \sqrt{\frac{\rho_c}{R_{SH}}} \tag{E.6}$$

when L_T is shorter than $0.5L$, $\coth(L/L_T) \to 1$, hence, equation E.4 can be reduced to

$$R_B = \frac{R_{SH}}{2W}(d + 2L_T) \tag{E.7}$$

E.2 Modeling of The Combined TLM-CTLM Test Structure

FEM is used again to accurately model the electrical behavior of the proposed test structure. Forming a model requires information on contact structure geometry, conductivity of each layer in the structure, and specific contact resistivity (ρ_c) of each interface in the structure.

A combined TLM-CTLM test structure with L, d and W values of 50 μm, 25 μm and 300 μm respectively, is used as an example to compare the analytical equations to those obtained by FEM. Each metal contact is assumed to be an equipotential, and this implies zero sheet resistance for the metal layer. The thickness of the semiconductor layer was 0.3 μm. In order to reduce the time taken for analysis, only a quarter of the whole structure is modeled. Examining the symmetry in the structure shows that this is representative of the whole structure.

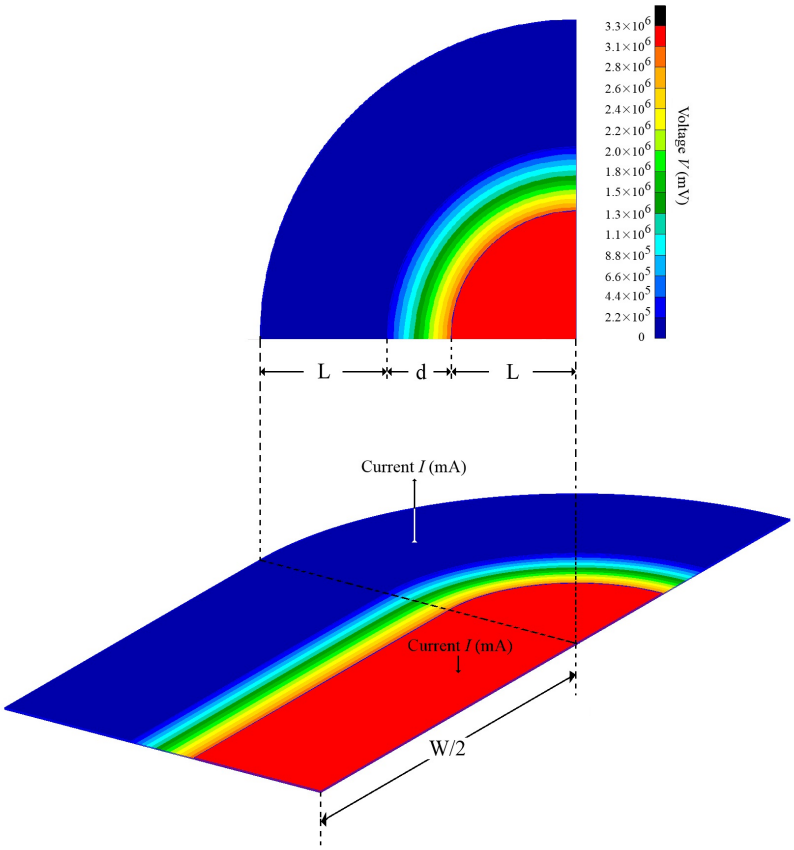

Figure E.3: Equipotentials (in millivolts) in the semiconductor layer for the combined TLM-CTLM test structure FEM example where $L = 50$ μm, $d = 25$ μm and $W = 300$ μm. $R_{SH} = 3000$ $\Omega/\square$, $\rho_c = 1 \times 10^{-4}$ $\Omega \cdot cm^2$ (a quarter of the test structure is presented).

The equipotential of the outer electrode surface is set to zero, and the current is input at the central electrode. Fig. E.3 shows the equipotentials and structure geometry of an example model.

Modeling of the CTLM has been reported in previous work [Pan et al., 2013] and modeling of the TLM shows that there is a perfect agreement between the analytical equations and FEM results.

R_T from the FEM is obtained by determining the difference between the equipotential of the central electrode and the equipotential of the outer electrode. R_T from the FEM is then determined by dividing this potential difference by the input current.

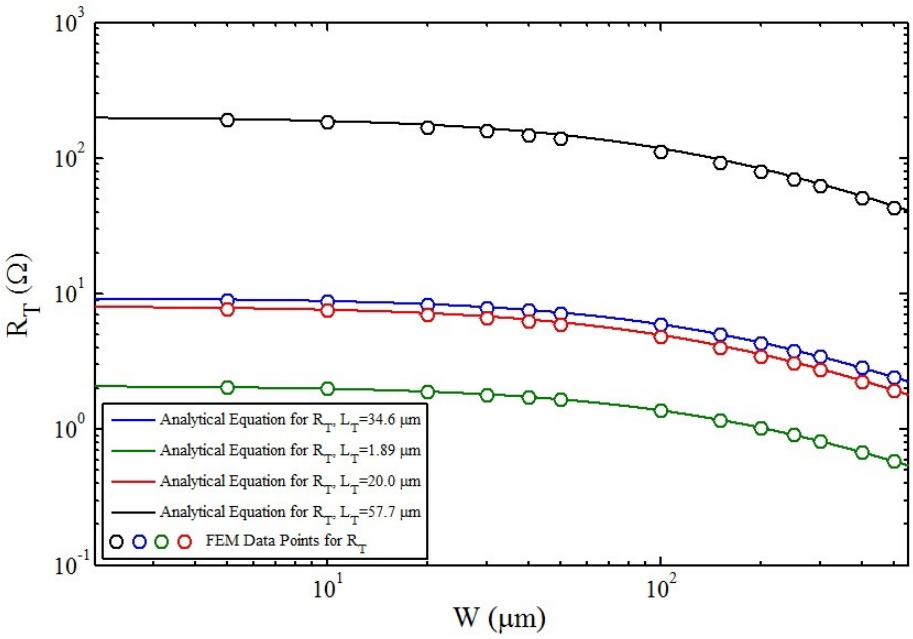

Figure E.4: Comparison of the total resistance R_T with W ranging from 5 to 500 μm. $L = 50\ \mu m$, $d = 25\ \mu m$. The values of L_T are 1.89 μm, 20.0 μm, 34.6 μm and 57.7 μm respectively.

Fig. E.4 shows a comparison of the FEM and analytical results using equation

E.2 for R_T. It is seen that the analytical and FEM results are in good agreement with increasing W for different values of L_T.

E.3 Methodology to Extract Specific Contact Resistivity Using The Combined TLM-CTLM Test Structure

The complete test pattern to extract ρ_c is shown in Fig. E.5. The structure consists of four combined TLM-CTLM patterns with different values of d and W.

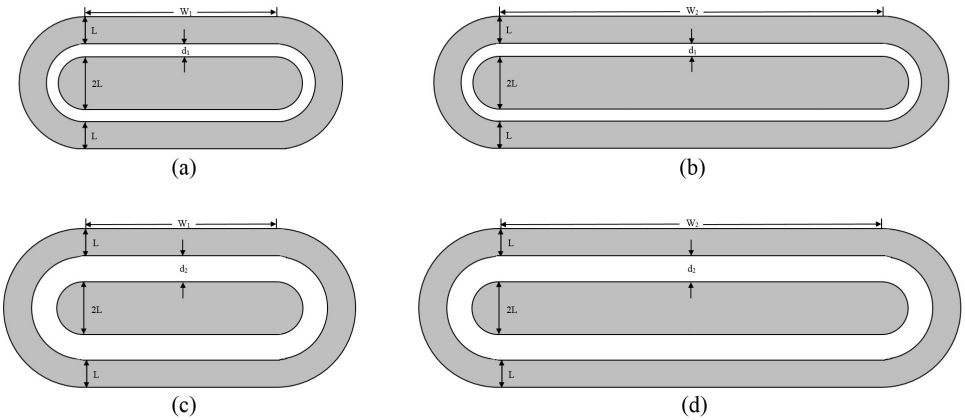

Figure E.5: Structure used to extract R_{SH} and ρ_c using the combined TLM-CTLM test structure.

Considering the resistances between the central electrode and the outer electrode for each of the contact structures in Fig. E.5 (a) and (b), we have

$$\frac{1}{R_{T1}} = \frac{1}{R_{A1}} + \frac{1}{R_{B1}} \tag{E.8}$$

$$\frac{1}{R_{T2}} = \frac{1}{R_{A1}} + \frac{1}{R_{B2}} \tag{E.9}$$

Substituting equations E.4 and E.5 to equations E.8 and E.9

$$\frac{1}{R_{T1}} - \frac{1}{R_{T2}} = \frac{1}{R_{B1}} - \frac{1}{R_{B2}} = \frac{2\,(W_1 - W_2)}{R_{SH}\,[d_1 + 2L_T \cdot \coth\,(L/L_T)]} \tag{E.10}$$

Similarly, considering the resistances between the two electrodes for the contact patterns in Fig. E.5 (c) and (d)

$$\frac{1}{R'_{T1}} = \frac{1}{R'_{A1}} + \frac{1}{R'_{B1}} \tag{E.11}$$

$$\frac{1}{R'_{T2}} = \frac{1}{R'_{A1}} + \frac{1}{R'_{B2}} \tag{E.12}$$

Using equations E.4 and E.5

$$\frac{1}{R'_{T1}} - \frac{1}{R'_{T2}} = \frac{1}{R'_{B1}} - \frac{1}{R'_{B2}} = \frac{2\,(W_1 - W_2)}{R_{SH}\,[d_2 + 2L_T \cdot \coth\,(L/L_T)]} \tag{E.13}$$

R_{SH} can be determined by eliminating L_T in equations E.10 and E.13

$$R_{SH} = \frac{d_2 - d_1}{2\,(W_2 - W_1)} \cdot \theta \tag{E.14}$$

where θ can be experimental determined

$$\theta = \frac{(R_{T2} - R_{T1}) \cdot (R'_{T2} - R'_{T1})}{R_{T1}R_{T2} \cdot (R'_{T2} - R'_{T1}) - R'_{T1}R'_{T2} \cdot (R_{T2} - R_{T1})} \tag{E.15}$$

Eliminating R_{SH} in equations E.10 and E.13, L_T can be found

$$\frac{d_2 + 2L_T \cdot \coth(L/L_T)}{d_1 + 2L_T \cdot \coth(L/L_T)} = \frac{R_{T2} - R_{T1}}{R_{T1} \cdot R_{T2}} \cdot \frac{R'_{T1} \cdot R'_{T2}}{R'_{T2} - R'_{T1}} \tag{E.16}$$

If L is greater than $2L_T$, equation E.16 can be reduced to

$$L_T = \frac{d_2 - \varphi \cdot d_1}{2\varphi - 2} \tag{E.17}$$

where φ can be also experimental determined

$$\varphi = \frac{R_{T2} - R_{T1}}{R_{T1} \cdot R_{T2}} \cdot \frac{R'_{T1} \cdot R'_{T2}}{R'_{T2} - R'_{T1}} \tag{E.18}$$

With known R_{SH} and L_T, ρ_c can be found immediately using equation E.6.

For the proposed test structure presented here, L, d, W, R_{SH} and ρ_c determine the total resistance R_T. Results show that analytical equations can be used to determine ρ_c if R_T is measured and ρ_c and R_{SH} are the only unknowns. In order to verify that the structure is universal, R_{SH} and ρ_c are scaled by factors m and n, respectively. By using equations E.2-E.6, the total resistance can be written in the following form:

$$R_T\left(mR_{SH}, n\rho_c, \frac{\sqrt{n}}{\sqrt{m}}L, \frac{\sqrt{n}}{\sqrt{m}}d, \frac{\sqrt{n}}{\sqrt{m}}W\right) = mR_T\left(R_{SH}, \rho_c, L, d, W\right) \tag{E.19}$$

Equation E.19 shows that scaling R_{SH} and ρ_c will not change the shape of the plots in Fig E.4 with the y-axis scaled by a factor of m. Thus, the structure is universal and applicable for ohmic contacts where the resistive effects of the semiconductor layer and the contact interface can be described by R_{SH} and ρ_c respectively.

E.4 Summary

A new test structure, using a combination of the TLM and the CTLM, was presented. This structure and the corresponding ρ_c evaluation technique are appropriate for the contacts to 2-D semiconductor layers. FEM has been used to

demonstrate the accuracy of the proposed test structure. The given scaling equation showed that this test structure is universal using equation E.19.

List of Publications

1. **Y. Pan**, G. K. Reeves. P. W. Leech, and A. S. Holland. Analytical and finite-element modeling of a two-contact circular test structure for determining specific contact resistivity. *IEEE Trans. Electron Devices*, 60(3):1202-1207, 2013.

2. A. M. Collins, **Y. Pan**, and A. S. Holland. Using a two-contact circular test structure to determine the specific contact resistivity of contacts to bulk semiconductors. *Facta Universitatis, Series: Electronics and Energetics*, 28(3):457-464, 2015.

3. **Y. Pan**, G. K. Reeves, P. W. Leech, P. Tanner, and A. S. Holland. Two-contact Circular Test Structure for Determining Specific Contact Resistivity. *MRS Proceedings*, 1553(864):mrss13-1553-t03-13, 2013.

4. P. W. Leech, A. S. Holland, G. K. Reeves, **Y. Pan**, M. Ridgway, and P. Tanner. Effect of low energy implantation on the properties of Ti/Ni/Au contacts to n-SiC. *MRS Proceedings*, 1743(284):mrsf14-1743-ww12-10, 2015.

5. **Y. Pan**, A. M. Collins, P. W. Leech, G. K. Reeves, A. S. Holland, and P. Tanner. Low specific contact resistivity nickel to silicon carbide determined using a two contact circular test structure. *Proc. IEEE Int. Conf. Microelectron. Test Struct.*, 79-82, 2014.

6. A. M. Collins, **Y. Pan**, and A. S. Holland. Designing geometry for the circular transmission line model to determine sheet resistance under contacts. *Proc. IEEE Int. Conf. Microelectronics*, 311-314, 2014.

7. **Y. Pan**, A. M. Collins, and A. S. Holland. Determining specific contact resistivity of contacts to bulk semiconductor using a two-contact circular test structure. *Proc. IEEE Int. Conf. Microelectronics*, 257-260, 2014.

8. **Y. Pan**, A. M. Collins, and A. S. Holland. A novel single dot test structure for determining specific contact resistivity. *Proc. of SPIE*, 8923:89232Q-1-89232Q-11, 2013.

9. **Y. Pan**, A. M. Collins, F. Algahtani, P. W. Leech, G. K. Reeves, P. Tanner, and A. S. Holland. Investigating extremely low resistance ohmic contacts to silicon carbide using a novel test structure. *Proc. of SPIE*, 8923:892356-1-892356-5, 2013.

10. A. M. Collins, **Y. Pan**, and A. S. Holland. Improved geometrical design of the circular transmission line model ohmic contact test structure. *Proc. of SPIE*, 8923:892359-1-892359-6, 2013.

References

D. Alok, B. J. Baliga, and P. K. McLarty. Low contact resistivity ohmic contacts to 6H-silicon carbide. *Electron Devices Meeting*, 93:691–694, 1993. 80

H. H. Berger. Contact resistance on diffused resistors. *proc. IEEE International Solid-State Circuits Conference*, 4:160–161, 1969. 11, 44

H. H. Berger. Models for contacts to planar devices. *Solid-State Electronics*, 15: 145–158, 1972. 11, 13, 42, 43

F. Braun. Uber die stromleitung durch schwefelmetalle. *Ann. Phy. Chem.*, 153: 556, 1874. iv, 1

C. Y. Chang, Y. K. Fang, and S. M. Sze. Specific contact resistance of metal-semiconductor barriers. *Solid-State Electronics*, 14:541–550, 1971. iv, 5

I. F. Chang. Contact resistance in diffused resistors. *J. Electrochem. Soc.*, 117: 368–373, 1970. 13

S. C. Chang, S. J. Wang, K. M. Uang, and B. W. Liou. Investigation of Au/Ti/Al ohmic contact to n-type 4H–SiC. *Solid-State Electronics*, 49:1937–1941, 2005. 70, 80

L. Chunjuan, L. Su, F. Jingjing, and W. Rong. Nickel ohmic contacts of high-concentration P-implanted 4H-SiC. *Journal of Semiconductors*, 33(3): 036002.1–036002.4, 2012. 84

S. S. Cohen, G. Gildenblat, M. Ghezzo, and D. M. Brown. Al-0.9%Si/Si ohmic contacts to shallow junctions. *J. Electrochem. Soc.*, 129:1335–1338, 1982. 20

United States Department Commerce. *Handbook of Mathematical Functions with Formulas, Graphs, and Mathematical Tables*. Dover, NY USA, 1972. 16, 27

Z. C. Feng. *SiC Power Materials: Devices and Applications*. Springer, Germany, 2004. 79

M. Finetti, A. Scorzoni, and G. Soncini. Lateral current crowding effects on contact resistance measurements in four terminal resistor test patterns. *IEEE Electron Dev. Lett.*, 5:524–526, 1984. 22

M. Grodzicki, J. Chrzanowski, P. Mazur, S. Zuber, and A. Ciszewski. Cr ohmic contact on an Ar^+ ion modified 6H-SiC (0001) surface. *Optica Applicata*, 39 (4):765–772, 2009. 79

C. A. Hewett, M. J. Taylor, J. R. Zeidler, and M. W. Geis. Specific contact resistance measurements of ohmic contacts to semiconducting diamond. *J. Appl. Phys.*, 77(2):755–760, 1995. 19

A. S. Holland, G. K. Reeves, and H. B. Harrison. Error correction for finite semiconductor resistivity in kelvin test structures. *proc. IEEE Int. Conference on Microelectronic Test Structures*, 10:95–98, 1997. 37

A. S. Holland, G. K. Reeves, and P.W. Leech. Universal error corrections for finite semiconductor resistivity in cross-kelvin resistor test structures. *IEEE Trans. Electron Devices*, 51:914–919, 2004. 23, 45

A. S. Holland, G. K. Reeves, M. Bhaskaran, and S. Sriram. Analytical and finite-element modeling of a cross kelvin resistor test structure for low specific contact resistivity. *IEEE Trans. Electron Devices*, 56(10):2250–2254, 2009. 28, 48

G. Hui, Z. Yi-Men, and Z. Yu-Ming. Ti–Al based ohmic contacts to n-type 6H-SiC with P^+ ion implantation. *Chinese Physics*, 15(9):2142–2145, 2006. 79

W. Kellner. Planar ohmic contacts to N-Type GaAs: Determination of contact parameters using the transmission line model. *Siemens Forsch. Entwicklungsber*, 4(3):137–140, 1975. 15

R. R. Lieten, S. Degroote, M. Kuijk, and G. Borghs. Ohmic contact formation on n-type Ge. *Appl. Phys. Lett.*, 92:022106.1–022106.3, 2008. 79

F. Liu, C. H. Li, A. P. Pisano, C. Carraro, and R. Maboudian. Low-energy ion bombardment to tailor the interfacial and mechanical properties of polycrystalline 3C-silicon carbide. *J. Vac. Sci. Technol.*, 28:1259, 2010. 79

W. M. Loh, K. Saraswat, and R. W. Dutton. Analysis and scaling of kelvin resistors for extraction of specific contact resistivity. *IEEE Electron Device Lett.*, 6(3):105–108, 1985. 38, 50

W. M. Loh, S. E. Swirhun, T. A. Schreyer, R. M. Swanson, and K. C. M. Saraswat. Modeling and measurement of contact resistances. *IEEE Trans. Electron Devices*, 34:512–524, 1987. 23, 43

G. S. Marlow and M. B. Das. The effects of contact size and non-zero metal resistance on the determination of specific contact resistance. *Solid-State Electronics*, 25(2):91–94, 1982. 100

J. A. Mazer, L. W. Linholm, and A. N. Saxena. An improved test structure and kelvin-measurement method for the determination of integrated circuit front contact resistance. *J. Electrochem. Soc.*, 132:440–443, 1985. 20

K. Mochizuki, A. Terano, M. Momose, A. Taike, M. Kawata, J. Gotoh, and S. Nakatsuka. Au/Pt/Ti/Ni ohmic contacts to p-ZnTe. *Electronics Letters*, 30 (23):1984–1985, 1994. 81

G. E. Moore. Cramming more components onto integrated circuits. *Electronics*, 38(8), 1965. 44

H. Murrmann and D. Widmann. Current crowding on metal contacts to planer devices. *proc. IEEE International Solid-State Circuits Conference*, 4:162–163, 1969. 10

N. F. M. Nasir, P. W. Leech, A. S. Holland, and P. Tanner. Properties of Al and Pd on n-type SiC membranes. *MRS Proc.*, page 1433, 2012. 29

T. Ohmi. Ultra-clean processing for ULSI. *J. Microelectron*, 26(6):595–619, 1995. 44

M. Ono, A. Nishiyama, and A. Toriumi. A simple approach to understanding errors in the cross-bridge kelvin resistor and a new pattern for measurements of specific contact resistivity. *Solid-State Electronics*, 46:1325–1331, 2002. 23

Y. Pan, G. K. Reeves, P. W. Leech, and A. S. Holland. Analytical and finite-element modeling of a two-contact circular test structure for specific contact resistivity. *IEEE Trans. Electron Devices*, 60(3):1202–1207, 2013. iv, 72, 80, 82, 116, 119

S. J. Proctor and L. W. Linholm. A direct measurement of interfacial contact resistance. *IEEE Electron Dev. Lett.*, 3:294–296, 1982. xi, 20, 21

G. K. Reeves. Specific contact resistance using a circular transmission line model. *Solid-State Electronics*, 23(5):487–490, 1980. iv, 14, 15, 18, 27, 28

G. K. Reeves and H. B. Harrison. Obtaining the specific contact resistance from transmission line model measurements. *IEEE Electron Device Lett.*, 3(5):111–113, 1982. 11

G. K. Reeves and H. B. Harrison. An analytical model for alloyed ohmic contacts using a trilayer transmission line model. *IEEE Trans. Electron Devices*, 42(8): 1536–1547, 1995. 44

E. H. Rhoderick. *Metal-Semiconductor Contacts*. Clarendon, Oxford, 1978. 1

V. L. Rideout. A review of the theory, technology and applications of metal-semiconductor rectifiers. *Thin Solid Films*, 48:261, 1978. 1

D. K. Schroder. *Semiconductor Material and Device Characterization, 3rd ed.* Wiley, Hoboken NJ USA, 2006. 5, 45

K. K. Shih and J. M. Blum. Contact resistances of Au-Ge-Ni, Au-Zn and Al to III–V compounds. *Solid-State Electronics*, 15:1177–1180, 1972. iv, 20

W. Shockley. Research and investigation of inverse epitaxial UHF power transistors. *Air Force Atomic Laboratory, Wright-Patterson Air Force Base*, Rep. No. AL-TDR-64-207, 1964. iv, 10

X. Song, J. Biscarrat, J-F. Michaud, F. Cayrel, M. Zielinksi, T. Chassagne, M. Portail, E. Collard, and D. Alquier. Structural and electrical characterizations of n-type implanted layers and ohmic contact on 3C-SiC. *Nucl. Instr. Meth. Phys. Res.*, 269:2020–2025, 2011. 84, 85

B. G. Streetman and S. K. Banerjee. *Solid state electronic devices, 6th Ed.* Pearson Prentice Hall, Upper Saddle River, NJ 07458, 2000. 3

S. M. Sze. *Physics of Semiconductor Devices, 2nd Ed.* Wiley-Interscience, New York, 1981. 1, 3

T. Takeda, A. Tomita, T. Matsui, and T. Isshiki. Structural analysis of ZnO thin films grown in room temperature on PET film. *Materials Science Forum*, 770-780:1201–1205, 2014. 84

C. Y. Ting and C. Y. Chen. A study of the contacts of a diffused resistor. *Solid-State Electronics*, 14:433–438, 1971. 13

L. B. Valdes. Effect of electrode spacing on the equivalent base resistance of point-contact transistors. *Proceedings of the IRE*, 40:1429–1434, 1952. 68, 85

L. J. VanderPauw. A method of measuring specific resistivity and hall effect of discs of arbitrary shape. *Philips Research Reports*, 13(1):1–9, 1958. 75

L. Wang, S. Dimitrijev, J. Han, F. Iocopi, and J. Zhou. Transition between amorphous and crystalline phases of SiC deposited on Si substrate using H3SiCH3. *Journal of Crystal Growth*, 311(19):4442–4446, 2009. 60

A. H. Wilson. The theory of electronic semiconductors. *Proc. R. Soc. Lond. Ser. A*, 133:458, 1931. 1

A.Y.C. Yu. Electron tunneling and contact resistance of metal-silicon contact barriers. *Solid-State Electronics*, 13:239–247, 1970. 2

Y. Zhong, C. Bailat, R. S. Averback, S. K. Ghose, and I. K. Robinson. Damage accumulation in Si during high-dose self-ion implantation. *J. Appl. Phys.*, 96 (3):1328–1335, 2004. 83